Potential ultra hard phases of ZrO_2-HfO_2 solid-solutions, derived from high P-T conditions

Neil Jackson

Faculty of Science

University of the Witwatersrand

A dissertation submitted to the Faculty of Science, University of the Witwatersrand, Johannesburg, in fulfilment of the requirements for the degree of

Master of Science.

2010

Declaration

I declare that this thesis is my own unaided work, except where due acknowledgement for the assistance received has been made. It is being submitted for the Degree of Master of Science at the University of the Witwatersrand, Johannesburg. It has not being submitted before for any degree or examination at any other university.

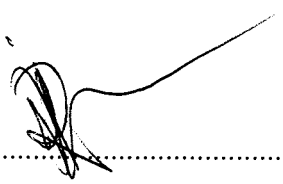

.....

(Signature of candidate)

.....02.....day of.....August.....2010

Abstract

The Merrill-Bassett gem anvil cell with a newly developed anvil polishing technique and the CO_2 laser heated diamond anvil cell was used to search for possible ultra hard phases of the unstabalized $Zr_xHf_{1-x}O_2$ (x=0.5) solid-solution. The pressure-temperature phase diagram of this compound was explored for the first time using angle dispersive x-ray diffraction. The pressure-temperature behaviour of this solid-solution was then compared to the diffraction data of the end members ZrO_2 and HfO_2. The investigative techniques of Raman spectroscopy and x-ray diffraction were used to clarify previous Raman spectroscopy studies. The structural changes from the sevenfold coordinated monoclinic to orthorhombic-I to the ninefold orthorhombic-II (cotunnite) structure under high pressure-temperature conditions were confirmed. Thus the potential for the $Zr_{0.5}Hf_{0.5}O_2$ solid-solution as a candidate for an ultra-hard ultra-tough "superceramic" was confirmed.

To my family for all their love and support.

Acknowledgements

I am especially grateful to my original supervisor, Professor Giovanni Hearne for his guidance and encouragement during the course of this work. It has been a pleasure to work with such an incredible scientist who is such an expert in the field of high pressure physics. His scientific ethic and love for his work was a constant source of encouragement and motivation during the numerous challenging experiments performed. I am thankful to Dr Naidoo, my supervisor since July 2009, for the support in administration, for his motivation in keeping my schedule on track and the final proof reading of my dissertation in the closing months of this dissertation. I acknowledge Professor Dave Billing my co-supervisor in the Department of Chemistry for assistance with regards to x-ray diffraction and allowing great ease of access to the Structural Chemistry resources.

This work could not have been completed without the invaluable advice and assistance from a number of people:

Professor F. Schoning for expert assistance in understanding the complexities involving high pressure x-ray diffraction and advice on the analysis of results. Mr R. Erasmus for the many hours of Raman measurement and assistance in investigating the many challenges involving high pressure Raman measurement. He has certainly played an integral role in the advancement of this dissertation. The technical staff from the workshop in the School of Physics for their assistance provided in machining and modifying high pressure apparatus. Dr A. Forbes at NLC CSIR, who provided much assistance in the CO_2 laser heating set up and provided much of the optics for the laser heating system through the rental pool system. Thanks goes to Mr C. Kasl for his suggestions and the valuable assistance with proof reading the final document.

The high pressure studies group and the structural chemistry students for general support and stimulating discussions during the experiments.

The support of the DST/NRF Centre of Excellence in Strong Materials (CoE-SM) towards this research is hereby acknowledged. Opinions expressed and conclusions arrived at, are those of the author and are not necessarily attributed to the CoE-SM. My gratitude goes to the wonderful people working at the CoE-SM for their assistance in administration and financial support provided to me during the course of this work.

Lastly a big thank you to my wonderful family and friends for their generous encouragement, understanding and patience which kept me motivated during the course of this degree.

Contents

List of Figures

List of Tables

Symbols and Acronyms

- HV - vickers hardness
- x - mols of Zr in $Zr_xHf_{1-x}O_2$
- P - pressure
- T - temperature
- CZ - cubic zirconia
- MB - Merrill-Bassett
- GAC - gem anvil cell
- DAC - diamond anvil cell
- (hkl) - Miller indicees
- OrthoI - orthorhombic-I
- OrthoII - orthorhombic-II (cotunnite)
- SG(#) - space group number
- PTM - pressure transmitting medium
- IR - infra-red
- λ - wavelength
- BA - Boelher-Almax
- TP - thrust plate
- BP - backing plate

1

Introduction

Zirconium dioxide (zirconia, ZrO_2) and hafnium dioxide (hafnia, HfO_2) are well known binary oxide materials that are used in applications such as structural ceramics, high temperature solid electrodes and also substrates for growth of other materials [1]. Materials of high hardness and toughness, with erosion and corrosion resistance, are increasingly important for modern industry. High hardness corresponds to high bulk modulus or low compressibility and some non-metallic materials with a high bulk modulus are shown in figure 1.1 [2]. Ultra hard materials are especially important in South Africa's billion dollar mining industry, where they can be used in grinding and cutting tools such as drill bits for oil exploration.

Zirconia (ZrO_2) based ceramics exhibit high temperature strength and high toughness. Possible applications of these ceramics include high-K (high permittivity) materials for use in Ge channel materials in metal-oxide-semiconductor field-effect transistor (MOSFETS) and to replace SiO_2 as the gate dielectric in complementary metal-oxide-semiconductor (CMOS) technology [3]. These ceramics are used extensively as implants in the dental industry in the form of dental caps and in optical films since zirconia based ceramics are transparent and have a high refractive index.

At ambient pressure and temperature both ZrO_2 and HfO_2 are stable in the so-called baddeleyite or monoclinic structure. At temperatures above $\sim$1000°C their structures change to tetragonal and then to the cubic fluorite structure as shown in figure 1.2 [1, 4]. At temperatures below 500°C the phase changes from monoclinic to orthorhombic-I (orthoI) at around 5 GPa, and to orthorhombic-II (orthoII or the so-called cotunnite structure) between 10 and 15 GPa in these materials. The high-pressure stabilized cotunnite phase can be recovered to ambient conditions (displays irreversibility) whereas orthoI cannot. The transformation to tetragonal

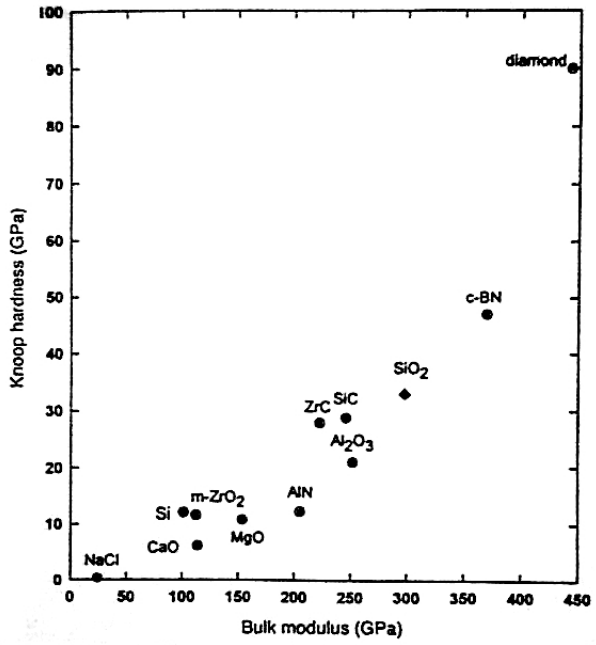

Figure 1.1: Hardness of materials - Hardness of some non-metallic materials as a function of bulk modulus [2].

from the orthoI phase is independent of pressure and occurs above 600°C for ZrO_2 [4] and above 1200°C in the case of HfO_2 [1]. Hafnia therefore has higher application temperatures than zirconia and is a better refractory material. The bulk modulus of cotunnite zirconia has been determined experimentally to be 278 GPa [5], compared with the calculated value of 305 GPa by Dewhurst [6]. The calculated and experimental bulk modulus of HfO_2 has been determined to be 306 GPa and 320 GPa respectively [7]. These high bulk moduli values demonstrate that both ZrO_2 and HfO_2 have properties of hard materials.

To achieve these ultra hard phases it is necessary to generate high pressures and high temperatures. To generate these extreme conditions anvil cells, multi anvil presses and shock compaction pressure techniques are used in conjunction with laser, resistive or furnace heating techniques. This project will investigate the ZrO_2-HfO_2 solid solution using the Merrill-Basset (MB) type diamond anvil cell (DAC) and gem anvil cell (GAC) in conjunction with CO_2 laser heating. Two diamond anvils with truncated tips are mounted in opposed orientation with a sample confined to a cavity drilled in a metal foil gasket sandwiched between the diamond tips. Pressurized, this assembly can be mounted in the CO_2 laser heating system. Thereafter the CO_2 laser can be focused directly on the sample and the entire sample raster scanned so that a

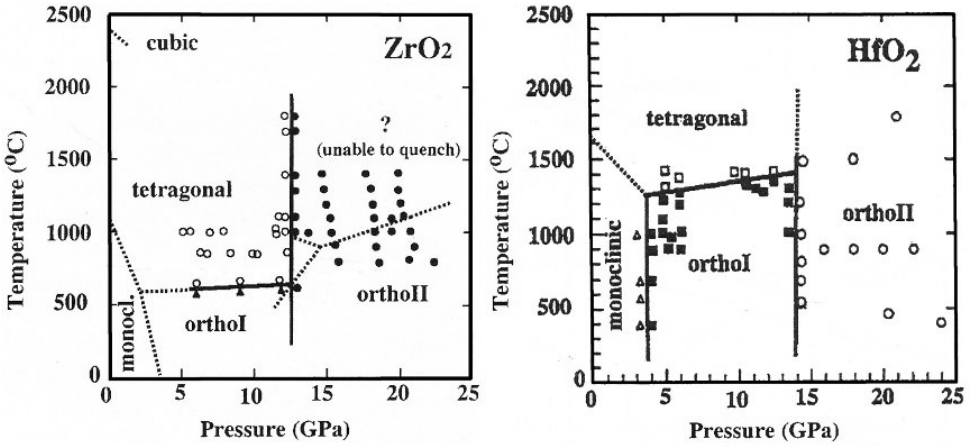

Figure 1.2: Phase diagram for ZrO_2 and HfO_2 - (a) ZrO_2 phase diagram, dotted and solid lines represent previously reported phase boundaries. Closed triangles, open circles, and closed circles represent the orthoI, tetragonal and orthoII phases respectively [4]. (b) HfO_2 phase diagram, dotted and solid lines represent previously reported phase boundaries. Open triangles, closed squares, open squares and open circles represent the monoclinic, orthoI, tetragonal and orthoII phases, respectively [1].

comparison between the XRD and Raman spectrum can be made.

Structure changes were monitored via Raman spectroscopy and then combined with experimental x-ray diffraction (XRD) patterns and then compared to results obtained from the literature of the end members.

1.1 Originality and novel features of the research

To date, there have been no published investigations of the pressure-temperature (P-T) phase diagram for the $Zr_{0.5}Hf_{0.5}O_2$ solid-solution system. A recent *in situ* high pressure Raman spectroscopy study on $Zr_{0.5}Hf_{0.5}O_2$ at room temperature to pressures of ∼30 GPa suggests that it adopts a phase transition sequence similar to the end-members ZrO_2 and HfO_2 (monoclinic/baddeleyite to orthoI to orthoII/cotunnite) [8]. Raman spectroscopy does not readily give structural details and there has been no prior (XRD) structural characterization of the high P-T (orthoI and orthoII) phases of $Zr_{0.5}Hf_{0.5}O_2$. The better characterization of high P-T phases of the solid solution $Zr_{0.5}Hf_{0.5}O_2$ using XRD and Raman spectroscopy will be the main goal of this study. New hand polishing cubic zirconia (CZ) anvil methods were developed for use in the gem anvil cell and tested in the region of ∼15 GPa. These newly developed CZ anvils were used to

study the phase change from monoclinic to orthoI and the metastability of the orthoI phase of the $Zr_{0.5}Hf_{0.5}O_2$ solid-solution at low pressures.

The facilities for processing to extreme conditions of high pressure/temperature (P-T) in the laser heated diamond anvil cell in the School of Physics at the University of the Witwatersrand (WITS) are perhaps unique in the Southern Hemisphere.

1.2 Aims and approaches of the project

The aim of this project was to investigate the potential ultra hard phases of the sol-gel processed ceramic $Zr_{0.5}Hf_{0.5}O_2$ solid-solution. High importance was placed on gaining extensive experience in high pressure and high temperature experimental techniques. The gem and diamond anvil cells were prepared for experiments using Raman spectroscopy and the limitations of the sample thickness, pressure transmitting medium and anvils investigated. Familiarity of laboratory based analysis techniques was a priority, therefore training on the modified Siemens SMART XRD system was extensive. Emphasis was placed on the development of the hand polishing of CZ anvils for use in the gem anvil cell to use at low pressures. $Zr_{0.5}Hf_{0.5}O_2$ (weak scatterer) and TiO_2 (strong scatterer) were investigated in the gem anvil cell using the triple confocal Raman conditions.

The project was divided up into four stages. The first stage was to become familiar with high pressure methodology. As the diamond anvils are expensive and easily breakable, a method was devised to hand polish cubic zirconia anvils. Moderate pressures ($\sim$10 GPa) can be achieved using these gem anvils and valuable experience gained with the $Zr_{0.5}Hf_{0.5}O_2$ solid-solution system and the high pressure apparatus. With experience gained in gem anvil cell methodology the diamond anvil cell was prepared and loaded. Learning and using Raman spectroscopy and XRD analysis techniques followed including training on a myriad of software packages. The last stage was to perform CO_2 laser heating on the sample. Liquid Ar was chosen to be the pressure transmitting medium to insulate the sample and was cryogenically loaded. The CO_2 laser heating system involves setting up and performing preliminary alignment and modifications specific to the experimental conditions.

1.3 Structure of the dissertation

The background to the research topic, the aims and the novel aspects of this project are discussed in this introduction. A literature review containing details surrounding the similarities of the zirconia and hafnia systems including the structural similarities of the system under extreme conditions of pressure and temperature is presented in chapter 2. The literature review will include detailed discussions on the Merrill-Bassett gem anvil cell (MB-GAC), the Merrill-Bassett diamond anvil cell (MB-DAC), Raman spectroscopy, XRD and CO_2 laser heating. Experimental details are described in chapter 3. In chapter 4, the results obtained from high pressure experiments and laser heating experiments are presented in detail. The general discussion and conclusions of the results are presented in chapter 5.

2

Literature Review and Description of Experimental Methodologies

This chapter presents background information regarding the techniques, methods and theory covered in this dissertation. It will cover information regarding the sample chosen. The experimental apparatus, including the high pressure cells and the CO_2 laser heating system, Raman spectroscopy and XRD will be discussed in detail.

The literature review is divided into five main sections. Section 2.1 will discuss the importance of ultra hard materials in the Southern African context. Comparisons on the unstabalized $Zr_{0.5}Hf_{0.5}O_2$ solid-solution will be limited to information available on the end members ZrO_2 and HfO_2, and Raman spectroscopy work completed by Mojaki [8] in her PhD thesis.

Section 2.2 describes high pressure gem and diamond anvil cell methodology. The merits of static pressure generation will be compared to shock compression pressure generation. This section will introduce the various Merrill Basset (MB) high pressure cells and the MB pressure cell used in the current investigation will be described in detail.

This section will also include details on the new hand polishing technique used to manufacture CZ anvils as developed in our high pressure laboratory at WITS. The details of the metal foil used to make gaskets will be reviewed along with details concerning the pressure transmitting media and pressure measurement.

Section 2.3 describes the heating techniques using a 30 W CO_2 laser and its implementation in attaining high temperatures in the MB-DAC. The components of the laser heating system will be discussed along with the improvements made. Focusing the laser into a $\sim$200 μm diameter sample cavity is challenging and the theory of this setup is discussed. The temperature

measurement is non-trivial and some basic theory will be covered.

Section 2.4 describes the theory of the Raman spectroscopy technique and the implementation of Raman spectroscopy with the gem and diamond anvil cells is discussed.

Section 2.5 will focus on XRD applications in high pressure research. High pressure and high temperature are key techniques to fully explore the P-T phase diagram. Using XRD, phase transformations can be qualified and with sufficiently high quality data, quantified.

Raman inelastic light scattering by long wavelength optical phonons is a convenient and sensitive probe used to characterize local structural changes and able to monitor structural transitions in compounds. Combining this technique with XRD data will help qualify the phase information contained in the Raman spectra for the first time.

2.1 Ultra hard materials - unstablized $Zr_{0.5}Hf_{0.5}O_2$ as a candidate

The hardness of materials is related to the plastic deformation after indentation [2]. Ultra hard materials are very important in many sectors in South Africa and the world. The search for compounds as hard as diamond is very competitive and a lucrative industry. Materials with high hardness have many applications in high performance engineering applications like wear resistive coatings and machining [2] (a selection of these materials is shown in figure 2.1).

To achieve these ultra hard materials, high pressure and temperature is used as a means of stabilizing the material into more closely packed structures and also increases the de-localization of the valence electrons [9]. The effect of temperature results in less ordered or higher entropy structures, ionization and the disruption of chemical bonds [9]. By investigating the phase changes of a material we can potentially form interesting metastable phases which can be quenched to ambient conditions. The following section will describe the current information regarding $Zr_{0.5}Hf_{0.5}O_2$ as a possible candidate for a "superceramic". To my knowledge $Zr_{0.5}Hf_{0.5}O_2$ has not been studied by XRD before and information in the literature pertains to the end members ZrO_2 and HfO_2 and initial Raman spectroscopy performed by Mojaki [8] who synthesized the samples via the sol-gel method.

2.1.1 Sol-gel processing of $Zr_{0.5}Hf_{0.5}O_2$

The sol-gel method, a low temperature method that produces better purity than conventional high temperature processes, was used to synthesize the $Zr_{0.5}Hf_{0.5}O_2$ ceramic [8]. The sol-gel method involves the precipitation of the metal oxide particles in a solution to form a colloidal

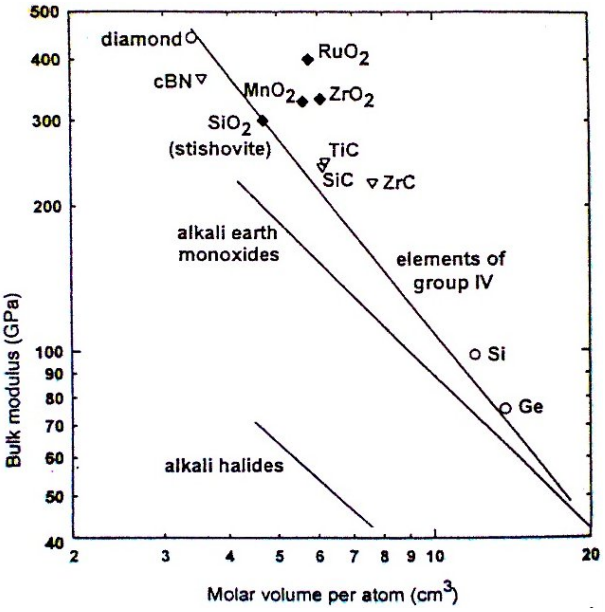

Figure 2.1: Bulk modulus of some hard materials - Modified figure of bulk modulus as a function of the mean volume per atom (log-log scale), with the solid diamond symbol representing high pressure phases of dioxides [1].

suspension called a sol [8]. Sol-gel processing can produce a variety of forms of a material, for example ultra-fine or spherical powders [8]. $Zr_{0.5}Hf_{0.5}O_2$ was chosen as the project candidate because of promising preliminary high P-T work performed by Mojaki [8].

2.1.2 Similarities between ZrO_2 and HfO_2

Zirconium and hafnium have similar atomic radii of 0.1442 nm and 0.1454 nm, respectively [8]. The compounds are so similar that HfO_2 was first discovered by x-ray spectroscopy in a ZrO_2 sample [10]. Both ZrO_2 and HfO_2 have high melting temperatures and form glassy materials when heated [10]. The ionic radii are 0.79 Å and 0.78 Å for Zr^{4+} and Hf^{4+} with electronegativity values 1.22 and 1.23, respectively. These figures demonstrate the similarities between Zr, Hf and their oxides. Due to the similarities of the crystal structure and phase transformation between ZrO_2 and HfO_2, continuous solid-solutions can be formed over the entire range of composition [8].

2.1.3 The high pressure and temperature phases of ZrO_2 and HfO_2

At ambient pressure and temperature, zirconia is stable in the so-called baddeleyite structure (monoclinic $P2_1/c$). It changes to the tetragonal structure ($P4_2/nmc$) at 1100°C, and then transforms to the cubic fluorite structure ($Fm3m$) at ∼2300°C [4]. Five structures of ZrO_2 have been identified at different pressures and temperatures. At ambient pressure zirconia is stable at room temperature in the monoclinic phase. It then transforms to tetragonal-I structure ($P4_2/nmc$) at ∼950°C and to the cubic fluorite phase at ∼2300°C with space group ($Fm3m$) [8]. Under high pressure of about 5 GPa at room temperature, ZrO_2 transforms to the tetragonal-I structure and then to an orthorhombic phase at about 15 GPa [8]. Ohtaka *et al.* [4] however, reported that the pressure induced transformation at 5 GPa goes to the orthoI phase and not the tetragonal-I phase and then to orthoII at ∼15 GPa. These transformations are reversible when the compound cools back to ambient conditions. When the tetragonal phase reverts back to the monoclinic phase, there is a volume increase of about 5% which causes cracking and structural failure, thus making it unsuitable to use pure zirconia as a starting material for synthesizing a new ultra hard material [8].

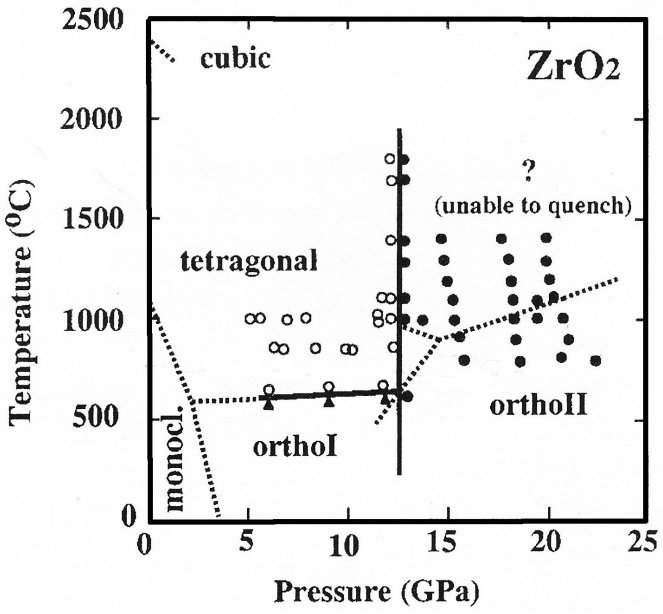

Figure 2.2: Phase diagram of ZrO_2 - The pressure-temperature phase diagram of ZrO_2. Reported phase boundaries are given by dashed lines. Phase boundaries by Ohtaka *et al.* [4] given by solid lines. Closed triangles, open circles, and closed circles represent the orthoI, tetragonal and orthoII phases, respectively [4].

The P-T phase diagram of ZrO_2 is depicted in figure 2.2. Zirconia changes from monoclinic to orthoI (*Pbca*) with a distorted fluorite structure, to orthoII (*Pnam*) structure with increasing pressure [4]. Zirconia changes to the tetragonal phase (above 600°C), after starting from the orthoI phase, as this transformation is independent of pressure, it then transforms to orthoII above 12.5 GPa accompanied by a 9% volume reduction [4].

Ohtaka *et al.* [4], found that the phase transformation of ZrO_2 from orthoI to tetragonal to be independent of pressure. For single crystals, the transformation of orthoI occurs between 4 GPa and 12 GPa [11] and transformation pressures are dependent on grain size. The high-pressure stabilized cotunnite phase can be recovered to ambient conditions whereas the orthoI phase cannot. The cotunnite phase is stable up to 1800°C and pressures well beyond 24 GPa [4]. Ohtaka *et al.* [5] determined the bulk modulus of cotunnite zirconia experimentally to be 278 GPa compared with the calculated value of 305 GPa [6]. Based on the bulk modulus hardness correlation plot of Yang *et al.* [12], cotunnite zirconia can be considered to be a hard material.

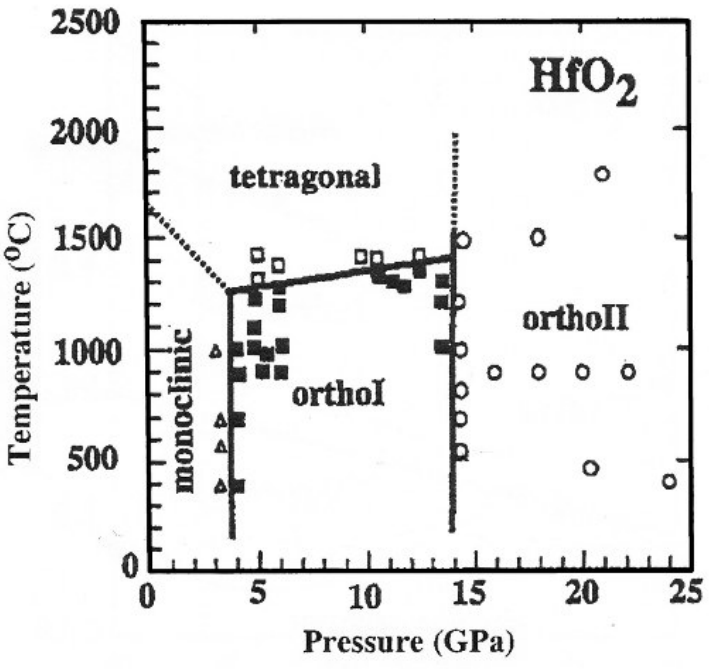

Figure 2.3: Phase diagram of HfO_2 - Pressure-temperature phase diagram of HfO_2 determined from *in situ* XRD measurements. Reported phase boundaries are given by dashed lines and the triangle, solid square, square and circle symbols represent the monoclinic, orthoI, tetragonal and orthoII phases, respectively [1].

Hafnia (HfO_2) changes to the same structures as zirconia under the increase of pressure at similar values (ZrO_2 in figure 2.2 and HfO_2 in figure 2.3). As the temperature increases, the phase changes from orthoI to tetragonal but at a higher temperature than in zirconia. It is isostructural to zirconia and more stable. Hafnia has applications at higher temperatures than zirconia and therefore is a better refractory material. Similarly to zirconia, as shown in figure 2.3, hafnia transforms from monoclinic to orthoI to orthoII (cotunnite), structures with increasing pressure. Liu [11] determined the transition pressures to be 4 GPa and 14.5 GPa and like zirconia the transformation pressures are also dependent on grain size. The cotunnite phase in hafnia can be retained to room temperature and atmospheric pressure as in zirconia, while the orthoI phase cannot. The calculated and experimental bulk modulus has been determined to be 306 GPa and 320 GPa, respectively [7], therefore giving properties of a hard material (high bulk modulus).

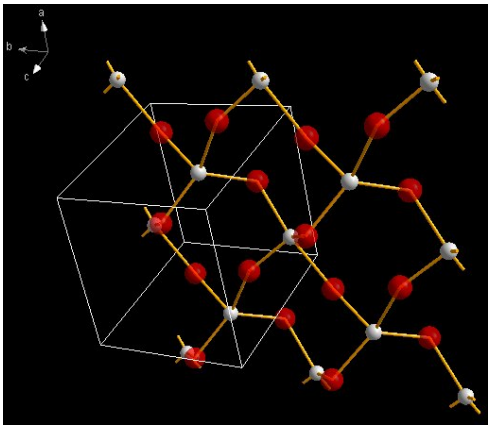

Figure 2.4: Monoclinic ZrO_2 or HfO_2 - Monoclinic ambient phase of ZrO_2 or HfO_2, space group P121/c1 SG(14) ICSD-89426 [13]. Zr or Hf represented by small white spheres and O are the red spheres. The monoclinic phase of ZrO_2 or HfO_2 are sevenfold coordinated dioxides.

Figures 2.4, 2.5 and 2.6 show the monoclinic, orthoI and the orthoII structures of the end members ZrO_2 and HfO_2, respectively.

2.2 High pressure methodology

High pressure can be generated using two techniques, via shock wave and static compression. Shock wave experiments in increasing pulse duration consists of laser irradiation, electric discharge and high explosive shock experiments shown in figure 2.7 [14]. These techniques are

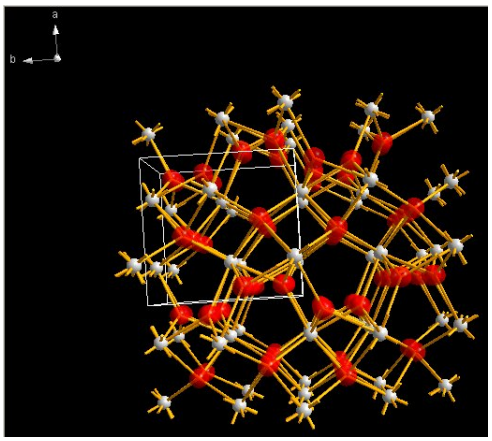

Figure 2.5: High pressure orthoI phase of ZrO_2 or HfO_2 - High pressure orthoI phase of ZrO_2 and HfO_2, space group Pbcm SG(57) ICSD-77716 [13]. Zr or Hf represented by small white spheres and O are the red spheres.

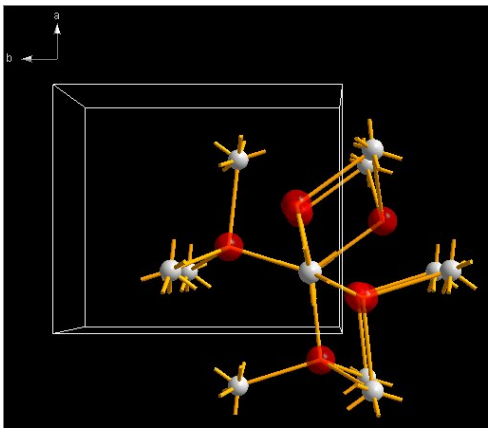

Figure 2.6: High pressure orthoII phase of ZrO_2 or HfO_2 - High pressure orthoII (cotunnite) phase of ZrO_2 or HfO_2, space group Pnma SG(62) ICSD-83862 [13]. Zr or Hf represented by small white spheres and O are the red spheres. The orthoII phase of ZrO_2 or HfO_2 are ninefold coordinated dioxides.

mainly used to simulate natural pressure and temperature occurrences such as meteorite impacts [14].

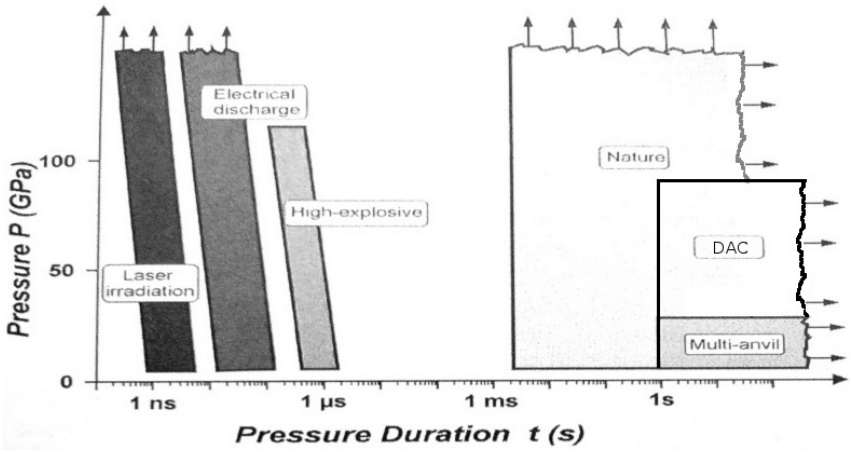

Figure 2.7: Shock wave vs. DAC experiments - Comparison of shock wave pressure generation vs. DAC pressure generation [14].

Shock wave experiments consist of a high velocity projectile that hits a target thus inducing a shock wave within the target. The Huguenot relations are used to analyse the target by treating the shock wave as an ideal discontinuity. The conservation of mass, momentum and energy must be applied across the shock wave giving the following relations [8]:

$$P - P_0 = \rho_0 \mu_s \mu_P, \tag{2.1}$$

$$\rho = \frac{\rho_0 \mu_s}{(\mu_s - \mu_P)}, \tag{2.2}$$

$$E - E_0 = \frac{1}{2}(V_0 - V)(P + P_0), \tag{2.3}$$

where μ_s is the velocity of the shock wave and μ_P the velocity of the projectile. E_0, P_0, V_0 and ρ_0 are the initial energy, pressure, volume and density, respectively.

The DAC is used to generate static pressures as shown in figure 2.8, with

$$P = \frac{F}{A}, \tag{2.4}$$

where P is the pressure and F the force applied to area A, which is the truncated polished tip of the anvil called the culet. This relation shows a large force applied to a small area generates

large pressures. The DAC takes advantage of both of these requirements by having small anvil faces and the thrust screws generating large forces. The gasket acts as a container ring and the pressure transmitting medium (PTM) ensures that the pressure is transmitted hydrostatically (from all sides) to the sample.

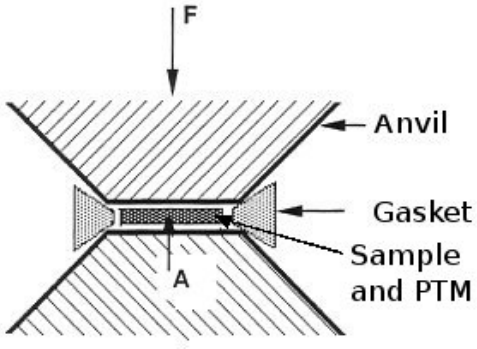

Figure 2.8: DAC pressure generation - Schematic of the principle of pressure generation in a DAC with F representing the applied force to the area A [15].

The details involving the anvil cells will be further described in the sections 2.2.1 and 2.2.2.

2.2.1 The gem anvil cell (GAC)

Various gems have been utilized to generate pressure in anvil cells including CZ, sapphire and diamond [16]. Diamond anvils have been used to generate the highest static pressures due to their high hardness (442 GPa shown in figure 2.12), defined as having high bulk modulus (measured in GPa) and high shear modulus (values over 100 GPa) [2]. Diamonds also exhibit the best thermal conduction at room temperature and excellent electrical insulation [2].

Diamond anvils are however expensive, difficult to manufacture and the DAC methodology is considered to be somewhat specialized, thus limiting widespread application in many laboratories. In addition, diamonds are not optically transparent over the entire electromagnetic spectrum, having experimental limitations such as an intense broad infra-red (IR) absorption from 2600 cm^{-1} to 1800 cm^{-1} (for type II diamonds) and are also unstable when heated in air at around 700°C, as they graphitize [17]. Diamond anvils have a high intensity background fluorescence which can mask or interfere with the scattering from the sample [17]. In type I diamonds there are absorption bands at 2000 cm^{-1} and 1250 cm^{-1} and for type II diamonds the absorption bands are at 2500 cm^{-1} and 1850 cm^{-1} which can mask the area of scattering interest (refer to figure 2.9) [18].

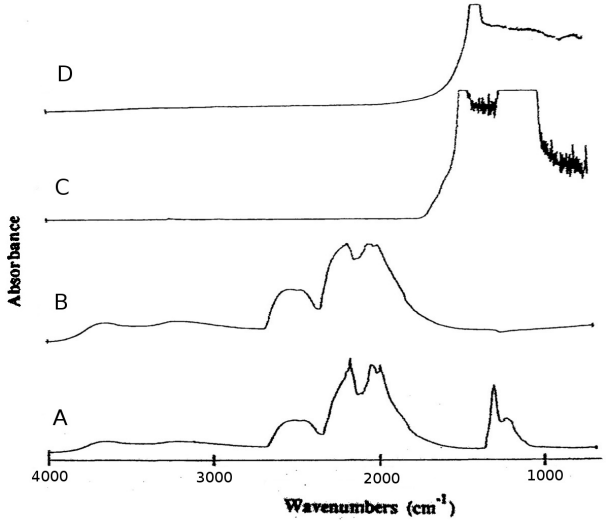

Figure 2.9: FT-IR absorbance - FT-IR (fourier transform - infra red) absorbance of (A) type I diamond, (B) type II diamond, (C) sapphire and (D) cubic zirconia [17].

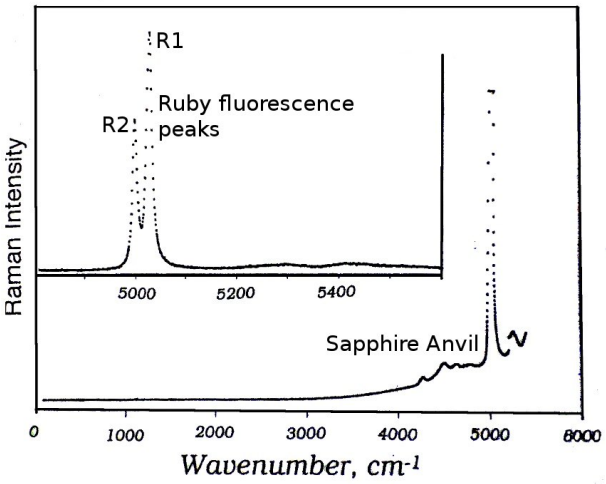

Figure 2.10: Raman spectrum for sapphire anvils - Raman intensities for sapphire anvils in comparison with the $R1$ and $R2$ ruby fluorescence peaks, showing that the sapphire Raman bands, excited by 514.5 nm Ar ion laser beam, interfere with the ruby lines at around 5000 cm^{-1} [19].

Gem substitutes for diamond anvils have been investigated, each having associated advantages and disadvantages over diamond. The advantages of using gems is that they are cheaper and are electromagnetically transparent in different regions (shown in figures 2.9 to 2.11) to that of diamond anvils. Sapphire and quartz would be good choices due to comparable hardness with diamond, cost effectiveness and machining ease. These substitutes are more stable at high temperature but have the same disadvantage as diamond in that they absorb light in the mid-IR wavelengths as shown in figure 2.10 [17]. Sapphire cannot be used below 1850 cm^{-1} (figures 2.9 (C) and 2.10) and quartz cannot be used above 2900 cm^{-1} [17]. Sapphire is inferior to CZ due to the IR absorption of two unknown peaks at 692.8 nm and 694.2 nm [19]. Metastable brilliant cut single crystal cubic zirconia (ZrO_2 stabilized with approximately 10-mol% Y_2O_3) has found widespread acceptance since 1976 as a diamond substitute in the jewellery industry [17]. CZ is extremely inert and has a high hardness (Knoop hardness = 1370). CZ can be used up to 2400°C in air and is transparent in a large part of the electromagnetic spectrum as shown in figures 2.9 D and 2.11 [17].

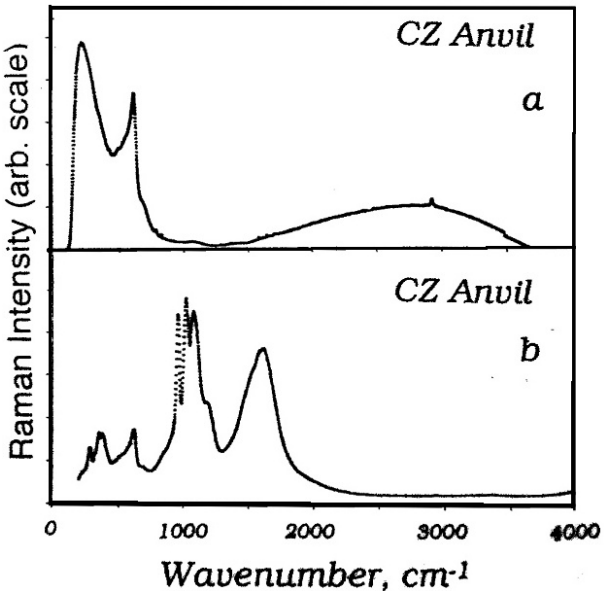

Figure 2.11: CZ anvil Raman bands - Raman bands for CZ anvils showing (a) excitation by a 432 nm He-Ne laser beam; (b) by a 514.5 nm Ar ion laser beam [19].

The GAC has been used to obtain moderate pressures of ∼15 GPa [20] depending on the culet size, pressure transmitting medium and the gasket material used, which will be expanded upon in sections 2.2.4 and 2.2.5. Russell and Piermarini [18] highlighted that generating pressures

above 10 GPa using gem anvils is non-trivial in efforts spanning the last 20 years or so using various experimental set-ups. Experimentation of various culet sizes by pairing a 254 μm culet with a 762 μm culet to replace the larger failed anvil thus minimising down time has been explored [17]. Russell and Piermarini [18] have used 500 μm to 1 mm culets with thin gaskets of 125 μm T301 stainless steel. Patterson and Margrave [17] achieved pressures up to 2 GPa using culet sizes of 500 μm and 1 mm. Xu and Huang [21] achieved pressures of 8.9 GPa [18]. Russell and Piermarini have achieved pressures of 13.2 GPa with a noteworthy significant broadening of the ruby fluorescence lines above 10 GPa [18]. They highlighted the absence of the CZ anvil fluorescence or CZ Raman scattering when between 800 cm^{-1} and 1600 cm^{-1} wave numbers, for a 432 nm He-Ne laser. In figure 2.12 a comparison of diamond, sapphire and CZ anvils is made and presents favourable data supporting CZ anvils as good substitutes for diamond anvils.

	Diamond	Sapphire	C-Zirconia
Chemical composition	C	Al_2O_3	ZrO_2
Major impurities (mol %)	0.2 N_2	...	15Y_2O_3
Crystal structure	$Fd3m$-O^7_k	R-3C(D^6_{3d})	Cubic
Density (g/cm^3)	3.51524	3.97	5.6
Hardness (Knoop scale)	5700-10 400	1370, 1525-2000	1370
Bulk modulus (GPa)	442	253-255	205
Young's modulus	1050	348.6	252
Melting point (°C)	>3550	2105	2680
Thermal conductivity (Wm-1 K-1 at 293 K)	Ia, 600-1000 II, 2000-2100	35	1.8
Thermal expansion (10-6)	0.8	7.8	10
Stable temperature in air (°C)	700	1700	2400
Refractive index n	2.4237 (546 nm)	1.73 (2.2 μm)	2.15-2.18
Optical transparency	IIa, 225 nm-2.5 μm and > 10 μm I, 340 nm - 2.5 μm, and > 10 μm	<5.5 μm	<6.9 μm
Resistivity (Ω m)	I & IIa, >10^{18} IIb, 10^3-10^5	...	10^7

Figure 2.12: Properties of diamond, sapphire and cubic zirconia - The properties of some anvils that have been used to generate pressure in the miniature anvil cells, reproduced from reference [21].

2.2.1.1 CZ hand polished anvils

Simplified manual polishing procedures have been developed for fabricating CZ anvils for GAC high-pressure experiments. To the best of my knowledge there have been no reports indicating the polishing of CZ anvils manually.

The manual polishing method was developed using guidelines similar to machine polishing. The hand held gem holder is a modification of the holder used in an industrial polishing machine as shown in the next chapter, section 3.2.1. The hand polishing technique produces very rounded anvil faces (and a rounded bevelled edge) seen by the circular Newtons rings on the CZ culet as opposed to the straight Newtons fringes seen on diamond anvils. This can be clearly seen in figure 2.13 and figure 3.6 in section 3.2. The degree of rounding is given by the radius of the N^{th} Newton ring:

$$r_N = [(N - \frac{1}{2})\lambda R)]^{\frac{1}{2}} \tag{2.5}$$

R is the radius of the lens through which the light passes, N is the bright ring number, and λ the wavelength of light. In this case R would give an indication of distortion of the culet surface that acts as the lens, *i.e.* if N is small and r_N large it will imply that the lens (in this case the culet) is relatively flat.

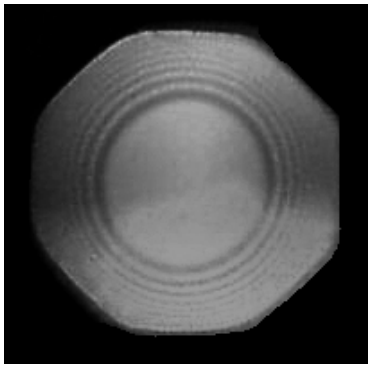

Figure 2.13: Interface between the CZ anvil and glass showing Newtons interference fringes - Circular Newtons fringes showing the degree of rounding of the CZ anvils viewed through one of the two opposing CZ anvils. The rings originate from the centre of the culet and are symmetrical indicating that the anvils are parallel. The shadow or outline of both anvils overlap and indicate that the anvils are concentric to one another.

2.2.2 The Merrill-Bassett diamond anvil cell (MB-DAC)

Diamond anvil cells can be used for a variety of experimental measurements such as Raman spectrometry, IR spectrometry, magnetism and XRD measurements [17, 22]. The range of compounds that have been studied in the last 30 years is extensive in fields such as chemistry, biology and physics and have included experiments on condensed gases, amino acids, proteins,

pharmaceutical compounds and various materials [22]. Jayaraman classified the design of DACs into five categories. Four are piston cylinder type cells, namely, the National Bureau of Standards cell, the Bassett cell, the Mao-Bell cell and the Syassen-Holzapfel cell [23]. The fifth cell, using a simple concept of thrust plates and driving screws, is called the Merrill-Bassett cell [23]. Originally these 45 mm diameter cells would be used in single crystal experiments and would only reach pressures of about 5 GPa [23]. The MB type diamond anvil cell has been through various iterations and geometry changes but the basic mode of operation remains the same [24].

Sterer *et al.* [23] noted that in conventional MB type anvil cells, the three screw design is only stable up to about 25 GPa and that the stability of the cell is highly dependant on the elastic limit of the screws. The modified design used in this study incorporates 6 allen thrust screws as shown in figure 2.14 [23]. The MB-DAC is of the transmission geometry type and is one of the most widely used types of cells [22]. Originally the design of the MB cell was based on the constraints that it should fit on a standard goniometer head and be small enough to fit the space requirements of a standard precession camera and a single-crystal orienter [22]. This small and simple design consists of two platens that are pulled together by allen screws. The platens are located on posts for stability and are kept parallel by careful measurement. Vertical posts are included for two reasons, namely, to position the metal gasket for precise and consistent alignment when indenting, and secondly to position the top thrust plate and insure precise vertical movement. Three additional holes are located in both thrust plates so that the cell can be positioned on a specially designed torque lever for the pressure allen screws to be torqued. The MB-DACs are manufactured in the School of Physics (WITS) using INC718 (steel alloy) and have a Vickers hardness of 440 HV after annealing in a furnace at 718°C for 8 hours under hydrogen or argon.

Anvils are mounted on the polished backing plates, which are inserted into the thrust plates. The anvils are aligned with their culets parallel and concentric. The cell is closed after a 100 μm thick glass slide is inserted between the anvils. This is done to protect the anvil faces from coming into contact with each other which would cause chipping or scratching thus lowering the integrity of the culets. The interference fringes between the diamond anvils disappear when aligned, whereas the hand polished anvils give the circular Newtons rings originating in the centre of the anvil face. A metal gasket of SS301 (diamond anvils) and $Ta_{90}W_{10}$ (CZ anvils) is pre-indented up to a thickness of about 30 μm and is sandwiched between the anvils [18]. The gasket is drilled and the cavity is then loaded with a pressure transmitting medium along with the sample and a pressure sensitive marker [18]. Measurements are then taken through the

diamonds as the platens and backing plates have exit cones of between 80° and 30° depending on the experimental requirements. This is a versatile design that allows single crystal diffraction experiments incorporating various materials and substances using laboratory based equipment and synchrotron sources [22].

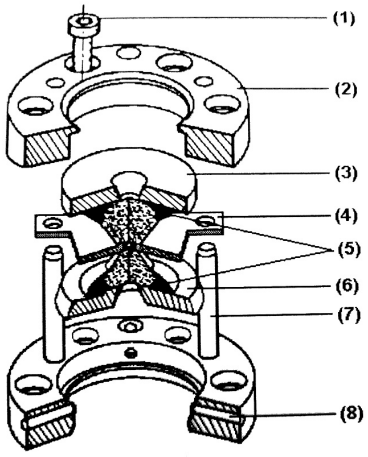

Figure 2.14: Exploded view of the MB cell - Cut-away exploded view of a modified MB cell. (1) Thrust screw, (2) thrust plate, (3) backing plate, (4) gasket (5), diamonds and epoxy, (6) bottom backing plate, (7) supporting posts and (8) lateral adjusting screw.

2.2.3 Determining pressure within the pressure cell

There are several methods of measuring the pressure in a DAC. One method is to include a material with a known pressure-volume equation of state (EoS) and the other is to load a pressure calibrant such as ruby chips/ balls (Cr^{3+} doped α-Al_2O_3) or MgO:V^{2+} into the gasket cavity along with the sample into the high pressure cell [17]. The lattice parameter of the marker can then be determined by XRD by tracking significant peaks and calculating the lattice parameter from the EoS. The ruby fluorescence $R1$ and $R2$ peaks can be measured and the pressure can be determined from the excitation wavelength using equations 2.6 and 2.7.Originally Russel [18] applied this idea of including a marker and by using the Decker EoS of NaCl up to 19.5 GPa to calibrate the ruby scale. The assumption is that both the marker and ruby are at the same pressure and then the line shift of the ruby fluorescence $R1$ taken along with diffraction data can be used to calibrate the ruby scale [25].

The ruby pressure scale is an easy way to determine pressure within the DAC and has been informally adopted within the high pressure community as a standard. Ruby has spectral lines

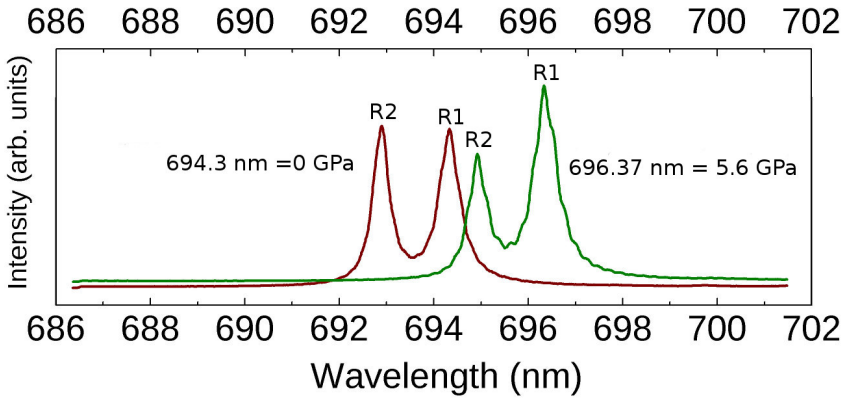

Figure 2.15: Ruby fluorescence $R1$ and $R2$ - $R1$ and $R2$ lines excited with an Ar ion laser (514.4 nm) showing pressures of 0 GPa ($R1$ at 694.31 nm) and 5.5 GPa ($R1$ at 696.37 nm).

R, U, B and Y in the visible spectrum with the higher U, B and Y being able to be pumped with a laser which relaxes to the R lines $R1$ and $R2$ as shown in figure 2.16 [25]. The $R1$ and $R2$ lines are metastable with long lifetimes that fluoresce down to the ground state [25]. Zero pressure represents $\lambda_0 = 694.24$ nm and $\lambda_0 = 692.81$ nm for $R1$ and $R2$ at 298 K, respectively [25]. The peak of the usually stronger $R1$ line is used for the calibration and pressure measurement. A zero pressure calibration is always performed for each experiment as the λ_0 value does not always match the quoted values as shown in figure 2.16. The luminescence and absorption spectrum is shown in figure 2.16. Piermarini *et al.* calibrated the $R1$ line shift against the NaCl EoS in 1975 [25] and since then a few more calibrations have been necessary to extend the calibration to higher pressures.

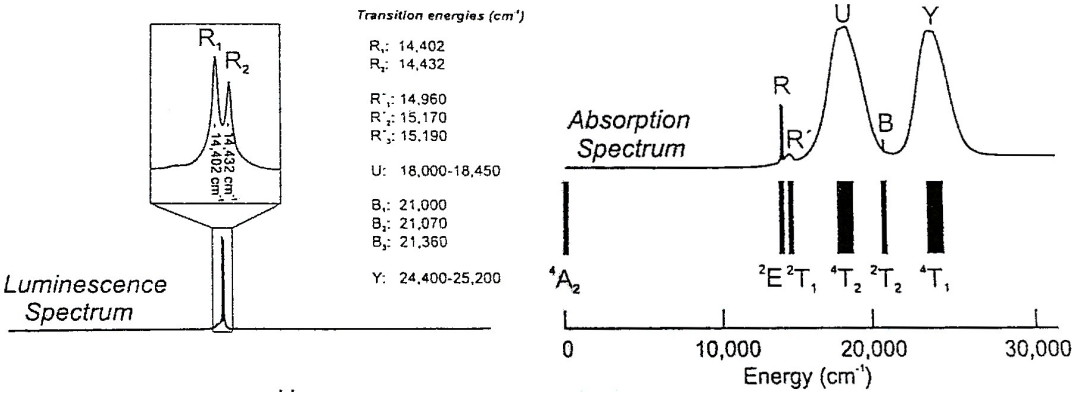

Figure 2.16: Electron-energy level term scheme - Luminescence and absorption spectra for ruby [24].

Piermarini *et al*. calibrated the wavelength shift against the Decker EoS of NaCl and found a linear dependency of

$$\frac{\Delta\lambda}{\Delta P} = 0.365 \tag{2.6}$$

Mao *et al*. [25] and Bell [25], using quasi-hydrostatic and non-hydrostatic pressure to megabar pressures to re-calibrate the ruby scale, found the empirical quasi-linear relationship

$$P = A[(\frac{\lambda}{\lambda_0})^B - 1]/B, \tag{2.7}$$

using $A = 1904$ and $B = 7.665$ (the slope and curvature parameters, respectively) for quasi-hydrostatic and $B = 5$ for non-hydrostatic conditions. Silvera *et al*. [25] have since calibrated the $R1$ line to 150 GPa using equation 2.7 with $A = 1876$ and $B = 10.71$.

Even though the fluorescence method is ideal to do fast and easy pressure calibration between 0.01-0.1 GPa, the precision is limited to about 0.02-0.05 GPa due to differential thermal expansion of the components of the DAC and to time dependent mechanical relaxation within the gasket [24]. Pressure can be determined by means of an internal pressure marker such as NaCl or Pt Black and calculating the pressure from the unit-cell parameters using the materials' EoS. The Birch-Murnaghan equation of state is:

$$P(V) = 1.5B_0[(\frac{V}{V_0})^{-7/3} - (\frac{V}{V_0})^{-5/3}] \times \{1 + 0.75(B_0' - 4)[(\frac{V}{V_0})^{-2/3} - 1]\} \tag{2.8}$$

where B_0, V_0 and B_0' are the bulk modulus, the atomic volume and the pressure derivative of the bulk modulus, respectively.

Having a hydrostatic environment is ideal for the cavity contents and reliable pressure measurements need to be taken. The choice of pressure transmitting medium is determined via experimental parameters.

2.2.4 Pressure transmitting medium (PTM)

The identification of a suitable PTM is experiment specific. This is considerably more difficult when using CZ anvils. There is a parabolic stress distribution across the anvil face under pressure, with the maximum stress at the centre of the anvil [18]. When a liquid hydrostatic PTM like ethanol:methanol (4:1) or glycerine is employed the pressure gradient is undetectable so the pressure distribution is a truncated shape across the gasket hole diameter [18]. When a PTM like NaCl and AgCl solids are employed, there is additional support across the sample and thereby

decreasing the truncation of the parabolic stress across the gasket hole diameter [18]. The decision on what PTM to use was based on my own experimental data using Raman spectroscopy. This is due to the anvils, PTM and the sample giving off Raman bands necessitating the PTM chosen to optimise the Raman signal and to minimise the interference from any Raman bands originating from the PTM. For the initial high pressure experiments, the PTM considered was Si oil (vacuum pump oil), Fluorinert FC70/FC77 (1:1) or NaCl flakes. The NaCl flakes look similar to the sample flakes and therefore makes discerning the sample flakes difficult. For the high pressure laser heating experiments, liquid Ar was used because it insulates the diamond anvils from the sample [26, 27].

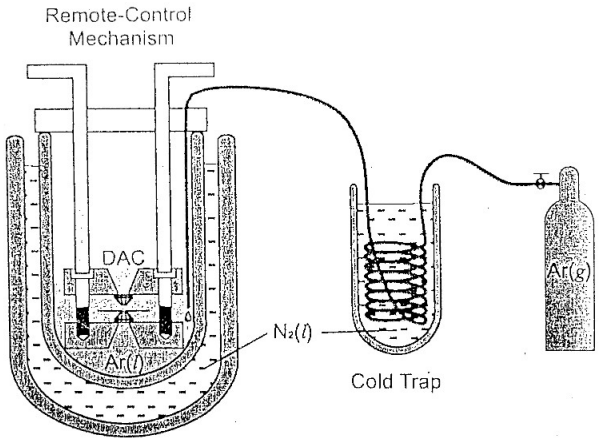

Figure 2.17: Cryogenic loading apparatus - Apparatus for making liquid Ar PTM using a bath of liquid N. The Ar gas flows from the gas bottle through the coil submerged in liquid N. The Ar gas is liquefied and collected in a vessel for the MB-DAC to be submerged in.

As seen in figure 2.17, the high pressure cell can be loaded with liquid Ar (boiling point of 87 K). Commercial welding argon (purity better than 99.996%) is liquefied by flowing the Ar gas through a heat exchanger coil submerged in liquid nitrogen (boiling point of 77 K). The cell is then lowered into the liquid Ar and the screws cracked open to reference positions and the PTM allowed to flow in. The screws are then tightened. This low temperature process is tricky as it affects the movement of the screws and the platens and it is not possible to view the process easily due to the slight convection of the liquid [26].

If the cell is pressurized above 1.2 GPa, the Ar has already crystallized in the hexagonal close packed (h.c.p.) structure before being heated up [26]. If the cell is below 1.2 GPa further pressurization is required to crystallize the argon and it goes to the face centred cubic (f.c.c.) structure once the cell is at room temperature.

2.2.5 Gasket materials

The choice of gasket material as in the case of PTM is also highly dependent on the experimental setup. It depends on the type of anvils being used and also the analysis technique employed. Typically a metal gasket of 200 μm starting thickness is used. Various gasketing materials that are suitable such as tungsten, rhenium, hardened stainless steel, martensitic tool-steel or alloys for example inconell or Cu-Be may be used [24]. CZ anvils require a softer gasketing material due to the possibility of breaking these anvils when pre-indenting. CuBe and $Ta_{90}W_{10}$ were explored because they are not considered very hard but are able to fully support the sample cavity. Xu and Huang [21] used T301 stainless steel gaskets of 0.125 mm thickness in CZ anvil cells successfully to only 7.8 GPa. Pb was also considered a possible gasketing material but reports show that it will only support the cavity to pressures of around 2 GPa [17]. Tungsten gasket has been tested to 50 GPa with the cavity diameter shrinking from 130 μm to 75 μm [28]. In extremely high pressure experiments rhenium gaskets are used in high pressure cells of up to 222 GPa [29].

2.3 Heating the sample in a MB-DAC

Three methods of heating the DAC are possible. A purpose built mini furnace for heating of the entire DAC under H_2 or Ar gas and a CO_2 laser heating facility were considered. The third method of heating a sample is to place resistive wires in the cavity but this method was not explored. Furnace heating results in the entire cell being heated and the behaviour of the cell due to the expansion of the metal body adds uncertainty to the pressure measurement, as the pressure measurement is not done *in situ*. The cell body is made from INC718 alloy (heat treated at 718°C) therefore furnace heating is limited to below this value. The anvils are typically glued to the backing plates with epoxy. Furnace heating is advantageous due to ease of measuring and controlling the temperature via the furnace thermocouple and the trivial placement of the cell within the furnace as compared with the challenging setup of the CO_2 laser heating facility and DAC alignment.

2.3.1 CO_2 laser heating

The wavelength of the CO_2 laser is convenient to use due to the fact that we are able to focus the beam down to about 30-50 μm on the sample and reach temperatures of up to about 3300°C [27]. This is advantageous when using a cavity size of 100 μm in diameter which is an average cavity

size used in DAC experiments. This allows for heating of very specific areas of sample while leaving other areas unheated that can be used as a reference in the cell. Most importantly, ZrO_2 and HfO_2 absorb 10.6 μm wavelength from the CO_2 laser as metal oxides are strongly absorbing at the 10.6 μm wavelength [27]. The CO_2 laser is therefore suitable for heating the $Zr_{0.5}Hf_{0.5}O_2$ solid-solution. The attenuation is believed to be about 70% using the type Ia anvils (used in this study) compared with the highly transparent type IIa diamond anvil windows which are rare and expensive [27].

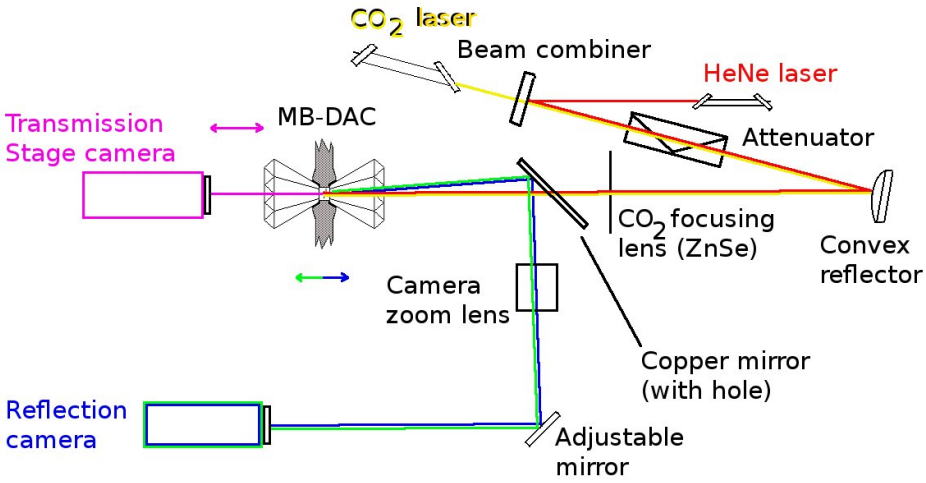

Figure 2.18: Laser heating setup - The modified CO_2 laser heating setup in the School of Physics.

The CO_2 laser heating setup is shown in figure 2.18. The setup was modified from the setup mentioned in the paper by Hearne *et al.* [27]. The system consists of a co-linear laser of the 30 W continuous wave CO_2 laser and HeNe laser (yellow and red paths combined) due to the CO_2 being invisible. The lasers are aligned by doing a near field and far field test by using heat sensitive paper. Laser light passes through the attenuator (calibrated between 0 and 100%). The convex lens expands the CO_2 laser on to the CO_2 focusing lens (ZnSe) mounted on a three axis stage and the light is then focused onto the sample through the copper mirror. The copper mirror has a hole drilled through it to allow the laser light through onto the sample and was newly installed. The light is then collected on the mirror (blue and green paths) and reflected through the camera zoom lens on to the bullet camera (blue and green paths) to be viewed on the monitor. A 50:50 beam splitter can be inserted before the camera to reflect light onto an

optical fibre for temperature measurements (not shown). The reflected light from the sample is not parallel to the incoming CO_2 laser light and as the stage is moved horizontally the reflected light takes a different path. This system therefore displays the image moving horizontally across the monitor and can only be used for vertical alignment. This alignment problem was not discovered in the paper by Hearne *et al.* [27]. A second colour CCD camera (pink) was installed on the sample stage for easier alignment of the CO_2 laser.

From the phase diagrams of the end members in figures 2.2 and 2.3, we can see the temperatures used to synthesize orthoI and orthoII were between 500°C and 1000°C. Using these phase diagrams as guidelines we hoped to achieve similar processing temperatures. On the current laser heating system two methods of temperature measurement are possible. The first involves a system of changing the angle of the polariser and comparing the resulting signal to a reference value [27]. The second, uses a spectro-radiometric method that measures grey body emission and the temperature extracted from the Planck black-body radiation formula. The Wien approximation to the Planck formula is often used as the temperature is more easily extracted from the linear fit:

$$J(\lambda) = ln(\epsilon(\lambda)) - \omega(\lambda)T^{-1}, \tag{2.9}$$

where $J(\lambda) = ln(I_\lambda \lambda^5/c_1)$, I_λ is the spectral intensity, $\omega(\lambda) = c_2/\lambda$, ϵ the emissivity and T the temperature. The constants are $c_1 = 2\pi hc^2 = 3.7418 \times 10^{-16}$ Wm^2 and $c_2 = hc/k_B$, $hc/k_B = 1.4388\times 10^{-2}$ mK. Focus from the various optical elements can be determined easily using a substitute sample in place of the DAC by emission. However, the diamonds in the DAC act as lenses themselves and have different refractive indices requiring the focus to be calculated using the following formula:

$$\frac{AD}{RD} = \frac{n_1}{n_2} \tag{2.10}$$

where RD is real depth, AD the apparent depth, n_1 and n_2 the indices of refraction of diamond and air, respectively. This formula was used to roughly calculate how far into the second diamond the laser focuses.

2.4 Raman spectroscopy

Raman scattering in the DAC provides a convenient way of investigating the effect of pressure on optical phonons in crystalline solids experimentally to several hundred kilobars [15]. In this

section Raman Spectroscopy will be briefly introduced and information is summarized from texts by Dr Sossé Ndiaye [30], Dhamelincourt *et al.* [31], Jayaraman [15] and Paula [32]. Textbooks by Long [33] and Gregora [34] were also consulted and a more comprehensive review can be found therein.

Raman spectroscopy is a type of vibrational spectroscopy. It is based on the inelastic scattering of light. Incident radiation is created with the use of a suitable laser source. Laser light produces a monochromatic, polarised narrow beam which has a well defined wave vector k_l. Light scattered in the direction k_s is collected over a certain solid angle $\Delta\Omega$ with wave number v. The bulk of the intensity would be due to Rayleigh scattering, where light of the same wavelength is elastically scattered by the sample. Weak lines to higher and lower energies would correspond to Raman scattering.

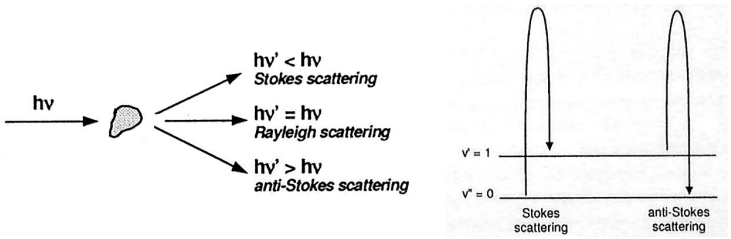

Figure 2.19: Principle of Stokes and anti-Stokes - Visualization of the Stokes and anti-Stokes scattering processes [32].

When a monochromatic light (*eg.* a laser), is shone on a material most of the light is transmitted or reflected elastically, however some inelastic scattering of the radiation is observed. Stokes Raman lines ($\tilde{v}_0 - \tilde{v}_i$) and the corresponding anti-Stokes Raman lines (shown in figure 2.19 ($\tilde{v}_0 + \tilde{v}_i$) appear symmetrically on both sides of the Rayleigh line ($\tilde{v}_0$) with ($\tilde{v}_0$) and ($\tilde{v}_i$) the absolute wave numbers ($\tilde{v} = v/c$). Raman bands can be regarded as unique fingerprints that also give information about the local molecular environment. Suppose that a photon of a given energy (and wavelength) collides with a sample. When energy is transferred from a molecule to the photon, light of higher energy (shorter wavelength) will be scattered by the sample (anti-Stokes scattering). When energy is transferred from the photon to the molecule, light of lower energy (longer wavelength) will be scattered by the sample (Stokes scattering). Both the Stokes and anti-Stokes scattering are associated with transitions between rotational, vibrational and electronic levels [33]. The new wave numbers are called Raman lines or bands and constitute the Raman spectrum [33].

For Stokes scattering,

$$\tilde{v}_{out} - \tilde{v}_{in} = -\Delta\tilde{v} = G(v+1) - G(v) + \frac{1}{2\pi c}\sqrt{\frac{k_Q}{\mu_Q}} \tag{2.11}$$

and anti-Stokes scattering,

$$\tilde{v}_{out} + \tilde{v}_{in} = \Delta\tilde{v} \tag{2.12}$$

where k_Q and μ_Q are the force constant and reduced mass of the normal mode, respectively; $G(v+1)$ and $G(v)$ are vibrational terms for the $v+1$ and v states; and $\Delta\tilde{v}$ is the so-called Raman shift, expressed in units of cm^{-1} (shown in 2.19). Molecules are in motion inside the lattice and consist of rotational, translational and vibrational modes.

2.4.1 Vibrational energies and polarization effects

From quantum mechanics, only well defined modes are allowed. These are the normal modes or phonons which are responsible for physical qualities in materials including thermal and electrical conduction (for example, the heat conduction in insulators or the propagation of sound in solids). Raman spectroscopy has consistently been shown to be a useful tool in the characterisation of the structure of metal oxides in both the bulk and the surface supported phases [8]. Visible Raman spectra are sensitive to terminal oxygen vibrations ($M = O$) [8]. These atomic displacements and frequencies are known as normal modes of vibration of the molecule. Figures 2.20 and 2.21 show the various types of motion that contribute to the creation of a normal mode. Each normal mode, denoted by Q, can be described as an independent, multi-atom harmonic oscillator with allowed energies given by:

$$G_Q(n) = (n + 1/2)\tilde{n}_Q \tag{2.13}$$

where

$$\tilde{n}_Q = 1/2\pi c\sqrt{k_Q/\mu_Q} \tag{2.14}$$

and where $G_Q(n)$ is the energy of the oscillator in a state labelled by the quantum number n (n = 0, 1, 2, 3, ...), and $\tilde{n}_Q$ is the characteristic frequency (in cm^{-1}) of the oscillator.

In vibrational spectroscopy, electromagnetic radiation is used to excite the normal modes. At room temperature, most normal modes of large molecules may be aptly described with $n = 0$.

This means that, even in its lowest energy state, each of the normal modes of a molecule are moving with energy

$$G_Q(0) = G_Q(1) - G_Q(0) = \tilde{n}_Q \tag{2.15}$$

The ability of a molecule to be distorted by an electric field is referred to as its polarizability α. The induced dipole moment is given by:

$$\tilde{u}_{ind}(t) = \alpha \cdot \tilde{E}(t) \tag{2.16}$$

If there is a change in the polarizability of a molecule it means there will be an active vibrational mode in the Raman spectrum. Bonds possessing covalent character tend to give strong Raman signals because of the change of polarizability associated with the vibration [35].

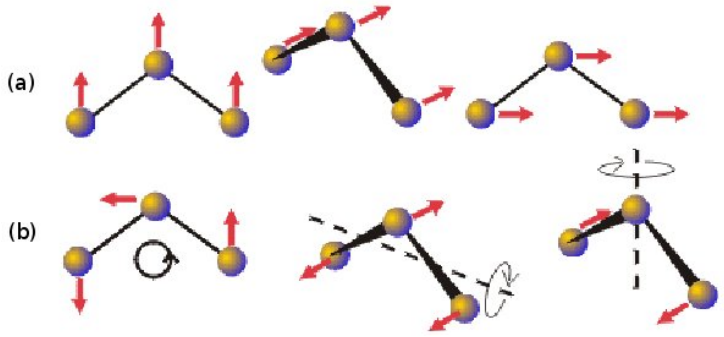

Figure 2.20: Molecular vibrations - (a) $3N$-6 vibrations for a non-linear entity of N atoms, (b) $3N$-5 for a linear entity of N atoms (for N=3 atoms).

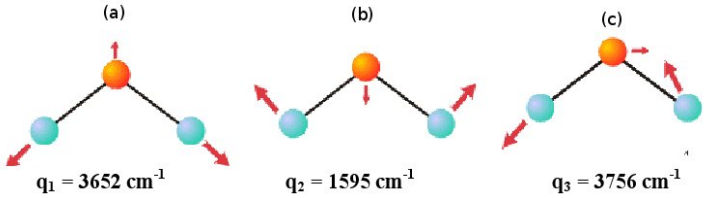

Figure 2.21: Molecular vibrational modes - Since $3N = 9$, this leaves $3N$-6 = 3 vibrational modes: (a) Vibration (q_1) is called the symmetric O-H stretching mode. It can be formed by combining the stretching of the two O-H bonds so that expansions and contractions of the two bonds occur in phase. (b) Vibration (q_2) is the bending mode. (c) Vibration (q_3) is called the antisymmetric O-H stretching mode. It is formed by combining the expansion of one O-H bond with the contraction of the other O-H bond, *i.e.* out of phase.

2.4.2 Raman selection rules

For a molecule with a centre of symmetry, vibrations with symmetrical vibrations are inactive in the IR and vibrations with anti-symmetrical vibrations inactive in Raman scattering [36]. The distortion of a molecule in an electric field, and therefore the vibrational Raman cross section, is determined by its polarizability.

A Raman transition from one state to another, and therefore a Raman shift, can be activated optically only in the presence of non-zero polarizability and dependent on the symmetry of the vibration or rotation [36].

Raman-active vibrations/rotations can be identified by using almost any textbook that treats quantum mechanics or group theory for chemistry. Raman-active modes can then be found for molecules or crystals that show symmetry by using the appropriate character table for that symmetry group.

2.4.3 Confocal laser Raman micro-spectroscopy instrumentation

The intensity of the Raman signal is given by

$$S \sim I_0 \sigma_\lambda N \Omega T_\lambda s_\lambda \tag{2.17}$$

where I_0 is the laser irradiance at the sample, σ_λ is the differential cross section for the Raman line, N is the number of molecules in the probed volume V, Ω is the solid angle of collection of the Raman light, T_λ is the throughput of the instrument, and s_λ the sensitivity of the detector at the wavelength λ. Using microscope objectives for both the illumination and collection of light at the sample was found to be the best way to decrease V and increase Ω and I_0 [31]. By using high numerical aperture (NA) optics the laser beam can be focused to a small volume collecting under a wide angle. The micro-Raman spectrometer can focus the laser down to 5 μm and thus small sample areas in the DAC can easily be probed. A vastly greater amount of local irradiance I_0 can be collected, and due to the wide angle of collection, Ω helps to compensate for the small number of molecules N [31]. Originally the micro-Raman spectrometer was conceived as a confocal microscope.

The pinhole acts as a filter to remove rings and noise and produces a clean point source which is then imaged in the plane of the microscope objective. The pinhole arrangement, as shown in figure 2.22, ensures that only the light coming from the focal plane reaches the detector and that light from the upper and lower planes is partially attenuated. By using a

micro-Raman spectrometer it is possible to discriminate between different depths of the sample allowing "optical sectioning". This arrangement is useful in illuminating stray light from either the background or fluorescence which is outside the focal volume [31].

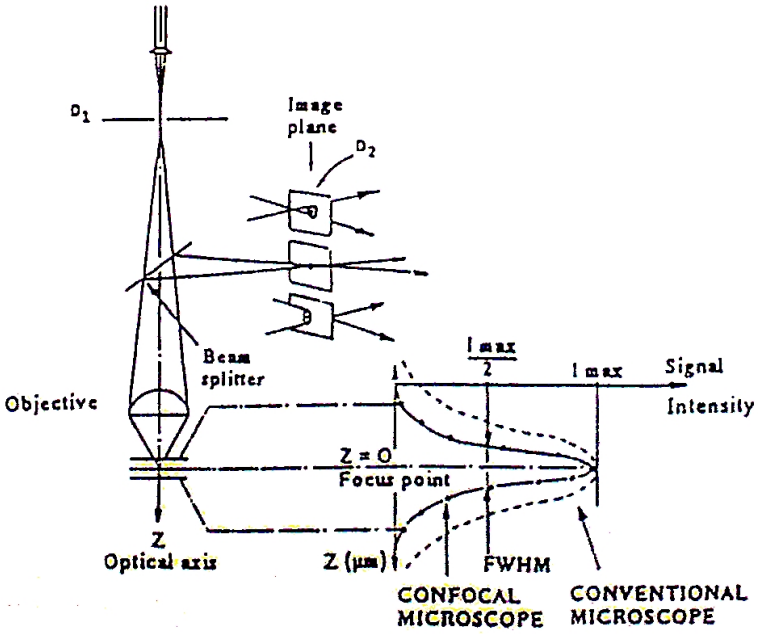

Figure 2.22: Principle of confocal Raman spectroscopy - Comparison of conventional microscope with the confocal microscope setup [31].

2.4.4 Using Raman spectroscopy in the pressure cell

Optical spectroscopic techniques are well suited to probing materials under extreme conditions. Information from pressure induced shifts on inter-atomic binding forces in crystals, charge transfer effects and structural instabilities is obtained from Raman spectra [15]. In the case of the GAC and DAC, measurements can be made quickly on samples with micrometer dimensions [9]. Thermal gradients created by laser heating through the sample is less of a factor when using Raman spectroscopy because the bulk of a material is not probed by spectra taken from localised areas. Care must be taken to minimize the laser-induced heating of the sample as it may alter the surface structure of the bulk metal oxide [8]. However, from the phase diagrams by Ohtaka *et al.* (in figure 2.2), the orthoI phase only starts at approximately 5 GPa for both ZrO_2 and HfO_2 and at about 500°C. Consequently this means that any laser heating from the Raman laser is negligible for the $Zr_{0.5}Hf_{0.5}O_2$ sample. The advantage of using Raman spectroscopy over

IR spectroscopies is that even for non-crystalline compounds, the Raman bands are narrower than IR bands [37]. Other advantages include:

- Characteristic spectra for qualitative identification of compounds/phases.
- Relative lack of interference of adjacent peaks; aqueous solutions not a problem.
- Spatial resolution of $\sim$1 μm (micro-Raman).
- No sophisticated sample preparation necessary.
- It is a non-destructive, *in situ* technique.
- It is relatively fast (spectrum acquisition time 1 sec to 2 min).

Some disadvantages of Raman spectroscopy are:

- Inherent weakness of Raman effect - can be overcome by intense sources (lasers) and efficient detectors (PMT/CCD).
- Fluorescence - can be suppressed by using longer wavelength excitation.
- Not all compounds are Raman active - need complementary technique such as IR spectroscopy to access all vibrational modes.
- Can only probe bulk properties of materials which are transparent to incident laser wavelength (otherwise used as a surface or near-surface technique).

Certain corrections must be taken into account because the observer is outside the crystal in real experiments. These corrections are due to refraction, reflection and transmission of the incident and scattered light at the interfaces and through the anvil windows [34]. The absorption of light by the sample must also be taken into account [34]. It is difficult to take all of these aspects into account experimentally and therefore the measurement of the absolute Raman intensities are rare [34].

2.5 X-ray diffraction

X-ray diffraction is a technique that probes the structure of materials. It is a powerful technique to determine the phase changes of a material under extreme conditions. These changes can be closely monitored to get a good understanding of the nature of the material being probed. XRD is a well known technique and covered extensively in numerous sources. Information contained here is taken from a set of lecture notes by S. Verryn and the texts by B. E. Warren [38] and M. M. Woolfson [39].

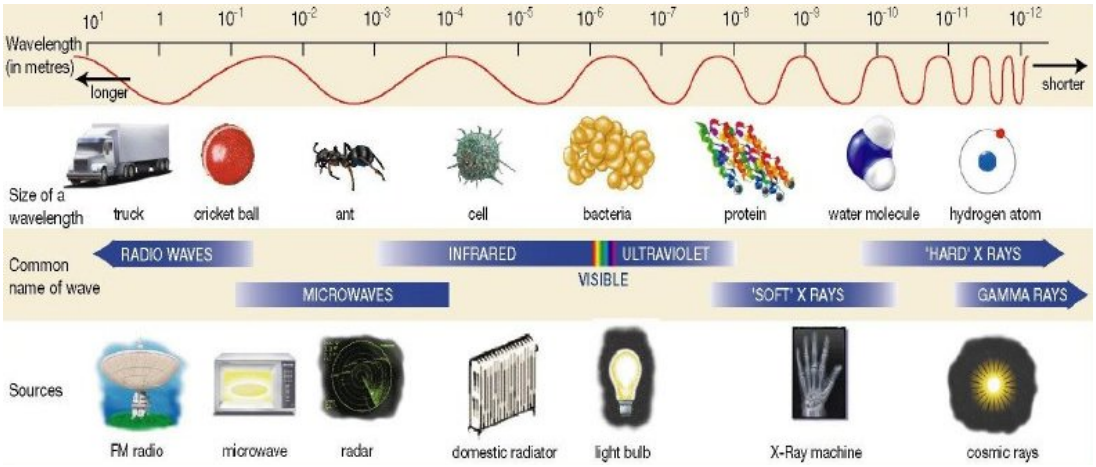

Figure 2.23: Electromagnetic spectrum - The electromagnetic spectrum (modified from Australian synchrotron).

2.5.1 X-ray diffraction theory

X-rays are electromagnetic radiation with wavelengths of the order 0.01-10 nm. This radiation is produced from radioactive materials, electron beams, synchrotron sources, proton bombardment and photons as secondary x-rays. The laboratory based XRD machines use a tube with a hot tungsten filament and electrons are accelerated by a voltage in a vacuum and then strike an anode made of molybdenum in the case of the Siemens SMART diffractometer. Large amounts of heat are produced as a by-product of the process (2% converted into x-rays). Various designs have overcome the challenges of producing x-rays in a tube by incorporating a rotating anode and constant cooling of this anode. Classical scattering theory considers the primary beam an electromagnetic wave with a perpendicular electric field exerting force on the electrons creating radiation in all directions with the same frequency as the primary beam and is called scattered

radiation. Experimentally this unmodified scattering and Compton modified (longer wavelength) scattering is observed. This scattering is incoherent because of the change in wavelength and produces a diffuse background. The unmodified scattering gives rise to Bragg reflections. The wavelength of x-rays are of the order of bond lengths between atoms and is therefore suitable for diffraction measurements as illustrated in figure 2.23, by looking at the region of 'soft' and 'hard' x-rays. X-rays are diffracted off planes of atoms within the cell as if they were reflected. These reflecting planes have an inter planar distance d with an associated scattering angle (2θ) that leads us to Bragg's law (equation 2.18) below. The typical emission spectrum from an x-ray tube is shown in figure 2.24 (a) with a typical Ni-K_β filter. Figure 2.24 (b) shows the typical synchrotron radiation which highlights the high brilliance and the broad range of wavelengths available.

Braggs law:

$$n\lambda = 2d_{hkl}sin\theta_{hkl} \tag{2.18}$$

The d-spacing for an orthorhombic crystal with lattice parameters a, b and c, for example, can be determined by:

$$d_{hkl} = \frac{1}{\sqrt{(h/a)^2 + (k/b)^2 + (l/c)^2}} \tag{2.19}$$

where h, k and l are the Miller indices which specify the reflection plane (a peak in a diffraction pattern).

A powder diffraction pattern consists of a number of rings (as collected via a CCD detector or position sensitive detector). There are numerous randomly orientated crystals (infinite orientations assumed, giving Debye rings on the Edwald sphere in figure 2.25) for any set of planes with spacing d_{hkl} that satisfy the Bragg equation 2.18. This is shown in figure 2.25.

On a laboratory based system the collimator is placed close to the sample which results in a more divergent beam than if placed further away but resulting in the intensity of the beam decreasing. The solution on our system is the inclusion of monocapillary optics.

2.5.2 Monocapillary optics

X-rays are very efficiently reflected off glass surfaces when the angle of incidence is at or below grazing incidence [41]. Monocapillaries function on the principle of total internal reflection of

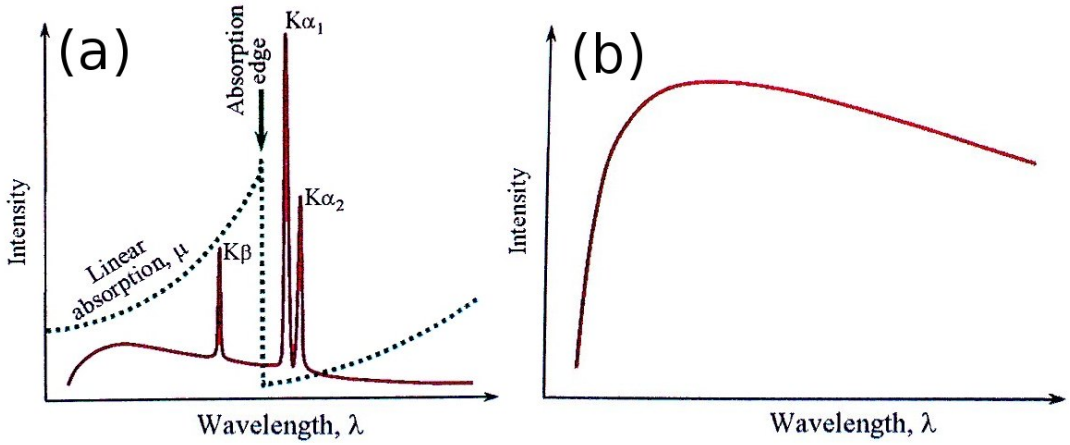

Figure 2.24: XRD spectrum - XRD spectrum from laboratory based diffractometer showing the effect of a Ni-K_β filter as the dotted line, (b) typical synchrotron emission spectrum [40].

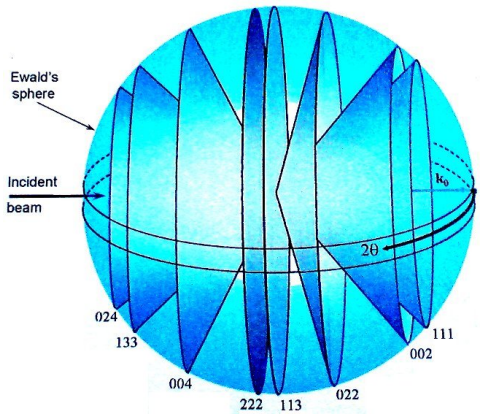

Figure 2.25: X-ray diffraction from a powder sample - X-rays diffract off a powder sample as cones on to the CCD detector or film (image modified from lecture notes).

the x-rays off the glass surface. Monocapillaries are carefully shaped ellipsoidal glass and for single-bounce optics are nearly 100% efficient [41].

Figure 2.26: Monocapillary glass optics - Principle of single-bounce ellipsoidal glass monocapillary [41].

The solid angle from the x-ray source to the capillary is relatively large therefore coupling between the two is efficient. Very high intensities of x-rays can be channelled into the capillary and can be used to generate high intensity micro-beams with diameters as small as 5 μm, with the disadvantage being line widths are increased by $\sim$10% [41]. Monocapillary glass optics display near perfect collimation [42].

2.5.3 Crystallography

Materials are commonly found in the crystal state. Crystals are regular shaped with a high degree of symmetry that possess considerable variation in size and shape. A crystal is a 3-dimensional periodic repetition of a structure. This can be represented as a lattice which is a framework on which the crystal is built. There are 14 Bravais lattices within 7 crystal systems namely, cubic, triclinic, monoclinic, orthorhombic, tetragonal, trigonal and hexagonal. The bravais lattices are made up of unique unit cells which are described as the smallest building blocks to complete the entire lattice and have lattice types: primitive side-centred, face-centred, body-centred, and rhombohedral lattice types. There are 32 crystal systems. There are 230 space groups which are a description of the total symmetry of a crystal.

2.5.4 X-ray diffraction at extreme pressures in practice

The sample volume size for single crystal diffraction studies is not significantly larger than the sample size loaded into the gasket cavity in a DAC and therefore the DAC is ideally suited for XRD studies [24]. The Merrill-Bassett cell made routine XRD studies possible due to its compact and simplistic design [24].

X-rays diffract off lattice planes in solid materials so a clever design is needed for the DAC so that the x-ray beam is free of other solid materials besides the sample during a measurement.

Diamond is a single crystal so when a measurement on diamond using XRD is performed the resulting pattern returns intense spots which are easy to mask out of the powder ring pattern obtained from the sample. The second consideration is the design of the diamond supporting plates, or backing plates. One method is to use solid beryllium backing plates; these plates however diffract along with the sample and can prove tricky in the case where the beryllium lines can't be collimated out on a CCD [22]. The beryllium lines also become more intense and 'spotty' in synchrotron patterns [22]. Using steel backing plates also has challenges because steel is opaque in nature to x-rays. Wide opening angles must be made in the backing plates, requiring larger anvils which are more expensive and the anvil support is also weakened thus lowering the maximum pressure obtainable [22]. Another beryllium-free design is to make the backing plates out of a type Ib synthetic diamond [22]. Brister [43] notes five limitations affecting XRD experiments at extreme pressures. Firstly, the x-ray beam must travel through approximately 5 mm of diamond that absorbs low energy x-rays of about 15 keV and below. Secondly, the effect of Compton scattering from the diamonds as the incoherent scattering from carbon dominates the total cross section over most of the useful x-ray energy range. Thirdly, the exit aperture of the diamond backing plates limits the available access to reciprocal space. Previously this has been overcome by choosing a slit for the exit aperture but only a satisfactory solution when doing energy dispersive diffraction and is problematic for angle dispersive diffraction. Non-hydrostatic pressure environments are the fourth limitation of the MB-DAC but hydrostatic pressure transmission mediums help to reduce or eliminate the pressure gradient over the diamond anvil face. Lastly, the small sample sizes and the corresponding x-ray beam must be matched, requiring the precise positioning of the monocapillary fitted to the SMART diffractometer. Type IIa diamonds would be preferable due to problems with optical viewing with type Ib, but are far more costly [22]. Particular to this study is the use of the novel Boehler-Almax (BA) anvil and special backing plate design shown in figure 2.27.

The BA anvils have the advantage of a larger girdle of 4 mm compared with typical brilliant cut anvils of 2.5 mm. This is to take advantage of the full 80° opening angle of the BA anvil [22]. The brilliant cut and BA anvils have a similar heights of 1.70 mm and 1.95 mm, respectively and path lengths are therefore comparable to standard brilliant cut diamond anvils [22]. The design of the BA anvil backing plate design incorporates a backing plate that is 3.7 mm thick to compensate for the BA anvil being partly embedded in the backing plate shown in figure 2.27, also the exit cone is ground to between 40° and 90°. The anvil seat is ground to 60° to match the 60° conical shape of the BA anvil.

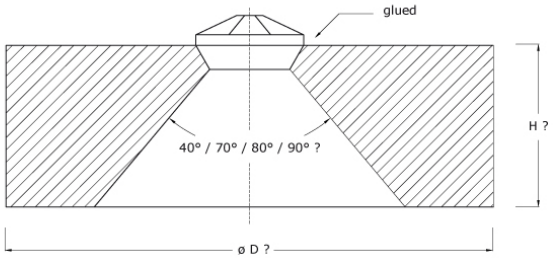

Figure 2.27: Boehler-Almax anvils - BA anvils and backing plate used for XRD wide exit [44]

These wide exit angles are extremely useful on a laboratory based machine as the wavelength typically used is that of Mo-K_α (0.707109 Å). This wavelength is not tunable as is the case with a synchrotron sourced wavelength allowing ~30° (2θ) maximum scattering angle to be measured on the laboratory based SMART x-ray diffractometer (determined experimentally).

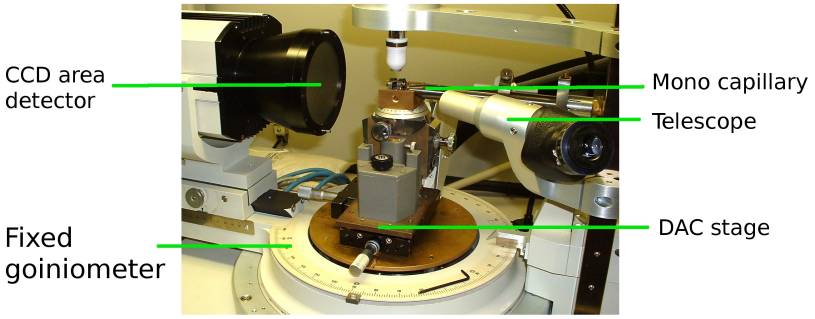

Figure 2.28: Siemens SMART diffractometer - Modified Siemens SMART x-ray diffraction system fitted with a 0.1 mm monocapillary.

Part of the study was to perform preliminary laboratory based experiments on the Siemens SMART diffractometer (figure 2.28) before envisaged synchrotron-based experiments. This included loading the cell, aligning the cell with respect to the x-ray beam and analysis of powder patterns *in situ* using the European Synchrotron Radiation Facility (ESRF) software FIT2D [45].

3

Experimental

In this chapter, the experimental techniques employed during this study will be described. The chapter has been divided into the following sections: sample preparation in section 3.1, high pressure experiments in section 3.2 and high temperature experiments in section 3.3. These sections include the techniques employed in developing the manual fabrication of cubic zirconia anvils, setting up of the Merrill-Bassett miniature pressure cells, anvil mounting, gasket indentation and sample loading. Experimental procedures of confocal Raman spectroscopy through the CZ anvils using two sample types in conjunction with preliminary MB-DAC measurements are discussed. Finally MB-DAC high pressure/temperature experiments using the CO_2 laser heating system and set up is discussed. The phase diagram of the $Zr_{0.5}Hf_{0.5}O_2$ system was explored with XRD in conjunction with Raman spectroscopy.

3.1 Sample characterization

The sample $Zr_{0.5}Hf_{0.5}O_2$ was prepared using the sol-gel process and is well documented in Mojaki's thesis [8]. It was received in powder form and no further preparation was required. The characterization of samples is extremely important in the investigation of materials and their properties. There are various techniques available for sample characterization, with the technique selected dependent on the information required. In this study, Raman spectroscopy and XRD was used.

3.1.1 Raman spectroscopy characterization

Raman spectroscopy was used to establish whether the solid solution of zirconia and hafnia were indeed the same powder used in the previous study (figure 4.1). The 514.5 nm line of a coherent argon ion laser was used, with an interference filter imposed to remove the plasma lines. A power source of 600 mW, reduced to approximately 10 mW on the sample, and a focused spot size of about 5 μm was used. The confocal pin hole of the apparatus used for powder samples was 0.2 mm. A Jobin-Yvon T64000 Micro-Raman spectrometer with BX40 Olympus microscope attachment, fitted with X20 and X50 ultra long working distance (ULWD) objectives was used and spots of about 5 μm could be measured.

3.1.2 XRD characterization

The Brukker D8 diffractometer (Cu-K_α) was used to determine the ambient XRD diffraction pattern (figure 4.12). Some preliminary internal pressure calibration studies were also performed with this instrument but the idea was ultimately discarded due to the broad nature of the peaks from the SMART diffractometer. The scanning range was 25-55° (2θ) using the step size of 0.014° and step time of 7327.2 s at room temperature (25°C). This ambient pattern was used to compare against the end members ZrO_2 and HfO_2. The low pressure XRD data measured in the MB-DAC was also compared with the ambient pattern.

3.2 High pressure experiments

Static high pressure experiments were carried out using the MB type anvil cell. The exploded view of the cell is shown in figure 2.14 in section 2.2.2 and the cross section is shown in figure 3.1. Initial experiments were performed using CZ anvils polished using a manual fabrication method developed in our high pressure laboratory at the School of Physics at WITS. The sample was then subjected to even higher pressures using the MB-DAC loaded with one Boehler-Almax anvil and one brilliant cut diamond anvil. High temperatures were achieved by using the in-house CO_2 laser heating system. The samples were then analysed with Raman spectroscopy and XRD.

3.2.1 Manual fabrication of CZ anvils

For the gem anvil experiments brilliant cut CZ single crystal gems of 170 mg (∼0.85 carat) with a 5 mm girdle obtained from commercial suppliers were used. The composition of the anvils was

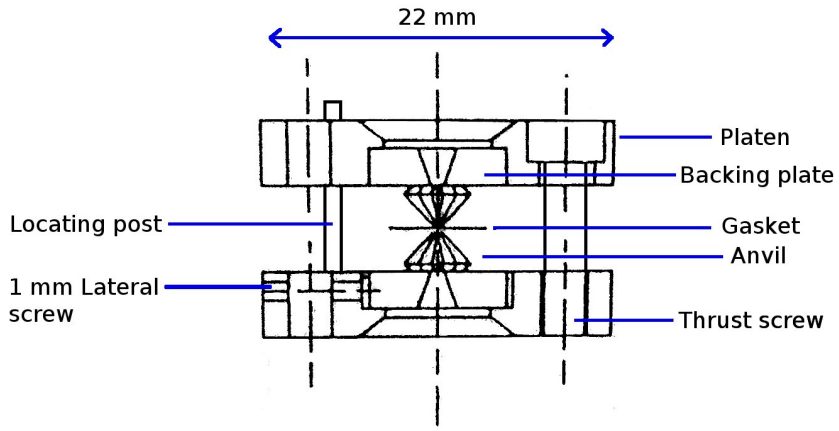

Figure 3.1: Merrill-Bassett cell - Cross section view of the miniature MB-DAC with a total diameter of 22 mm [23].

CZ stabilized with 10-mol% Y_2O_3. The program of hand polishing was continued after initial experiments conducted several years ago by Professor G. R. Hearne. CZ anvils had previously been machine polished in the School of Physics at WITS.

The hand polishing technique required three steps. The same polishing mats and lubricants are used in the hand polishing method as in the machine polishing method. These comprise of SiC 4000 grit polishing mat, UltraPrep self adhesive Diamond Lapping Film of 1 μm, 0.5 μm and 0.01 μm, MetaDi Diamond Suspension monocrystalline spray and MicroCloth self adhesive obtained from Apollo Scientific cc. [46]. The polishing mats are stuck to a glass sheet to create a sufficiently flat polishing surface.

Referring to figure 3.2, the CZ (iv), is mounted in the holder as shown. The gem is mounted with the table of the CZ on the stainless steel adjusting screw (i), (polished parallel to the stainless steel polishing ring (ii)). The CZ can be adjusted up and down by turning this screw. The CZ is clamped on the top by a locating plate (iii) that is tightened by the three screws. The CZ needs to be constantly adjusted up or down depending on the degree of rounding and the required final anvil size. With the tip of the gem protruding it is blunted off using a SiC 4000 grit polishing mat following a figure of eight or forward-back pattern. Constant downward pressure on the anvil and holder is required for a high quality, symmetrical culet. The tip must be adjusted so that it does not cause the holder to wobble or spin on the mat. This fine adjustment achieves very precise parallel polishing of gem tip with respect to the table. The culet can be viewed in the holder through the hole (v) in the adjusting screw (i).

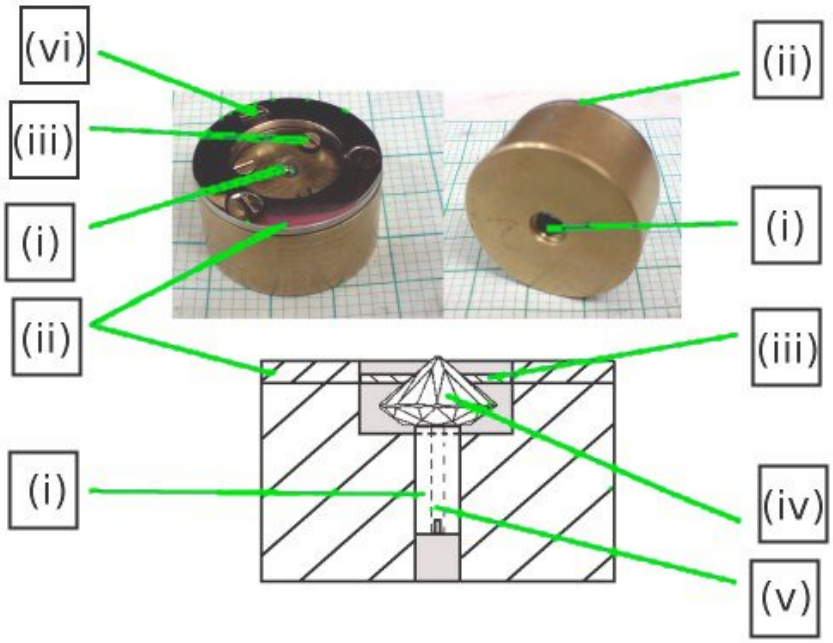

Figure 3.2: CZ anvil polishing holder - CZ anvil polishing holder showing the top, bottom and cross-section (labels defined in the text).

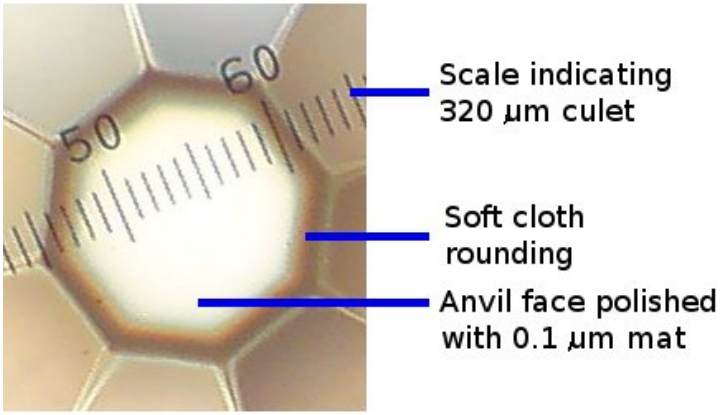

Figure 3.3: CZ culet final soft cloth polish - Edges polished round by the 1 μm soft cloth.

The culet is polished with the SiC 4000 grit polishing mat until it is 20-40 μm larger than the desired culet size. The soft cloth is used to round the edges of the culet octagon giving a rounded bevel shape to the anvil face similar to the bevel on diamond anvils as shown in figure 3.3. The next step is to polish using a 1 μm diamond impregnated polymer polishing mat keeping a constant downward pressure. It is necessary to alternate between the 1 μm polishing mat and the soft mat with diamond lapping spray to round off the corners and edges of the anvil. This technique is used to relieve the stresses at the edges as they tend to crack and chip and thus contaminate the polishing mats with hard CZ chips which scratch the anvil face during subsequent polishing. If the finished CZ anvil has any defects such as chips and scratches there is a likelihood of the anvil failing at lower pressures.

The 0.5 μm and 0.1 μm polymer polishing mats are used to polish out any micro-scratches and to give a higher quality finish to the culet. When the culet is viewed under a microscope at 20X magnification, there should not be any visible scratches. The culet face should be fully illuminated without optical shadow effects when adjusting the light level. If asymmetric shadow effects are observed, it could indicate non-uniformity on the culet face. A final test of parallelism and circular symmetry of the culet is to remove the finished anvil from the polishing holder; clean it thoroughly and try balance the anvil on the culet face on a glass slide and view the Newton interference fringes through a microscope as illustrated in figure 3.4.

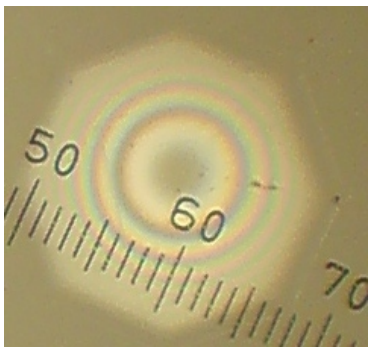

Figure 3.4: CZ anvil balancing test - CZ anvil balancing on the culet. The circular Newtons rings are very nearly centred and this anvil displays the characteristics of a well polished anvil.

If the anvil is of satisfactory quality and flatness it will balance on the culet and secondly the interference fringes will be circular and originating from the centre of the culet as in figure 3.4. If the rings are broad, the anvil has a relatively flat surface and if there are many fine rings, the anvil face is relatively rounded (see equation 2.5). Indications of a poorly polished anvil is that

the anvil does not balance as a first test and second if it lists and balances off centre creating more oval shaped interference fringes.

3.2.2 Diamond anvils

Diamond anvils are typically manufactured by Almax industries [44]. The top anvil used was a Boehler-Almax anvil of 0.55 carats and a 5 mm girdle of type Ia polished with an exit cone of 83°, and a culet size of 550 μm with an 8° bevel. The bottom anvil was a brilliant cut diamond of 0.55 carats and 5 mm girdle of type Ia, with a culet size of 650 μm with an 8° bevel.

3.2.3 Anvil mounting and alignment

The backing plates (BP) were polished by hand to a mirror finish and have 1 mm exit holes opening up in a cone of 60° for the top anvil and 80° for the bottom BA anvil. A holder (figure 3.5) clamps the anvil on the top with a screw (i) tight onto the backing plate (iii), and was then centred with three lateral adjustment screws (iv). The anvils, whether gem or diamonds, were mounted on the backing plates with a high temperature epoxy; Stycast (mixed with catalyst 9) and is stable to ∼200°C. The epoxy was de-gassed after mixing with the catalyst using a vacuum pump. By viewing from the bottom, the backing plate was moved such that the hole in the BP aligns with the culet by changing the focus on the microscope. The culet and the 1 mm hole must be concentric. The use of an inverted microscope such as the Olympus BX70 helps to achieve this, or a vertical telescopic system can be constructed using cross hairs or a similar arrangement can be used to get the culet and BP hole concentric.

The thrust plates (TP) with the BP secured on them were brought together with a glass slide between the anvils. Figure 3.6 shows the Newtons interference fringes (broad and fine fringes between the two separate glass/diamond interfaces). The fringes must disappear for both interfaces with the culets concentric by adjusting the lateral screws of the moveable BP and the three pressure generating thrust screws (that tilt the TP).

With the parallelism and concentricity of the culets completed, the screws were marked with a reference position. The height of the TP was measured at each thrust screw and noted as the reference of parallelism and concentricity (which was used when indenting the gasket and generating pressure). A final check that the anvils were polished parallel to their respective tables, was to recheck that these thrust screw height measurements were all within ∼150 μm of each other and were equally tight.

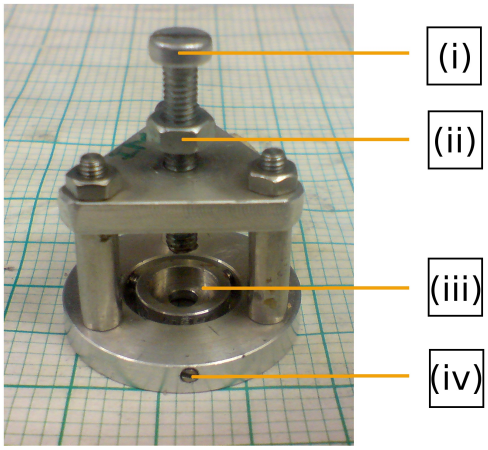

Figure 3.5: Gem alignment holder - Gem alignment holder for centring anvils on the backing plate. (i) Clamping screw, (ii) clamping screw lock nut, (iii) backing plate seat, (iv) lateral adjusting screws to centre backing plate on culet.

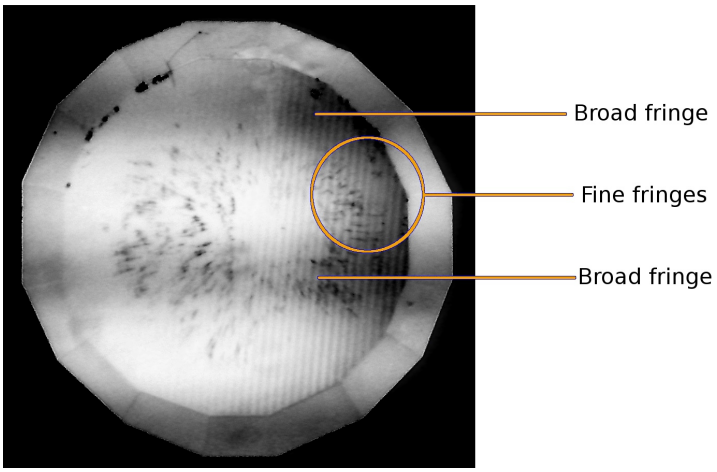

Figure 3.6: Newtons interference fringes for the diamond-culet/glass interface - Straight fine and broad fringes of the (flat) diamond/glass interface of each anvil indicating that the culets are not parallel. The anvil culet diameters are 550 μm for the brilliant cut diamond and 650 μm for the BA culet.

3.2.4 Gasket fabrication

The glass slide was removed and a metal gasket of approximately 200 μm sandwiched between the anvils and the screws closed to the reference positions mentioned above. Initially stainless steel 301 (SS301) was used with the CZ anvils but the anvils cracked in the indentation phase. CuBe was then used but determined to be too soft, as the cavity deformed at pressures below 10 GPa. Experimentally $Ta_{90}W_{10}$ was found to be suitable. The gasket material was cut to about 0.25 cm^2 and fixed parallel to the culet using non-permanent sticky clay or positioned on the vertical posts. The gasket was marked so that it can be returned to the same position after the sample cavity is drilled. During the pre-indentation period, the anvils are most likely to break due to the radial extrusion of the gasket material putting maximum tensile stress on the anvils' tip [24].

The recorded relative heights are kept constant during the indentation of the metal gasket. It was indented at 5 to 15 μm intervals and pressures of up to 2 GPa are possible [23]. It was also required that the gasket be left for tens of minutes to let the stresses in the metal relax, or the cell opened periodically during this indentation process. A hole was then spark eroded in the centre of the indent. The diameter was determined by the maximum pressures needed. The bigger the ratio between the cavity diameter and the culet (indent) diameter, the higher the pressures the gasket can support [24].

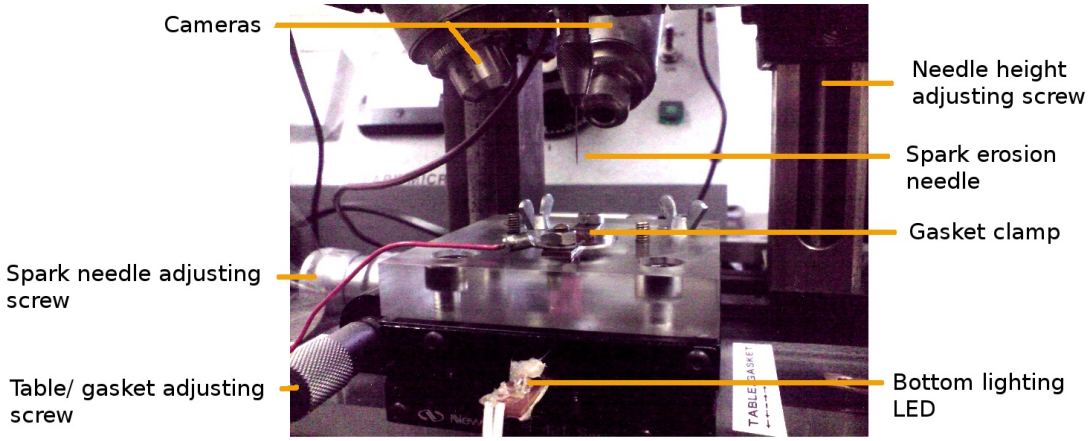

Figure 3.7: Spark erosion machine - Spark erosion machine used to start the hole in the gasket material after which a pin vice and micro drill are used to clean up the hole.

The gasket was inserted centrally in the clamp of the spark erosion machine (figure 3.7) so that it was visible on both cameras. The needle was centred on the indent. Dielectric liquid of

paraffin or alcohol was dropped in the indent. The coarse screw was used to lower the needle to within a few millimetres of the indent and then the fine adjustment screw used for sparking. The gasket can be removed and inspected at various stages and corrections made. The cavity was then cleaned out and fine tuned with the use of a micro-drill bit of between 100-200 μm (figure 3.8). Once the gasket was drilled it was inspected to ensure the cavity was drilled centrally on both sides of the gasket. The hole can be spark eroded before the final indent thickness is achieved as with further indenting the hole will close and relieve some of the stresses on the anvils. In our experience, a cavity with a final diameter of about a 1/3 of the diameter of the gasket indent, is optimal.

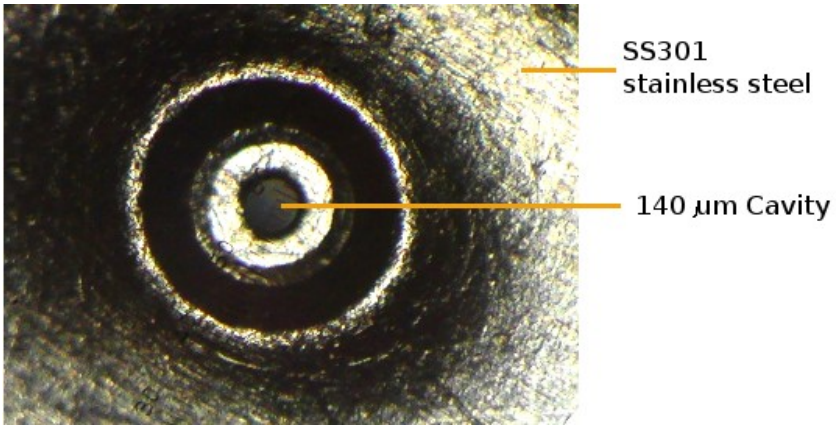

Figure 3.8: Gasket indentation - SS301 stainless steel foil of starting thickness 200 μm. Indent with 140 μm diameter cavity sparked and drilled.

At this stage, the parallelism and concentricity of the anvils was rechecked and any new references noted. The cell has undergone pressure during the indenting stage and the thrust and backing plates have had a chance to seat themselves in their final positions. It was expected that there would be a small change in reference heights.

3.2.5 Sample and ruby loading

Sample powder was collected on a surgical needle and placed in the indent of the gasket (with the top TP removed) while monitoring through a microscope. The top TP assembly was then slid onto the posts and clamped down between fingers thus pressing the powder into flakes in the indent. The TP was then removed and pieces of sample flakes manoeuvred into the cavity, after the excess powder was cleaned away. Usually 2-3 ruby balls are loaded onto the centre of the top anvil face. It is difficult to control where the ruby balls and sample flake end up after the

PTM is loaded into the cavity and sometimes several loading attempts are necessary to ensure a satisfactory distribution of sample flakes and ruby balls.

3.2.6 Pressure transmitting media (PTM)

The final experiments relied on three types of PTM. These were Si-oil for the TiO_2 experiment, Fluorinert (FC70/FC77, 1:1) for the TiO_2 and $Zr_{0.5}Hf_{0.5}O_2$ sample loading experiment in the MB-GAC. Fluorinert was used in the 20 GPa experiment and liquid Ar for the MB-DAC CO_2 laser heating experiment in the MB-DAC. The Si-oil and Fluorinert are liquids that are loaded with a needle and dropped into the cavity. Argon is a gas at room temperature but must be loaded in its liquid form. To achieve this, the Ar gas was liquefied using liquid nitrogen (N). The boiling temperature of Ar is 87 K and that of N is 77 K [26]. The method is described in section 2.2.4. The DAC was pre-cooled in liquid nitrogen and then the liquid Ar poured into the vessel. The Ar droped into the vessel and gently creeped into the sample cavity. Wittlinger [26] states that only weak convection arises in the liquid Ar which is necessary if the ruby and sample are to remain undisturbed and not washed away from the diamond surfaces. After the PTM was loaded, the cell was closed to the reference marks to increase the pressure to between 0.5-1 GPa to ensure the PTM was sealed in the cavity. This was checked via ruby fluorescence.

3.2.7 Pressure measurements

Using the standard ruby fluorescence technique, the pressure was evaluated by monitoring the $R1$ fluorescence line shown in figure 3.9. Initially three thrust screws are employed to create pressure in the MB cell. After the cell was closed to seal the PTM in the cell, the pressure was between 0.5-1 GPa. The screws were tightened slowly to protect the anvils from failing. The pressure response to tightening the screws and screw reference positions were closely monitored. By experimentation it was determined desirable to increase pressure in steps of about 1 GPa. Constant checking was important at higher pressures, especially when using CZ anvils. A 20 mW, 532 nm green laser was used as an excitation source. This was coupled to an Ocean Optics, USB-2000 or HGR-4000, spectrometer and optical fibre to the trinocular turret of the Olympus BX60 compound microscope. At ambient conditions (in our laboratory) the $R1$ line was located at 695 nm. The fluorescence was collected via a 200 μm optical fibre and displayed using the software package Ocean Optics Spectra Suite. Two additional internal pressure calibrants were tried, NaCl and Pt Black, with the $Zr_{0.5}Hf_{0.5}O_2$ sample using XRD. It was found that it

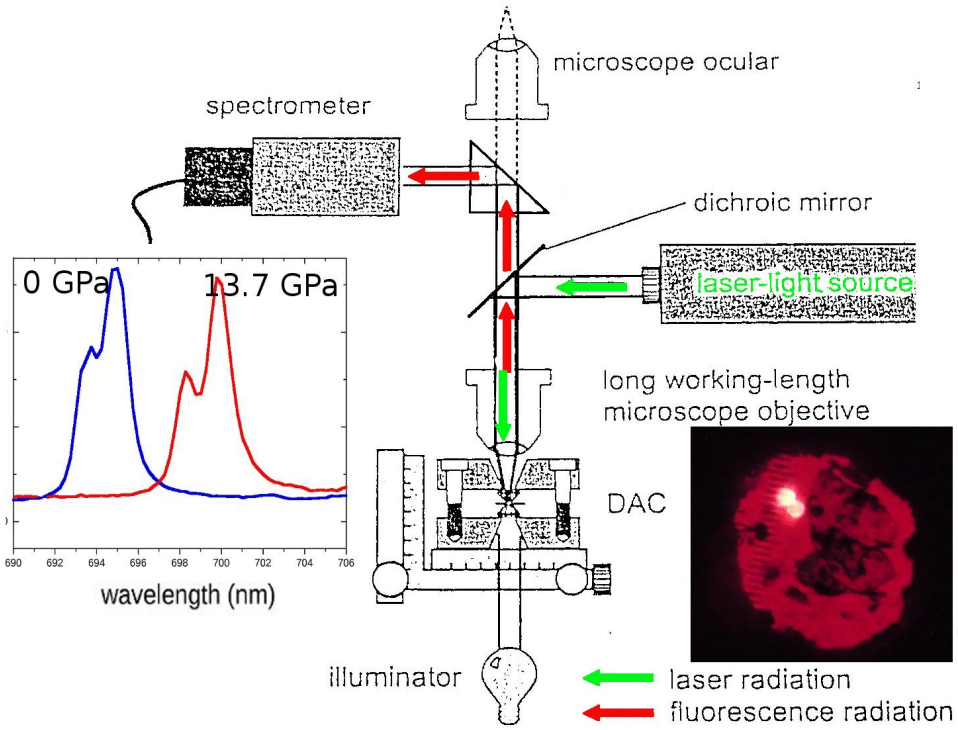

Figure 3.9: Ruby fluorescence microscope - A 20 mW, 532 nm green laser excitation source, Ocean Optics USB-2000 or HGR-4000 spectrometer, coupled to a 200 μm optical fibre to the Olympus BX60 compound microscope.

was difficult to get quantitative data from the diffraction patterns using the current set up as the peaks were too broad. The idea was consequently discarded.

3.2.8 Gem anvil cell (GAC)

Initial high pressure work was carried out by static compression in the MB-GAC. The orthoI phase of $Zr_{0.5}Hf_{0.5}O_2$ starts evolving at 5 GPa . Using static compression in the MB-GAC in conjunction with the hand polished CZ anvils it makes for a good initial experiment on the $Zr_{0.5}Hf_{0.5}O_2$ sample. Pressures of up to 10-15 GPa were anticipated with this set up considering the preliminary experiments to ∼13 GPa. The preparation of the CZ anvils in the MB cell is similar to the method described in sections 3.2.3 to 3.2.7 above for the MB-DAC. Initial Raman measurements were performed on the strong scatterer TiO_2 using the confocal pinhole in triple subtractive mode to determine if the CZ anvils created a significant detectable background. The laser was focused inside the CZ anvil and on the TiO_2 sample and compared. Si-oil was used as the PTM. Pressure generated on imperfectly polished CZ anvils reached 5 GPa. Further experiments were done at ambient conditions on a glass slide. Measurements on Si-oil and Fluorinert were compared. TiO_2 and $Zr_{0.5}Hf_{0.5}O_2$ Raman intensities were compared as well as the Raman spectrum of the CZ anvils themselves. These experiments helped show the possible Raman bands that may contaminate the spectrum of our sample at pressure. The experimental parameters of the Raman spectrometer were also explored and gave valuable information to use in the pressure experiments. In the final MB-GAC experiment both TiO_2 and $Zr_{0.5}Hf_{0.5}O_2$ were loaded into the same cavity as shown in figure 3.10.

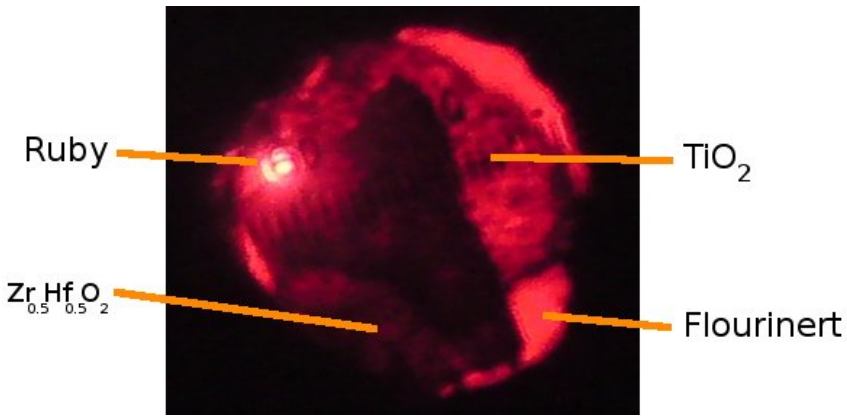

Figure 3.10: Two samples TiO_2 and $Zr_{0.5}Hf_{0.5}O_2$ in the MB-GAC - TiO_2 and $Zr_{0.5}Hf_{0.5}O_2$ loaded into the same cavity.

3.2.9 Diamond anvil cell (DAC)

The MB-DAC (W302 #1) was loaded with the BA anvil with culet size of 550 μm with 8° bevel. The brilliant cut diamond was mounted on the bottom BP and had a culet size of 650 μm with 8° bevel. For the second run using liquid Ar as the PTM and laser heating experiments, the INC718 #1 MB-DAC was loaded with a BA anvil on the top backing plate (BA anvil still mounted on W302 #1 backing plate used) and the brilliant cut diamond on the bottom BP. A stainless steel SS301 gasket of ~200 μm starting thickness was used in both cases for the XRD pressure measurements and a ~200 μm cavity was drilled. The side view of the cell is shown in figure 3.1 and the cooling of the MB-DAC shown in 3.11 after it had been loaded with the liquid Ar PTM.

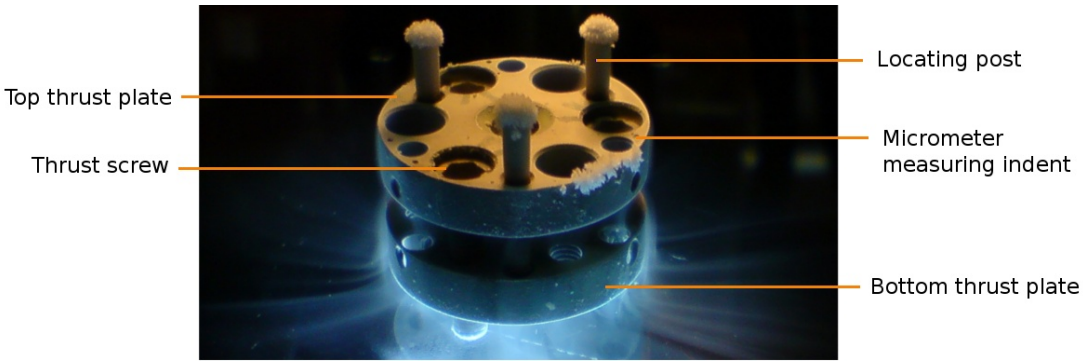

Figure 3.11: 22 mm diameter MB-DAC - MB-DAC cooling after liquid Ar loading.

3.3 High temperature experiments

The two methods available for heating the MB-DAC were furnace heating and laser heating. It was decided to laser heat the cavity to avoid damage to the diamond anvils and the glue. The INC718 cell is designed to handle temperatures of ~700°C. Liquid Ar was loaded into the 160 μm cavity is shown in figure 4.11 to insulate the sample from the diamonds.

3.3.1 CO_2 laser heating the MB-DAC

The system was aligned to try to focus the beam on specific parts of the cavity. The heated regions were measured with Raman spectroscopy. The reference positions (unheated by the laser) displayed no clear evidence of heating between the heated and unheated regions. The entire cavity was then heated by raster scanning because specific areas could not be reheated

once the cell was moved. The advantage of heating the entire cavity was that XRD measurements could be performed and qualitative data obtained for direct comparison to the first high pressure run.

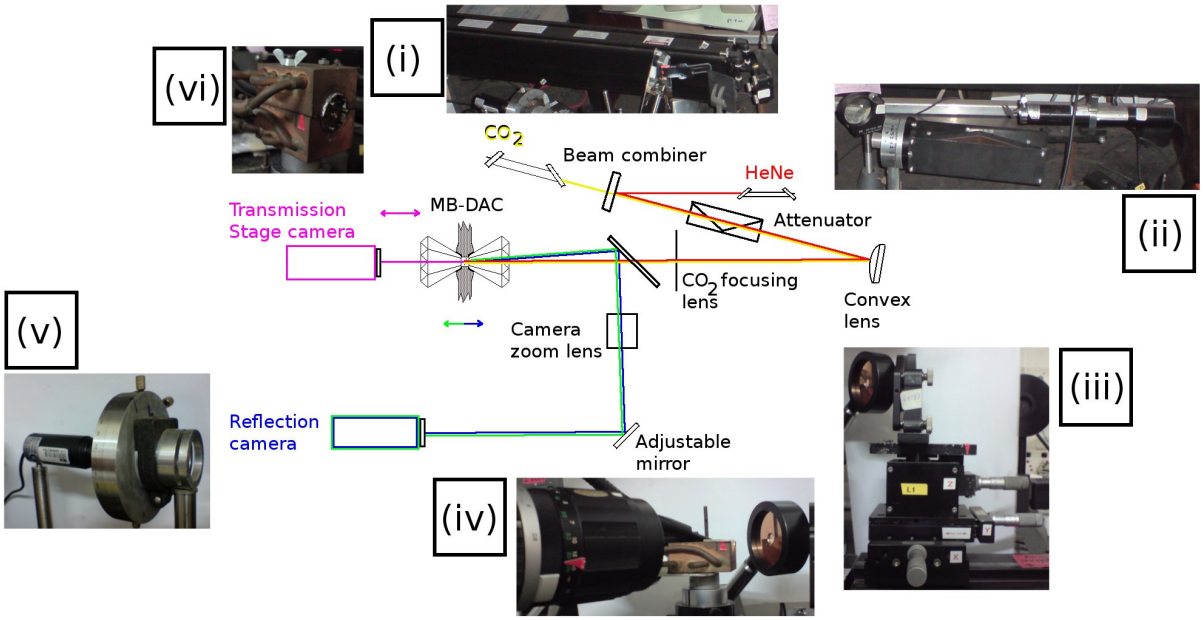

Figure 3.12: CO_2 laser heating facility details - (i) 30 W continuous wave CO_2 laser, (ii) attenuator and HeNe laser behind it, (iii) ZnSe CO_2 focusing lens on three-axis stage, (iv) copper reflecting mirror with hole cut in for the laser to pass through and zoom lens, (v) bullet camera with polariser and (vi) MB-DAC mounted in water cooling jacket.

Figure 3.12 shows the laser heating system. It consists of a co-linear 30 W continuous wave CO_2 laser and HeNe laser that are combined by the beam combiner. The CO_2 laser was focussed onto the sample by a ZnSe lens mounted on a three-axis stage. The alignment of the sample was achieved by using the test sample (Al_2O_3). The test sample was heated until emission was reached so that this emission spot could be monitored with both the cameras. The copper mirror is used to reflect the laser light through to the "reflection camera" as marked in figure 3.12. A 50:50 beam splitter can be fitted that allows half of the emitted light to the camera and half to the optical fibre for temperature measurements. Temperature measurements were unsuccessful due to hot spot alignment problems. The temperature was estimated from sample melting experiments done outside the DAC cavity. The zoom lens achieves a magnification on the monitor of ~220X. The second colour CCD camera was installed on the sample stage utilising the built-in lens giving a modest magnification of about 10X. This was further magnified

by zooming the picture via the software. The position of the emission spot was marked on both of the screens as a reference. The DAC was then placed on the stage and the sample cavity illuminated with the cold light (light transmitted through bundled fibre optic glass cables [47]) and the laser reference spot and cavity moved to be on top of each other by means of the sample stage. This ensured that the laser beam was positioned on the cavity. Confirmation that the system was correctly aligned was that the camera seemed to pick up radiation from the CO_2 laser through the cavity and it was then a matter of observing this spot on the screen and raster scanning over the cavity. The sample stage is water cooled and the MB-DAC is constantly cooled to avoid damaging the type Ia diamonds that have high thermal absorption at 10.6 μm wavelength. The absorption by the diamond anvil window (type-Ia, 2 mm thick) could be as high as 70% [48]. There was no emission during the laser heating experiment and it is believed that temperatures lower than 1000°C were achieved. The 10.6 μm wavelength of the CO_2 laser beam was focused to $\sim$50 μm into the second diamond but attenuated by the sample and cavity contents. This set up results in the laser not being focussed into the front diamond, avoiding damage.

3.3.2 High pressure Raman spectroscopy

The Raman effect is described as frequency shifts that are either positive (resulting in anti-Stokes Raman lines) or negative (resulting in Stokes Raman lines) when light is scattered by molecules. The Raman shifts correspond to vibrational energy changes in the scattering species and therefore display characteristic fingerprints. A Jobin-Yvon T64000 Micro-Raman spectrometer with BX40 Olympus microscope attachment, holographic gratings (1800 grooves mm^{-1}) and a liquid nitrogen cooled CCD detector with a 514.5 nm laser line of Ar^+ with output of 55 mW was used. The darker regions of the sample in figure 4.11 are labelled (A), (B), (C), (D) and (E) and gave the best signal to noise ratio when measured by the Raman laser. The sample was specifically pressed thin (10-20 μm thick, and near transparent), for efficient heat dissipation when laser heating. There is a fine balance between heat dissipation and being able to measure the thin sample with Raman and XRD. In Raman spectroscopy, most of the probing radiation was in fact transmitted rather than back-scattered. The diameter of the laser spot at the sample was 5-10 μm. The entrance slit width of the pre-monochromater was set at 150 μm. The confocal pinhole was set to between 100-200 μm to reduce the depth of the focal plane region as much as possible and thus to minimise sampling background signal from the CZ anvil. Under these conditions data acquisition times for each spectrum was between 5-8 minutes for the CZ anvils

and 8 minutes in the case of the laser heated MB-DAC. The maximum Raman laser power was set between 600 and 700 mW.

3.3.3 High pressure XRD

XRD data has been obtained using the modified Siemens SMART equipped with a 1K CCD detector based in the structural chemistry group in the School of Chemistry at WITS. The system consists of a conventional x-ray generator with Mo-$K\alpha$ radiation (λ= 0.71073 Å). The beam was directed normal to the diamond table and culet through a 0.1 mm monocapillary. Angle-dispersive diffraction patterns were in the form of Debye-Scherrer powder rings recorded on the 512 x 512 pixels of the area detector. A special stage was built for the SMART x-ray diffractometer. It has three-axis manipulation as well as tilting and rotation of the MB-DAC as shown in figure 3.13. MB-DAC is positioned in a "V" such that the cavity/sample of the MB-DAC is in the same place as if a crystal sample is mounted on the standard goniometer. This allows for correct sample to detector distance determination by means of the built-in viewing telescope. The cavity was then further manipulated by optimizing the count rate through to the CCD by adjusting the MB-DAC horizontally and vertically.

A new 0.1 mm monocapillary was attached to the x-ray tube and the beam is totally internally reflected and focused into a narrow beam. The 'OPTICAL' setting on the SMART [49] software rotates the goniometer and stage 30° 2θ so that it was aligned with the optical telescope. The MB-DAC was then put back into the zero position. The beam stop was then fitted taking care not to disturb the DAC.

Two dark field measurements were taken and averaged and automatically subtracted out of the powder ring pattern [49]. The length of acquisition (30 minutes) was determined experimentally to give the best sample signal to noise ratio. Few adjustments had to be made to get an uncontaminated powder pattern as the gasket would sometimes give strong powder rings. After each pressure increase, the set up process would have to be completed. As the backing plates provide limited 2θ reflections, the stage can be skewed to get the outer rings. Once the powder pattern has been collected the SMART software [49] unwarps the rings and the powder ring pattern imported into the FIT2D program [45]. This program converts 2-dimensional powder ring patterns into a powder peaks pattern and requires manual input of instrument parameters, like detector to sample distance and pixel size must be calculated.

To determine the pixel size (calculated to be 122.3 μm), the dimensions of the detector are divided by the number of pixels. The sample to detector distance was calculated by taking two

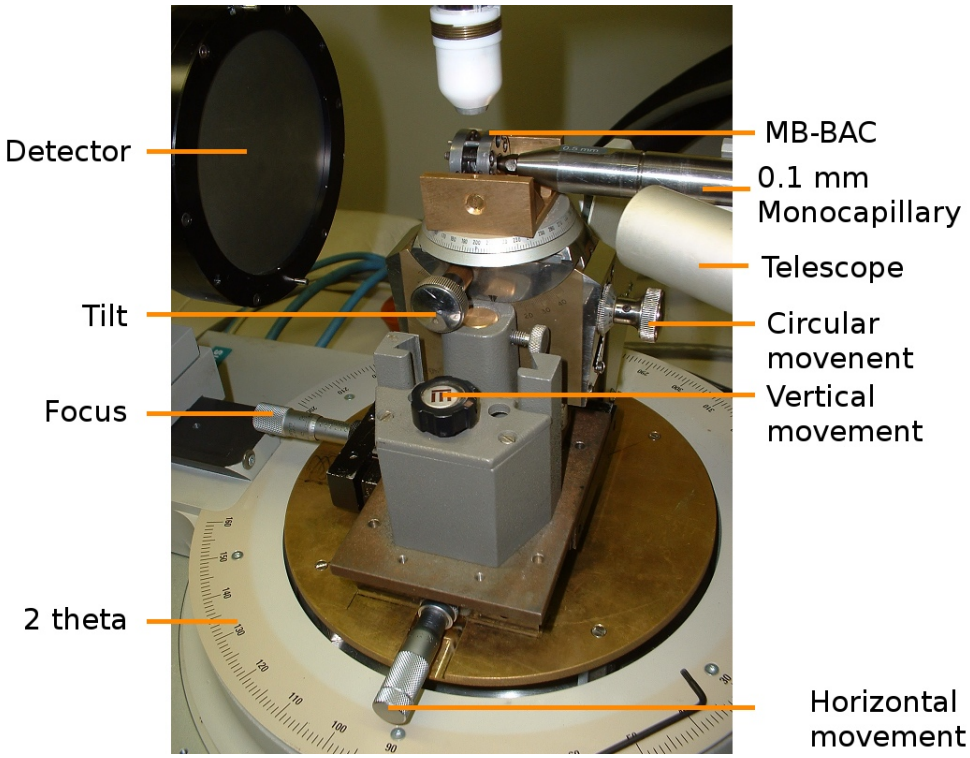

Figure 3.13: Siemens SMART MB-DAC stage - MB-DAC loaded onto the stage. The beam stop is not fitted in this figure.

different sample to detector measurements and calculating where the face of the 2-dimensional detector was exactly positioned with respect to the sample. This was calculated to be 7.687 mm added to the detector distance used in the FIT2D program.

The DAC was removed from the purpose built stage (figure 3.13) to increase or decrease pressure and heat the sample. Initially some experimentation was performed to determine the optimal time and detector distance settings. 60 mm, 45 mm and 35 mm were chosen and 10 min, 15 min and 30 min for each detector distance and time respectively. 45 mm was calculated to be the optimum distance from the detector to sample, however it was found experimentally that 35 mm (30 minutes) was a better compromise due to the dark field subtraction (dark field impinges on the pattern as shown in figure 3.14).

In a similar way as shown in figure 3.14 the XRD lines were identified. We compare the Ar lines to the end members ZrO_2 and HfO_2 to both the orthoI and orthoII XRD patterns. We look at the gasket interference lines and describe any of the other prominent features in the diffraction patterns. As the pressure increases the gasket hole closes and further intrudes into the diffraction pattern. Figure 3.14 is an example of the raw powder rings and the resulting integration of these rings using the FIT2D program.

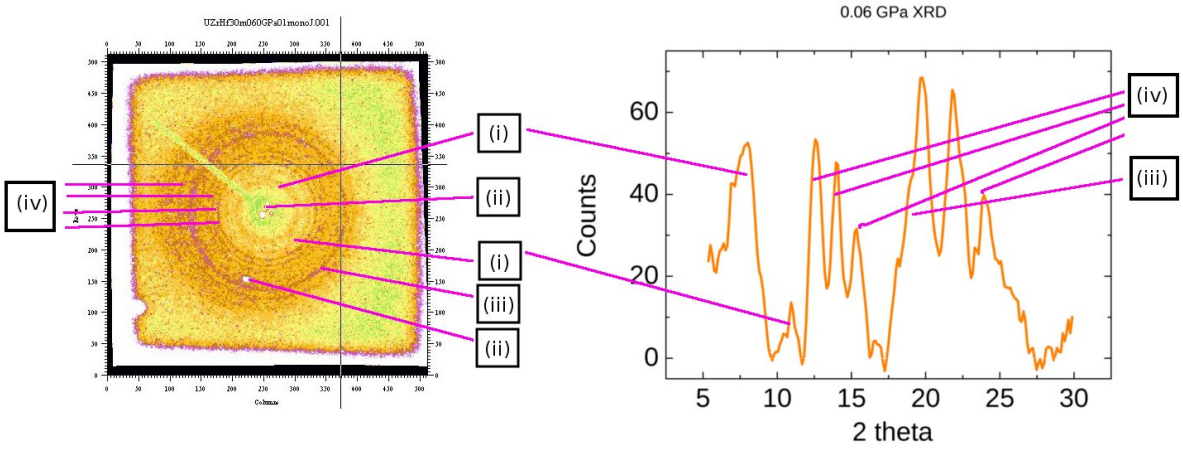

Figure 3.14: XRD peak identification - Figure showing identification after integration using FIT2D, of raw data from the SMART XRD diffractometer. Dark field subtraction has not been done as can be seen by the white border in the ring pattern. The MB-DAC was prepared with a SS301 gasket, loaded with Fluorinert PTM, $Zr_{0.5}Hf_{0.5}O_2$ sample and ruby balls. (i) Unknown peaks, (ii) diamond spots, (iii) gasket and unknown peaks and (iv) monoclinic sample peaks.

4

Experimental Results and Analysis

This chapter will be a logical flow of results obtained using the various experimental techniques learned with discussions included. High pressure techniques were learned by using gem anvils in the Merrill-Basset cell. A new cubic zirconia manual anvil fabrication technique was developed and the CZ gems' usefulness demonstrated for two extreme sample scattering cases, TiO_2 and $Zr_{0.5}Hf_{0.5}O_2$. Following these preliminary high pressure studies and Raman spectroscopy measurements, diamond anvil cell techniques were used. Pressures of up to 20 GPa were explored. The final part of the study used a combination of high pressure and high temperature by means of CO_2 laser heating. These techniques were used to investigate the response of the $Zr_{0.5}Hf_{0.5}O_2$ sample in conjunction with cryogenic PTM loading. Raman spectroscopy analysis techniques were used on both the MB-GAC and MB-DAC, while XRD was used exclusively on the MB-DAC. The results will be compared to the preliminary results obtained by Mojaki [8] and additional data will be presented on the P-T response of this compound as deduced from XRD and Raman data.

4.1 Ambient Raman and XRD measurements on $Zr_{0.5}Hf_{0.5}O_2$

Ambient measurements were performed on the $Zr_{0.5}Hf_{0.5}O_2$ powder sample. These were to obtain a reference Raman spectrum and reference XRD diffraction pattern for comparison with the high pressure-temperature modified sample. Figure 4.1 shows the Raman spectroscopy results, while the XRD results are shown in figure 4.12 of section 4.3.2. Additionally, the Raman spectrum was used to compare with the original Raman spectrum taken by Mojaki [8] and thus a direct comparison could be made to their results.

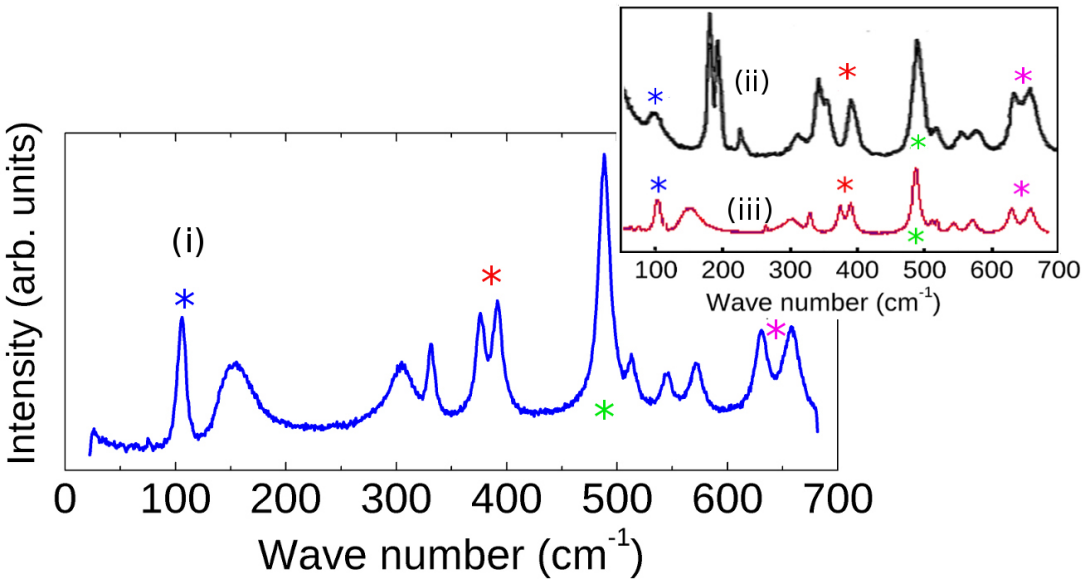

Figure 4.1: Raman $Zr_{0.5}Hf_{0.5}O_2$ powder - (i) Raman spectrum of $Zr_{0.5}Hf_{0.5}O_2$ powder at ambient conditions outside of the high pressure cell. (ii) Ambient ZrO_2 Raman spectrum measured by Carlone [50]. (iii) Ambient Raman spectrum of $Zr_{0.5}Hf_{0.5}O_2$ as measured by Mojaki [8]. The stars indicate the signature monoclinic Raman bands.

In the spectrum of Mojaki (figure 4.1 (ii)) there is an extra low intensity peak between 250 cm^{-1} and 300 cm^{-1} and a low intensity doublet between 500 cm^{-1} and 550 cm^{-1} wave numbers. These additional peaks could be attributed to laser plasma lines. The $Zr_{0.5}Hf_{0.5}O_2$ sample displays the prominent monoclinic features of Mojaki's [8] sample and those of Carlone [50].

4.2 Hand polished CZ anvils and initial Raman TiO_2 results

The information regarding manual fabrication of CZ anvils can be found in an as yet unpublished paper by our high pressure research group [20]. The manual fabrication technique was important for a number of reasons, namely, learning high pressure methodology and concurrently developing the new manual CZ fabrication technique for use in the MB-GAC. Additionally by conducting Raman measurements while refining the polishing methods, experimental parameters were uncovered regarding the use of PTM, gasketing materials and the optimum flake size and thickness that needs to be loaded (critical in laser heating experiments).

An ambient measurement of $Zr_{0.5}Hf_{0.5}O_2$ when mixed with Si-oil and Fluorinert is shown

in figure 4.2 and reveals a high attenuation of $Zr_{0.5}Hf_{0.5}O_2$ and additional peaks compared to the ambient sample. The inset shows Si-oil and Fluorinert PTM which were compared to the $Zr_{0.5}Hf_{0.5}O_2$ ambient sample. Figure 4.2 shows that there is an intense signal from the Si-oil below 100 cm^{-1} wave numbers and clearly swamps out the lower $Zr_{0.5}Hf_{0.5}O_2$ sample peaks. These peaks are of interest at higher pressure as they are monitored when the orthoII phase develops. By comparing (b), (c) and (d) it is clear the extent to which the Si-oil obscures the $Zr_{0.5}Hf_{0.5}O_2$ Raman signal. By comparing the (a) and (c) it is clear that the Flourinert, (e), intrudes minimally in the $Zr_{0.5}Hf_{0.5}O_2$ spectrum. Even though the Fluorinert displays its own Raman signal, the signal is much less intense than Si-oil, but becomes more intense at higher pressures.

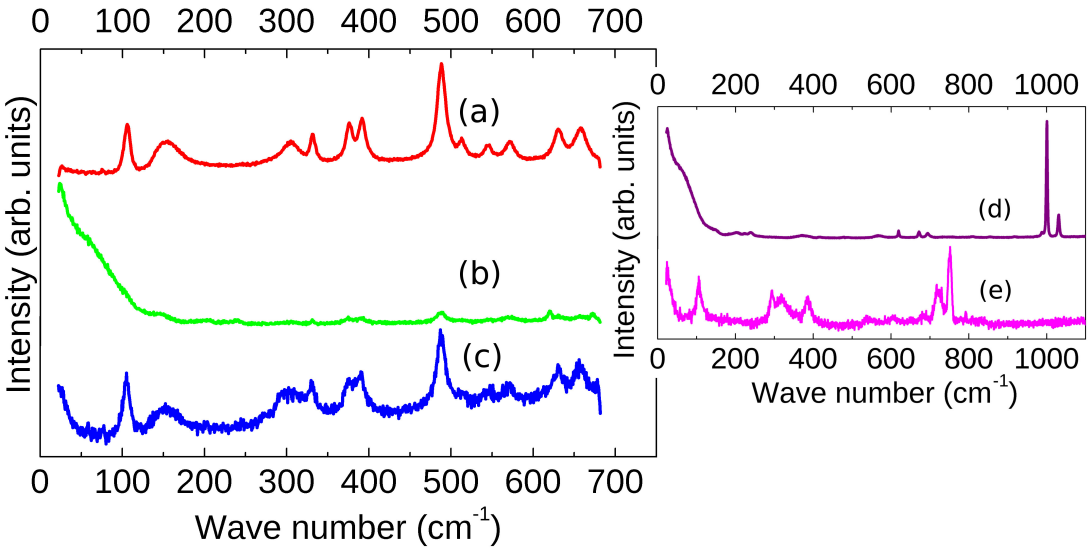

Figure 4.2: Ambient Raman spectra of $Zr_{0.5}Hf_{0.5}O_2$ mixed with PTM - (a) $Zr_{0.5}Hf_{0.5}O_2$ powder (b) $Zr_{0.5}Hf_{0.5}O_2$ mixed with Si-oil on slide, (c) $Zr_{0.5}Hf_{0.5}O_2$ mixed with Fluorinert. The inset shows the Raman bands of the (d) Si-oil and (e) Fluorinert PTM.

Figure 4.3 shows the Raman spectrum of the CZ anvils for the region of interest 0-750 cm^{-1} wave numbers. The Raman spectrum from 0-4000 cm^{-1} was measured by Xu [19] using a 514.5 nm Ar ion laser beam. From the inset in figure 4.3, it can be seen that the CZ anvils display intense Raman bands below 2000 cm^{-1} and more importantly below 1000 cm^{-1}, the region of interest.

In a subsequent experiment where the two samples of TiO_2 and $Zr_{0.5}Hf_{0.5}O_2$ were loaded (with results to follow), evidence is revealed that $Zr_{0.5}Hf_{0.5}O_2$ is a weak scatterer and TiO_2 a

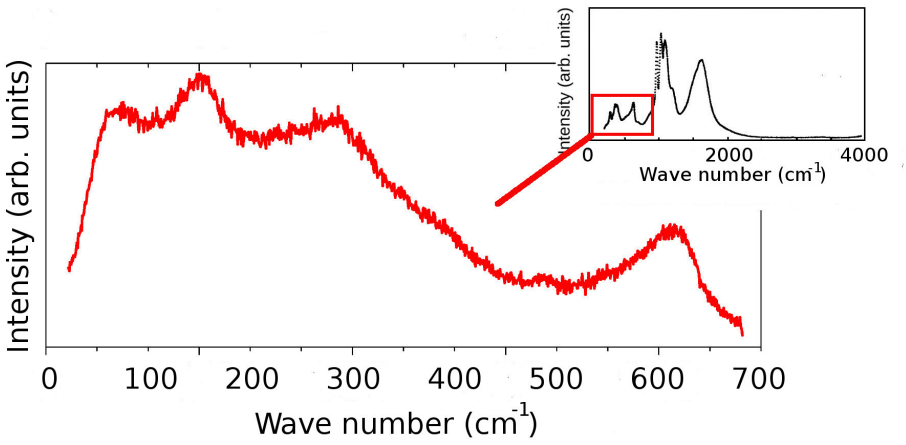

Figure 4.3: Raman spectrum of the CZ anvil - Raman spectrum of CZ anvil over the region of interest from 0-700 cm^{-1} wave numbers. The inset shows the Raman spectrum as measured by Xu [19].

strong scatterer (figure 4.4). The intensities and data acquisition times of the Raman measurements at 5 GPa show the weak scatterer $Zr_{0.5}Hf_{0.5}O_2$, display 2200 counts over 2400 seconds. By contrast the strong scatterer TiO_2 displays 8000 counts over 5 seconds with the signal completely dominating any background signal from the CZ anvil or the PTM.

Some valuable information was learned from these initial experiments. The sample of $Zr_{0.5}Hf_{0.5}O_2$ is a weak scatterer and the TiO_2 sample a strong scatterer. The CZ anvils display Raman bands and attenuate the Raman signal. Experimentally it was found that the PTM should be matched to the type of sample and anvils used. From preliminary analysis of these experiments, TiO_2 and Si oil PTM were loaded into the 200 μm $Ta_{90}W_{10}$ gasket cavity using the MB-DAC (labelled INC718 #1) with 380 μm imperfectly manually polished CZ culets. Raman spectra were taken of the cavity contents and are shown in figure 4.5.

The mode hardening (shift to higher wave number) is clearly distinguished by way of the Eg mode [51] at 140 cm^{-1} of the TiO_2 anatase phase. The other weaker intensity bands are also readily observable at 397 cm^{-1}, 518 cm^{-1} and 641.3 cm^{-1}. This first pressure run resulted in a failure of one of the CZ anvils at 5.56 GPa.

The reason for this failure was believed to be caused by stresses at the edges of the culet face as the anvils were polished with very sharp edges as can be seen in figure 4.6 (a). The polishing technique was then refined to include a rounding on the edges of the culet, to distribute the

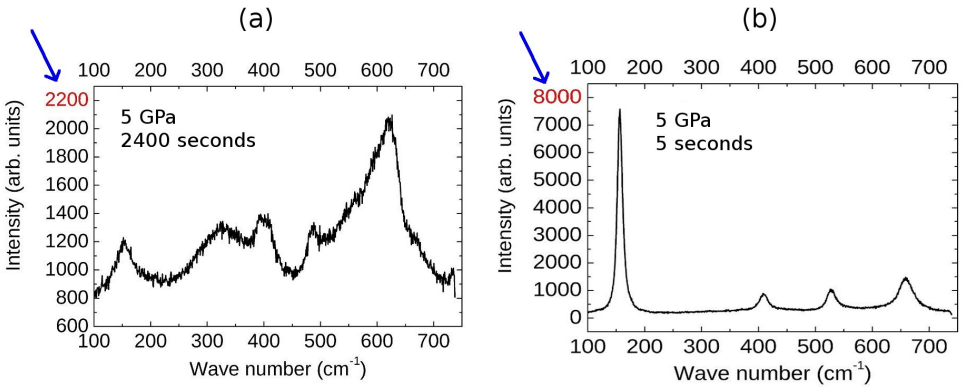

Figure 4.4: Intensity comparison of sample Raman bands - The intensity of (a) Weak scatterer $Zr_{0.5}Hf_{0.5}O_2$ showing 2200 counts over 2400 seconds with contaminating background contributions from the CZ anvils and PTM that obscure some of the signatures of the sample. (b) Strong scatterer TiO_2 reaching 8000 counts over 5 seconds which completely dominates any background signal from the CZ anvil or PTM, at 5 GPa.

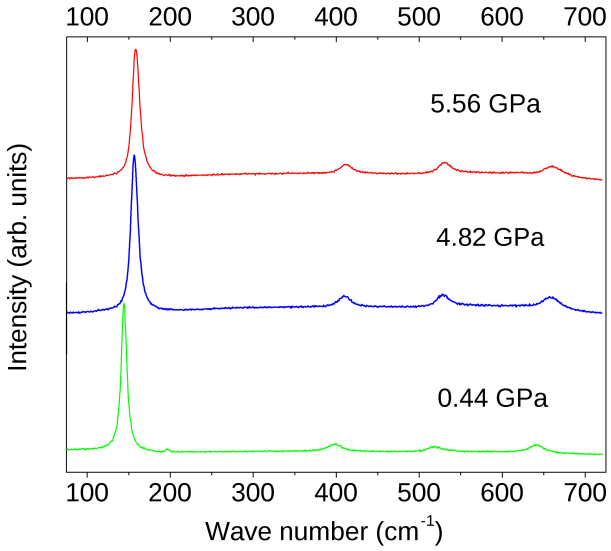

Figure 4.5: Raman MB-GAC high pressure measurement of TiO_2 - Raman spectra of the first TiO_2 pressure experiment to 5.56 GPa using imperfectly hand polished anvils.

stresses at the octagon corners more evenly, as described in the previous chapter. This was noted in figure 4.6 (b).

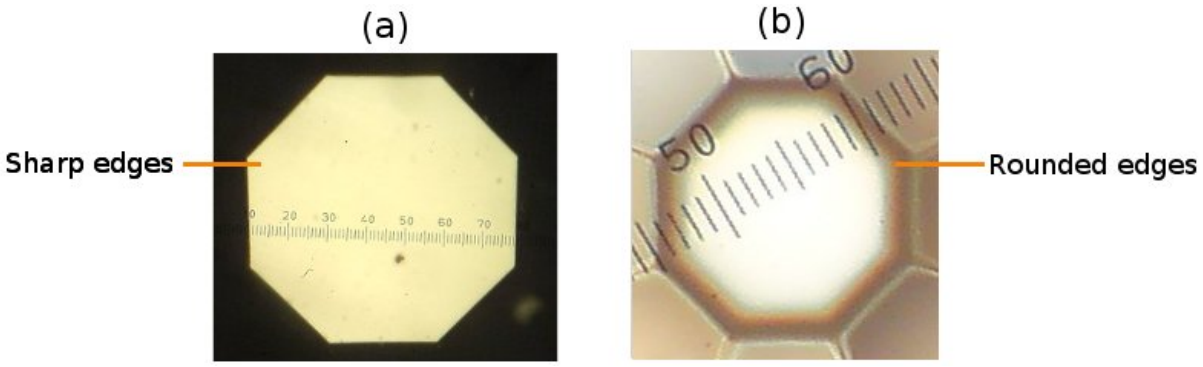

Figure 4.6: Sharp and rounded CZ anvil - (a) Early type sharply polished CZ culet of poor quality. (b) Rounded CZ anvil resulting in high quality culet due to the soft cloth polishing step.

Two anvils of 380 μm were polished with the sole purpose of determining the quality of the anvils by measuring the maximum pressure that could be reached (figure 4.7). The maximum pressure attained in this successful pressure experiment was 13.75 GPa and recorded with the ruby fluorescence method, without taking a Raman spectrum.

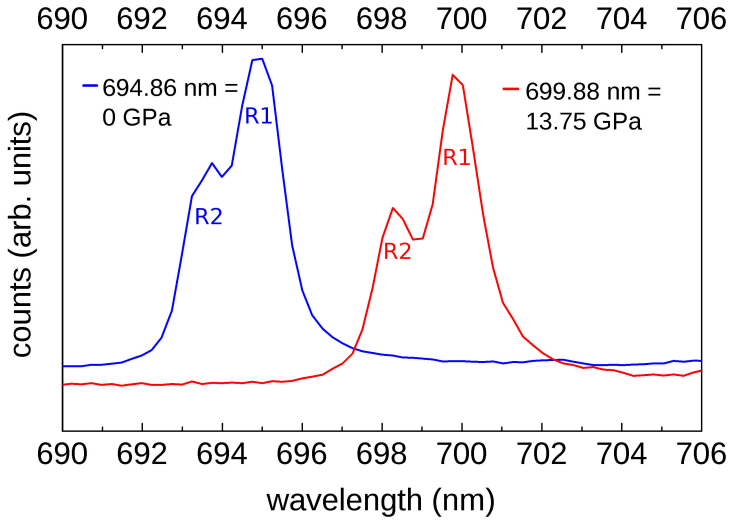

Figure 4.7: Pressure measurement to 13.75 GPa - Rounded CZ anvil test showing ruby fluorescence to 13.75 GPa.

As proof of concept for manual hand polished anvils, a follow up experiment to take data at these pressures was designed. New 380 μm CZ anvils were polished (for MB-GAC, INC718

#3) and TiO_2 and $Zr_{0.5}Hf_{0.5}O_2$ were both loaded into a sample cavity shown in figure 4.8. The initial findings suggested that the Raman signal quality of the $Zr_{0.5}Hf_{0.5}O_2$ sample may be weak at high pressure using CZ anvils. High pressure phase transformations of the TiO_2 could be monitored should the $Zr_{0.5}Hf_{0.5}O_2$ bands be too weak.

4.3 High pressure and high temperature Raman and XRD experiments

This section is divided into four subsections reporting results on MB-GAC experiments using the manually fabricated CZ anvils, preliminary XRD experiments in the MB-DAC and thirdly laser heating experiments with the cryogenically loaded Ar PTM in the MB-DAC. The final subsection compares the laser heated MB-DAC XRD data and Raman spectra to those of the unheated MB-DAC at 20 GPa.

4.3.1 MB-GAC strong scatterer TiO_2 and weak scatterer $Zr_{0.5}Hf_{0.5}O_2$ experiments

In the case exemplified here, thin samples of TiO_2 and the $Zr_{0.5}Hf_{0.5}O_2$ sample were compacted flat to form thin flakes in the indentation and then loaded into the sample cavity. Figure 4.8 shows the loading of the samples, Fluorinert PTM and two ruby balls into the $Ta_{90}W_{10}$ metal gasket cavity which had been spark drilled to 150 μm and closed to 0.7 GPa to create a seal.

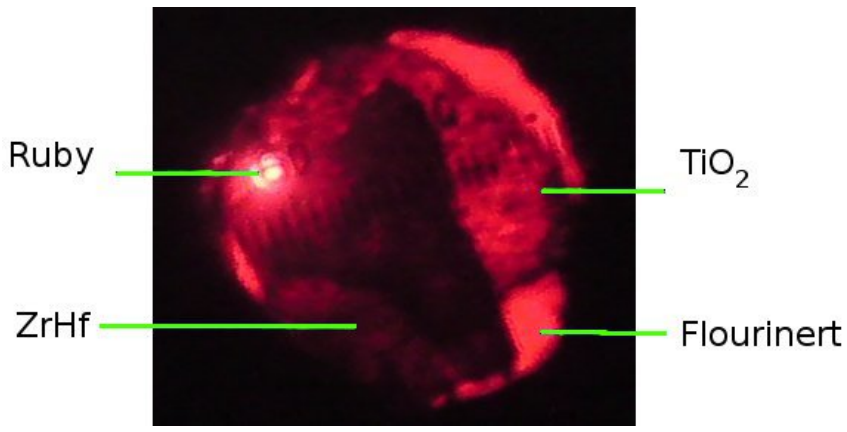

Figure 4.8: MB-GAC loaded with TiO_2 and $Zr_{0.5}Hf_{0.5}O_2$ sample - Non-trivial loading of both samples TiO_2 and $Zr_{0.5}Hf_{0.5}O_2$ into 150 μm diameter sample cavity, fluorinert as the PTM along with ruby balls. The MB-GAC was closed and pressurized to 0.7 GPa to create a seal.

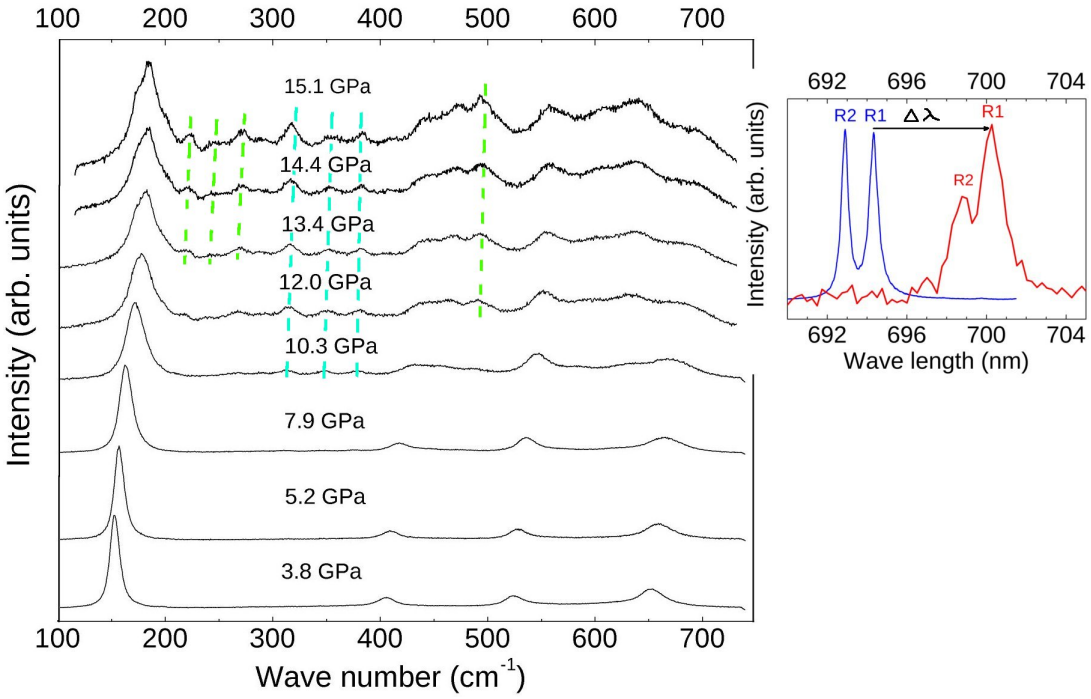

Figure 4.9: Raman MB-GAC TiO_2 high pressure measurements - Raman spectra taken in the MB-GAC from strong scatterer TiO_2. The phase transition to more complex spectra of the α-PbO_2-type phase (blue dashed lines indicate signature peaks) and the baddeleyite phase (green dashed lines indicate signature peaks) are readily distinguished (see text for details). The α-PbO_2-type phase develops between 8 and 10 GPa and the baddeleyite phase develops above 12 GPa. The TiO_2 spectra completely dominates any background signal from the CZ anvil and PTM. The inset shows an example of the ruby fluorescence spectra taken at some of the highest pressures (14.8 GPa) attained in the MB-GAC. Note that the ruby fluorescence peaks are still well resolved and sharp at this pressure. This indicates that the cavity is relatively hydrostatic. Notice that the signal to noise ratio of the ruby fluorescence decreases at higher pressures.

Figure 4.9 shows the TiO_2 high pressure Raman spectra taken in the MB-GAC. As in section 4.2, the mode hardening (shift to higher wave number) is clearly discerned by way of the Eg mode at 140 cm^{-1} of the TiO_2 anatase phase [51]. The other weaker intensity bands are also readily observable at 397 cm^{-1} (B1g), 518 cm^{-1} (A1g / B1g unresolved doublet) and 641.3 cm^{-1} (Eg) [51]. Again, these are part of six assigned Raman active modes (A1g + 2B1g + 3Eg) derived from a factor group analysis of tetragonal anatase [51].

As the pressure was increased to ∼8 GPa, several additional weak peaks appear in the range 330-380 cm^{-1}, characteristic of the α-PbO_2-type phase. As pressure was further increased, the intensities of these new peaks in the range 330-370 cm^{-1} increase and they were clearly distinguished at pressures of ∼10 GPa and beyond, there is a broadening of the intense band at low wave numbers of 180 cm^{-1}. The structural transition of bulk polycrystalline anatase to the α-PbO_2-type intermediate is slow, as found previously [52], coexisting with the original anatase structure up to a pressure of ∼12 GPa. Beyond ∼12 GPa, the intense mode at 180 cm^{-1} broadens appreciably and develops shoulder features. Furthermore as its pressure dependence decreases (signalling hardening), new Raman bands become apparent in the range 225-280 cm^{-1} in addition to a prominent band at 500 cm^{-1}. These are characteristic of the high-pressure (and more incompressible) baddeleyite phase and is fully stabilized at ∼15 GPa, consistent with the literature [48]. It may be noted how all aspects of this phase transition sequence are readily discerned, comparable to the case studies in the MB-DAC. This serves to demonstrate how the pressure signatures and phase transformations of strong to moderate scatterers may be readily monitored with this methodology, even down to low wave number lattice modes in regions where the contaminating background from the anvils is at its most intense. Two subsequent pressures were attained while trying to pressurize to 16 GPa, and the pressures were 15.5 GPa and 15.8 GPa, at which point the top anvil of 380 μm failed.

The spectra of the weak scatter $Zr_{0.5}Hf_{0.5}O_2$ ceramic are depicted in figure 4.10. The Raman spectrum of the monoclinic phase of this compound has been previously studied. The low symmetry of the crystal structure results at the Γ point in 18 Raman-active modes of symmetry (Ag) or (Bg). There are known modes in the wave number range up to ∼250 cm^{-1} [20]. Two main modes are discerned at 100 cm^{-1} and 150 cm^{-1}. These modes have merged by 3 GPa (see later section 4.3.3 for verification in the MB-DAC).

Modes in the range 300-350 cm^{-1} are partially obscured by the CZ background. A medium strength intensity doublet is discerned at 400 cm^{-1}. The known intense mode at 490 cm^{-1} is also discerned above the background. The rest of the modes in the range 500-700 cm^{-1}

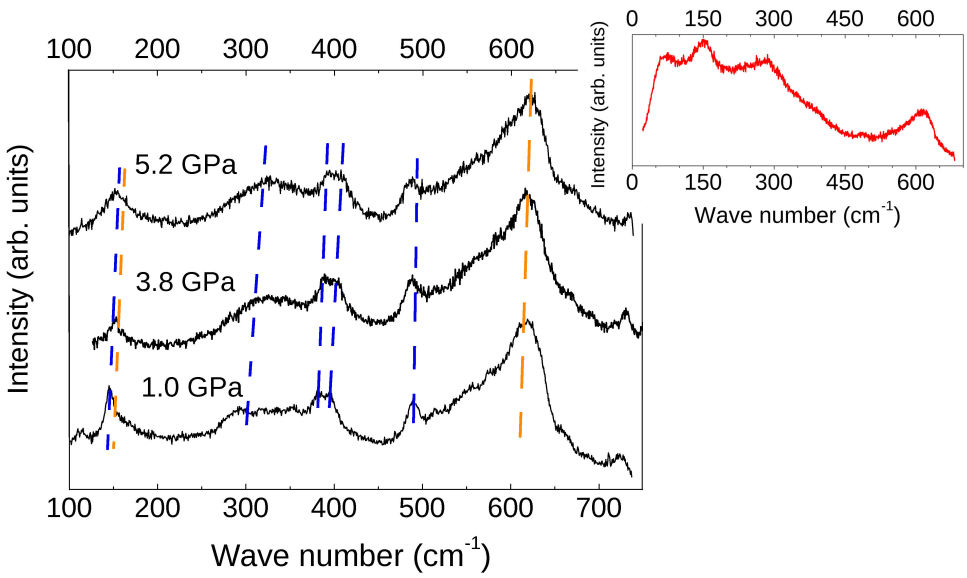

Figure 4.10: Raman MB-GAC $Zr_{0.5}Hf_{0.5}O_2$ high pressure measurements - Raman spectra taken *in situ* in the MB-GAC from the weak scatterer, $Zr_{0.5}Hf_{0.5}O_2$ ceramic. Contaminating background contributions from the CZ anvils (orange dotted line) and PTM obscure some of the signatures of the sample. Raman bands from the $Zr_{0.5}Hf_{0.5}O_2$ sample (blue dotted lines) are also readily discerned. The peaks at 100 cm^{-1} and 150 cm^{-1} merge by 5 GPa as shown in the Raman spectra. Inset shows the Raman spectrum of the CZ anvil.

are obscured by the strong contribution from the CZ. Part of the limitation of this low-scatter sample is perhaps the very thin (10-20 μm thick and near transparent) $Zr_{0.5}Hf_{0.5}O_2$ sample flake used, so that most of the probing radiation is in fact transmitted rather than back-scattered. It is anticipated that the quality of the spectra should improve if there is an increase in the relative sample-to-cavity volumes. The purpose of introducing this data is to confirm, together with the preceding mention of anatase TiO_2 behaviour, that low wave number lattice Raman modes at pressure may be tracked in spite of this being a weak scatterer in the region where the background from the CZ anvil tip is at its most intense. This is the first time that Raman bands at pressure in the lattice mode region have been presented in MB-GAC experiments involving CZ.

These results demonstrate that the CZ-GAC may now be used quite routinely for Raman pressure measurements. It will suffice entirely for the case of strong to moderate scatterers or with Raman spectra very different to that of the anvils (background). It may be possible to give valuable preliminary indicators of the pressure response of weak scatterers (even though there may be background contamination from the CZ anvils) ahead of more suitable DAC experiments. The CZ-GAC is already known to be very suitable for IR spectroscopy work because of the low background in the high wave number regime, perhaps even superior to that of DAC work [53].

This work demonstrates that complementary Raman data in the low wave number regime (lattice mode information) can also be derived from the same pressure cell, to appreciable pressures of 10-15 GPa. This easily covers and even exceeds the pressure range in which the pressure response of bio- and macro- molecular systems are investigated [20]. Smaller CZ culet sizes can be polished to say 300 μm that would allow for an increase in pressure.

These ideas may find similar applicability in moissanite [20] which has higher strength and stability compared to CZ, so that pressures up to 20 GPa for relatively convenient culet sizes (of 380 μm) would be feasible. Although there is need to be aware of where there may be a strong background contribution from Raman signals of the anvil. Emphasis must be placed on the modest cost-effective tooling and polishing techniques that may be used for the appropriate gem-anvil preparation. This methodology could in the least case, be used as an educational tool to school novices in analogous DAC preparation and pressurization techniques, without having to resort to expensive acquisition of diamond-anvils at the outset. Furthermore, materials characterization by optical spectroscopy at extreme high P-T conditions in excess of 10 GPa (previously the exclusive domain of DACs) is now much more accessible with modest effort, expertise and cost.

4.3.2 MB-DAC high pressure with Fluorinert PTM experiments

The experiments on the $Zr_{0.5}Hf_{0.5}O_2$ ceramic in the MB-DAC is presented in this section. XRD will be used to clarify the phase transition at room temperature to 20 GPa complemented by Raman spectroscopy measurements. The results are compared to Raman spectra and XRD data of the end members from literature. In this experiment Fluorinert was used as the PTM, thus no laser heating or furnace heating was done due to probable unpredictable behaviour of fluorinert (and anvil epoxy) at high temperatures. This initial investigation was performed to determine what further experiments would be necessary to further explore the phase diagram of $Zr_{0.5}Hf_{0.5}O_2$.

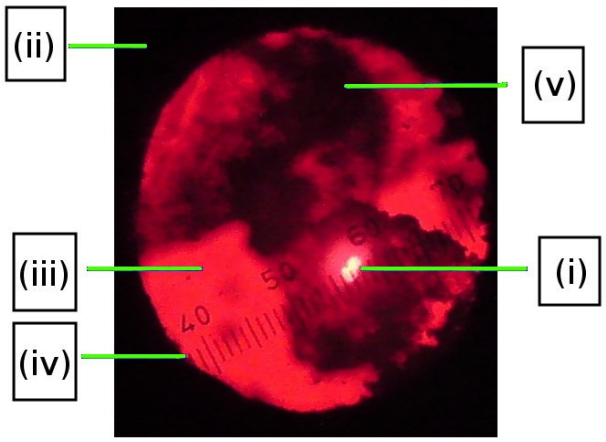

Figure 4.11: MB-DAC cavity loaded with $Zr_{0.5}Hf_{0.5}O_2$ and Fluorinert PTM. - (i) Ruby balls fluorescing using the 20 mW, 532 nm green laser excitation source, (ii) SS301 gasket, (iii) Flourinert PTM, (iv) 200 μm diameter sample cavity, (v) $Zr_{0.5}Hf_{0.5}O_2$ sample flakes.

The MB-DAC of tungsten 302, (HV = 560) was used and a gasket of SS301 (HV = 350) preindented to 40 μm, was spark drilled to obtain a sample cavity of 200 μm diameter. Samples of $Zr_{0.5}Hf_{0.5}O_2$ were compacted flat to form thin flakes in the indentation and then pushed into the sample cavity with Fluorinert PTM, with filling factor of ~60% (figure 4.11). Figure 4.12 shows the ambient XRD measurement mentioned in section 4.1 above using the Bruker D8 x-ray diffractometer with Cu-K_α radiation.

Figure 4.13 shows XRD data of $Zr_{0.5}Hf_{0.5}O_2$ sample loaded in the MB-DAC. The first XRD measurement is at 0.6 GPa (sealing pressure) and clearly shows the monoclinic phase (two signature peaks at 12.5° and 14°, measured in 2θ) by comparing it to the diffraction pattern of the ambient powder sample in figure 4.12 (Mo-K_α radiation). These signature monoclinic

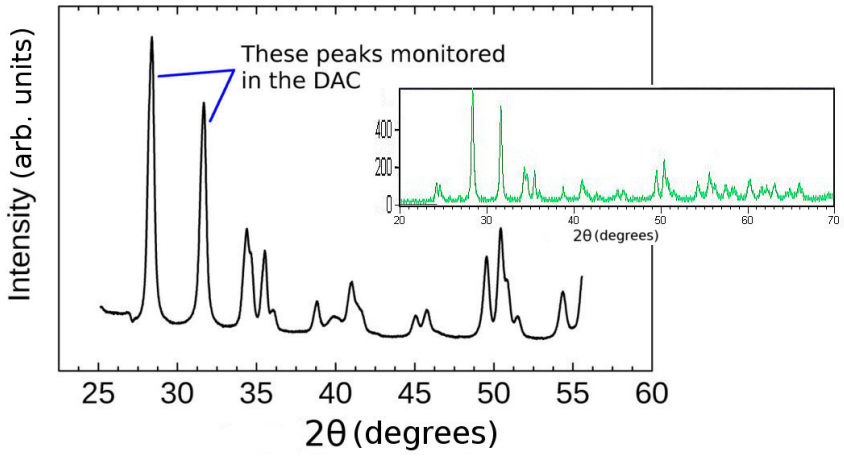

Figure 4.12: XRD of raw $Zr_{0.5}Hf_{0.5}O_2$ powder - Ambient $Zr_{0.5}Hf_{0.5}O_2$ measurement on powder sample with 3 wt% Pt Black mixed in for internal pressure marker (∼40°) experiment using copper K_α (Cu-K_α) whereas the MB-DAC XRD measurements used molybdenum-K_α (Mo-K_α). The inset shows the ambient XRD measurement performed by Mojaki [8].

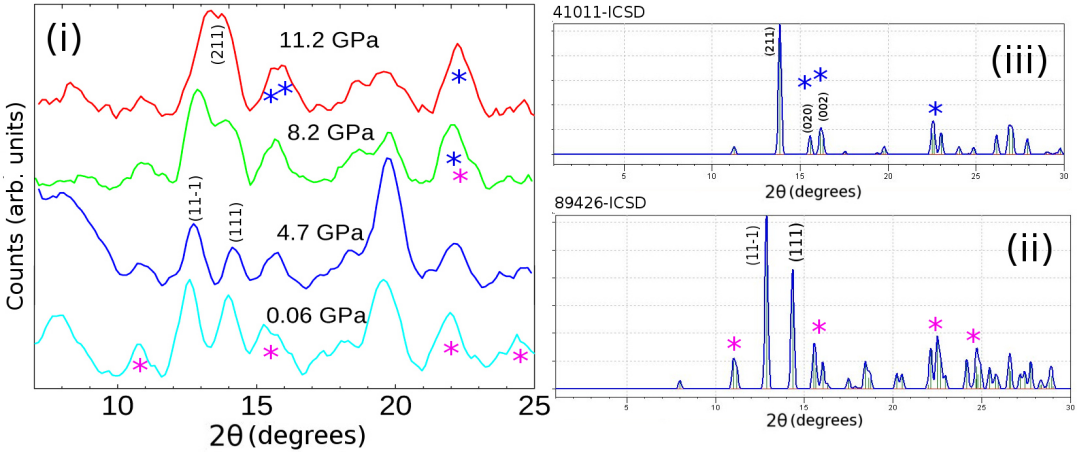

Figure 4.13: XRD of $Zr_{0.5}Hf_{0.5}O_2$ in the MB-DAC - (i) XRD MB-DAC at high pressure displaying two peaks at 12.5° (11-1) and 14° (111) indicating monoclinic $Zr_{0.5}Hf_{0.5}O_2$. At 8.3 GPa the orthoI peak 13.5° (211) starts emerging. Insets (ii) show end member ZrO_2 monoclinic and (iii) orthoI high pressure phase (98426-ICSD and 41011-ICSD respectively). The pink stars correspond to monoclinic sample peaks and the blue stars correspond to orthoI sample peaks.

sample peaks at 12.5° and 14° are labelled the (11-1) and (111) reflections, respectively taken from the corresponding labelled peaks of the end members [1, 4]. The XRD pattern in figure 4.13 shows that the monoclinic phase dominates to 8.2 GPa although the monoclinic to orthoI phase change is initiated at ∼5 GPa [4]. The peaks at 12.5° and 14° decrease in intensity as the phase change proceeds to orthoI with a single peak at 13° developing. This is seen by tracking it from 0 GPa through to 20 GPa and confirmed by the literature [1, 4]. There are additional signature peaks at 16° and 22° indicated by pink and blue stars for the monoclinic and the orthoI phase, respectively.

At 4.7 GPa the signature monoclinic peaks are still present from the 0.6 GPa XRD data. There is no indication of the orthoI phase. This confirms that the monoclinic to orthoI phase boundary is above 4.7 GPa and therefore certainly in the ∼5 GPa region as stated for the end member phase boundaries. The monoclinic peaks are slightly shifted right under the application of pressure. The other sample peaks are of low intensity and suffer from being broad and thus some of the doublets are obscured. The MB-DAC was slightly misaligned in the sample holder resulting in a strong gasket peak at 20°.

From 8.2 to 11.2 GPa, there is a phase mixture as the two monoclinic peaks decrease in intensity. The peaks shift slightly to the right under pressure as expected. There is the appearance of a third peak between the two monoclinic peaks and this indicates the orthoI phase developing at 13.5°. The highest intensity orthoI peaks are at 13.5° (labelled the (211) reflection) and 16° (the combination of the (020), (002) and (400) reflections, respectively). The appearance of these peaks confirm the phase diagram boundary for ZrO_2 and HfO_2 end members in the literature (shown in figure 2.2 and 2.3) [1, 4]. Ohtaka *et al.* [4] observed that low pressure measurements of ZrO_2 had slow phase transformations and that there was a mixture of the phases over a wide range of pressures. The monoclinic phase coexists with the orthoI phase up to a pressure of ∼15 GPa. This sluggishness may be overcome by heating at temperatures above 600°C [1].

Figure 4.14 compares the two 11 GPa measurements taken a few weeks apart and show that the orthoI phase had further developed over time (the kinetics is on a time scale of days).

The orthoI phase is dominant in the 18.2 GPa and 20 GPa XRD patterns by comparing figure 4.15 to figure 4.13 (iii). There is no indication of orthoII from the XRD because of the absence of any signature orthoII peaks at 15° or 15.5°.

The sluggishness of the transition from monoclinic to orthoI was confirmed in the Raman spectra. As pressure increases further to 15 GPa the intensities of these new peaks (150 cm^{-1}, 200 cm^{-1} and 400 cm^{-1}) increase beyond 15 GPa there is an intense mode at 400 cm^{-1}. These

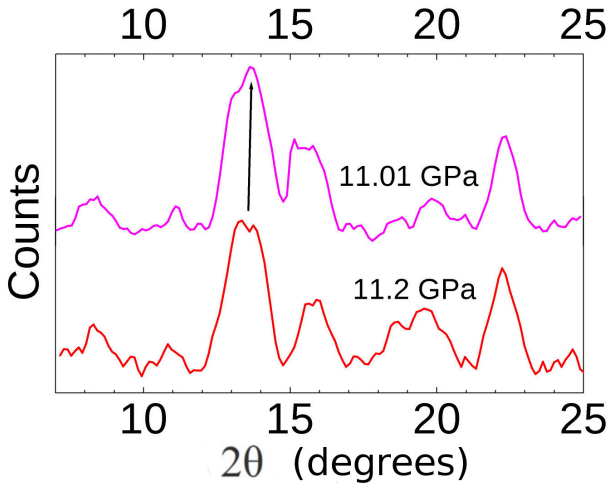

Figure 4.14: 11 GPa XRD data of $Zr_{0.5}Hf_{0.5}O_2$ - XRD high pressure data indicating the sluggish monoclinic to orthoI conversion of $Zr_{0.5}Hf_{0.5}O_2$. The second 11.01 GPa XRD pattern was taken a few weeks later. The cell had relaxed to a lower pressure of 11.01 GPa form 11.2 GPa. The conversion to the orthoI phase from monoclinic has advanced.

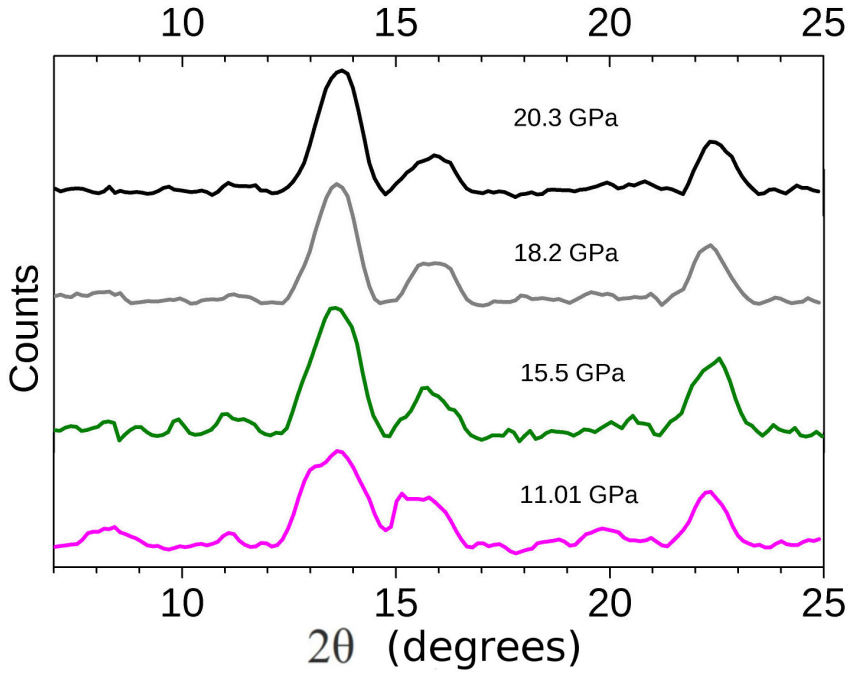

Figure 4.15: XRD high pressure orthoI phase of $Zr_{0.5}Hf_{0.5}O_2$ - XRD MB-DAC high pressure diffraction pattern displaying the two monoclinic peaks at 13° and 14° weakening in intensity and the orthoI peak dominating the XRD pattern. XRD taken from a very well aligned MB-DAC as there is hardly a trace of the gasket line at 20°.

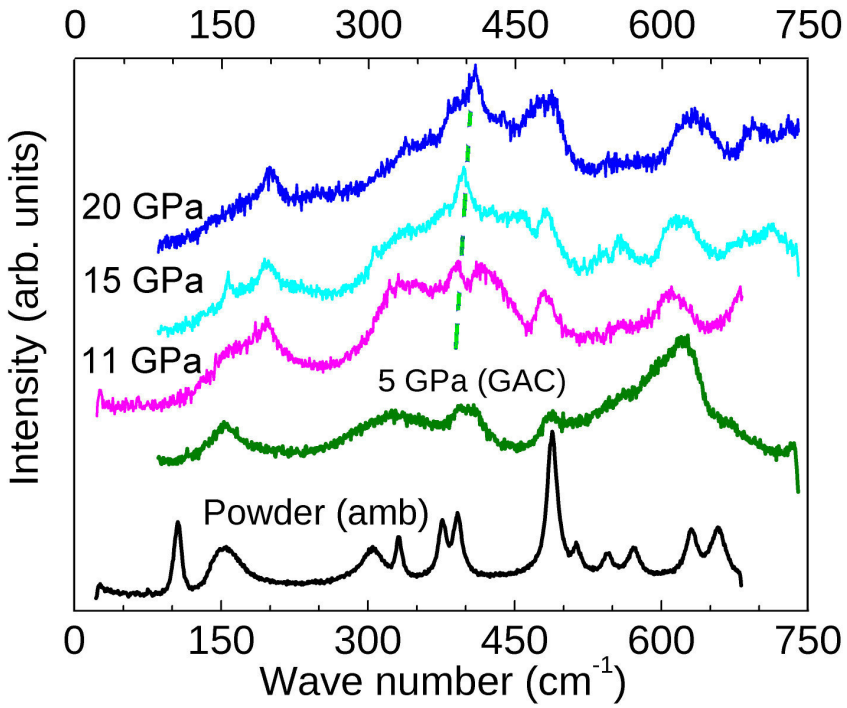

Figure 4.16: Raman MB-DAC high pressure of $Zr_{0.5}Hf_{0.5}O_2$ - Raman spectrum of $Zr_{0.5}Hf_{0.5}O_2$ powder at ambient P-T, MB-GAC at 5 GPa and the MB-DAC at 11 GPa, 15 GPa and 20 GPa. The orthoI signature peak is at 380 cm^{-1} and is discerned in the 11 GPa spectra (green dotted line). $Zr_{0.5}Hf_{0.5}O_2$ in MB-DAC loaded with Fluorinert PTM with no laser heating performed.

are supposed to be characteristic of the high-pressure (and more incompressible) orthoI phase. This orthoI phase is not fully stabilized at ∼15 GPa consistent with the literature [1, 4]. The pressure evolution of the Raman spectra of $Zr_{0.5}Hf_{0.5}O_2$ is shown in figure 4.16. Under ambient conditions the prominent Raman bands are from 100 cm^{-1} through to 700 cm^{-1}. The ambient powder spectrum and CZ anvil cell data (5 GPa) is used as a reference, and it is slightly attenuated compared to the MB-DAC spectra. In this experiment, the first MB-DAC Raman measurement was taken at 11 GPa. It displays a broad peak at 150 cm^{-1}, peaks between 300 cm^{-1} and 450 $cm^{-1}$and between 500 cm^{-1} and 600 cm^{-1}. When the pressure is increased to 15 GPa a number of new Raman bands of low intensity appear at wave numbers 150 cm^{-1} and 200 cm^{-1}. These appear to merge to a single peak at 200 cm^{-1} at 20 GPa and are specific to the high pressure orthoI phase. The bands at high pressure are broader than the low pressure monoclinic phase. The Raman spectra at 20 GPa can thus be used as a reference for the Raman signatures of orthoI. Using XRD it may be noted how all aspects of this phase transition sequence are readily discerned through the qualitative tracking of peaks. This is the first time that the Raman spectrum of the $Zr_{0.5}Hf_{0.5}O_2$ solid solution has been unambiguously identified as orthoI.

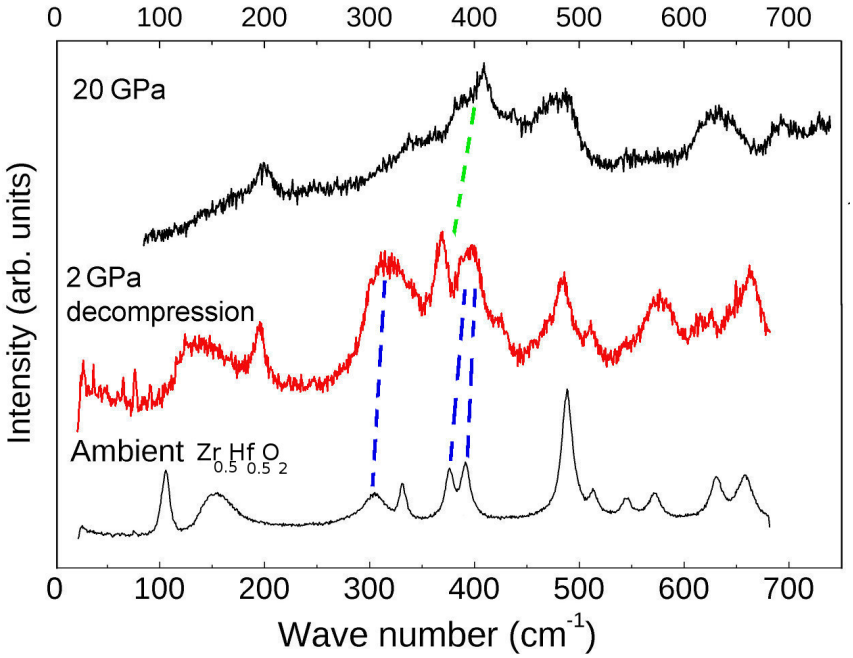

Figure 4.17: Raman MB-DAC decompression from 20 GPa to 2 GPa of $Zr_{0.5}Hf_{0.5}O_2$ - Figure showing spectra at 20 GPa and 2 GPa. Blue dotted lines indicate monoclinic signature peaks and the green dotted line the orthoI signature peak.

In ZrO_2 both orthoI and orthoII high pressure phases are quenchable to ambient conditions [4]. HfO_2 orthoI is not quenchable to near ambient conditions but the orthoII phase is [1]. Figure 4.17 shows the Raman spectra of the sample after it has been decompressed to 2 GPa. The pressure was decreased slowly from 20 GPa to 2 GPa and then immersed in a bath of liquid nitrogen to attempt to quench in the orthoI phase. The comparison of the Raman spectra in figure 4.17 to the XRD data in figure 4.18 shows that there is a mixture of phases. Monoclinic modes as well as orthoI modes are discernible and the 2 GPa spectrum looks similar to the Raman spectra taken at 11 GPa. The XRD patterns confirm the monoclinic and orthoI mixture. The XRD data shows the two monoclinic peaks at 13° and 14° reappear with the orthoI peak observed between the two peaks at 12.5°. This shows that there is some reversion to the original monoclinic phase. It is highly probable that the recovered mixture of the phases monoclinic and orthoI has enhanced hardness and toughness properties compared to the original monoclinic phase. This result is inferred as Block *et al.* discovered enhanced hardness and toughness for the end member ZrO_2 for pressures and temperatures as low as 8.6 GPa and 500°C [54].

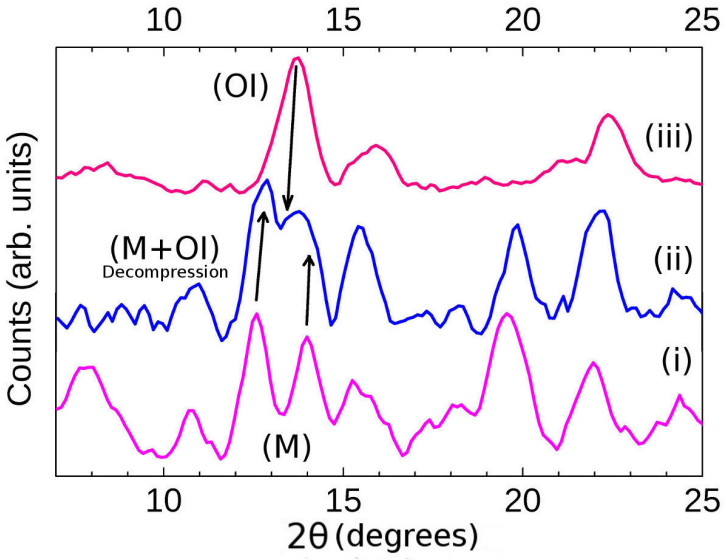

Figure 4.18: XRD MB-DAC decompression from 20 GPa to 2 GPa of $Zr_{0.5}Hf_{0.5}O_2$ - XRD data at (i) 0.6 GPa (close to ambient) displaying monoclinic structure, (ii) 2 GPa decompression data which is a mixture of monoclinic (higher percentage) and the orthoI phases. (iii) 20 GPa showing the full conversion to orthoI.

This experiment confirms that the $Zr_{0.5}Hf_{0.5}O_2$ solid solution cannot be quenched to the orthoI phase exclusively from 20 GPa whereas ZrO_2 can be. This is the first time that $Zr_{0.5}Hf_{0.5}O_2$

has been quenched to ambient from the orthoI phase. By using the combination of Raman and XRD we are able to track phase changes of $Zr_{0.5}Hf_{0.5}O_2$. The emphasis of this first experiment was to learn high pressure methodology in the MB-DAC. Secondly the set up of the XRD was completed and diffraction measurements taken. A reference diffraction pattern involving no heating was required for comparison with the high pressure laser heated sample. The XRD data shows conclusively that the orthoI phase is dominant and there is compelling evidence that the orthoII phase cannot be synthesized by pressure (up to 20 GPa) at room temperature alone. This is the first time that XRD at pressure on $Zr_{0.5}Hf_{0.5}O_2$ have been presented in MB-DAC experiments and compared with Raman spectra. The following experiment explores the conversion of $Zr_{0.5}Hf_{0.5}O_2$ to the orthoII high pressure phase (cotunnite) when CO_2 laser heating is used to accelerate phase transition kinetics.

4.3.3 MB-DAC high pressure-temperature with Ar PTM experiments

In this section the pressure-temperature phase diagram of $Zr_{0.5}Hf_{0.5}O_2$ is further explored to 20 GPa and laser heating to ∼1000°C. The Raman spectra results are compared to the previous pressure experiment and Mojaki's [8] data along with the phase diagrams of the end member components (ZrO_2 and HfO_2).

The MB-DAC (labelled INC718 cell # 1) was prepared with a gasket of SS301 preindented to 40 μm and spark drilled to obtain a cavity of 200 μm diameter. Thin sample flakes of $Zr_{0.5}Hf_{0.5}O_2$ were pushed into the sample cavity (figure 4.19). Liquid Ar was cryogenically loaded into the cavity to insulate the sample from the diamonds during the CO_2 laser heating experiment.

Raman spectra (figure 4.20) were taken on the darker regions due to a better signal to noise ratio. These are labelled (A) through (E) in figure 4.19. The pressure evolution of the $Zr_{0.5}Hf_{0.5}O_2$ sample is comparable to previous high pressure experiments from 2 GPa to 15.4 GPa (the MB-GAC experiment shown in figure 4.10 and the MB-DAC experiment shown in figure 4.16).

At 15.4 GPa, a laser heating experiment was attempted. The cavity was heated for approximately 15 minutes at about 75% full power with the laser beam focused into the second diamond as described in subsection 3.3.1. Figure 4.21 shows the pre- and post- laser heating Raman measurements at 15.4 GPa. It is clear that there is no change in the spectra. This implies that the laser was not intense enough, not focused properly on the sample or the heating was for too short a time. The only change that was noticed was the increase in pressure of ∼0.4 GPa to 15.8 GPa after the laser heating.

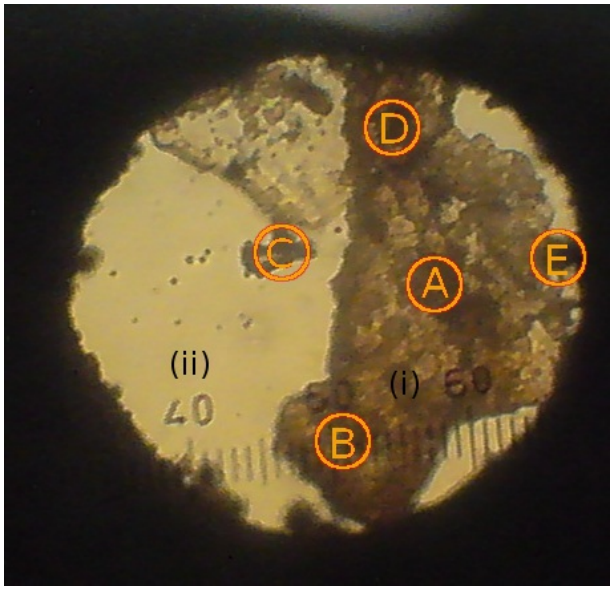

Figure 4.19: MB-DAC cavity loaded with $Zr_{0.5}Hf_{0.5}O_2$ and Ar PTM - 200 μm diameter stainless steel gasket cavity. (A), (B), (C), (D) and (E) are the regions that were measured by Raman spectroscopy. (i) Ruby balls and (ii) liquid Ar PTM.

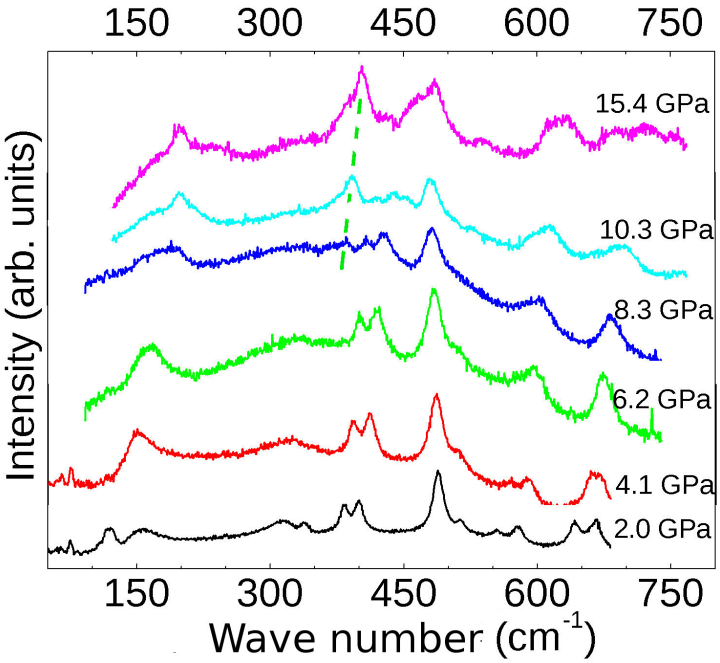

Figure 4.20: Raman $Zr_{0.5}Hf_{0.5}O_2$ and Ar PTM - Raman specrta of $Zr_{0.5}Hf_{0.5}O_2$ and liquid Ar PTM before laser heating. Green dotted line shows the orthoI signature peak.

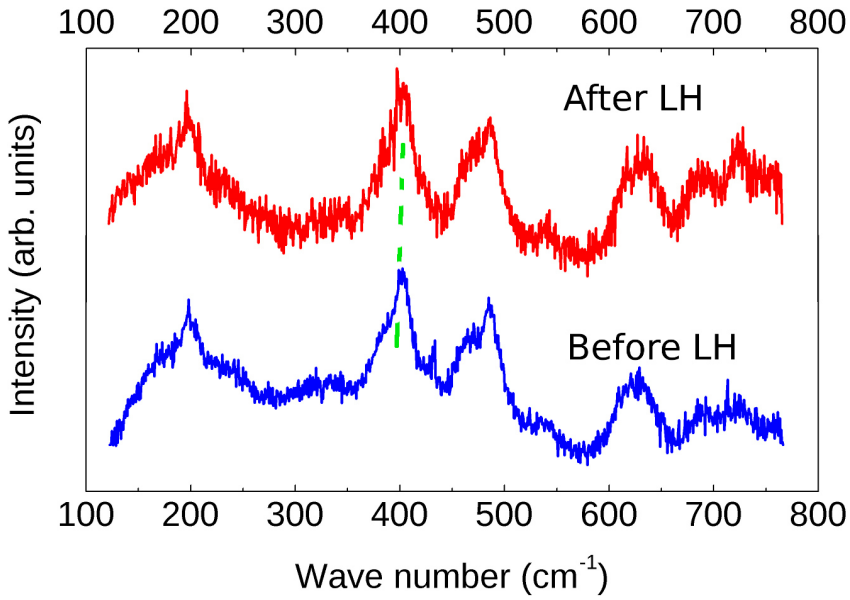

Figure 4.21: Raman spectra at 15 GPa of $Zr_{0.5}Hf_{0.5}O_2$ - Raman spectra at 15 GPa before and after 15 minutes of laser heating (LH). No discernible change in the spectra is observed. The green dotted line indicates the signature orthoI peak.

The signature peaks are marked from (a) through (u) on figures 4.22 and 4.23 for easy comparison. The XRD data was converted to d-spacing (figure 4.23) so that it could be directly compared with the d-spacings found in the literature [1, 4]. The d-spacing is as defined in equation 2.18.

The 2 GPa and 8.3 GPa XRD data shows consistency with the previous MB-DAC data shown in figure 4.13. The two monoclinic peaks are clearly discernible in the 2 GPa XRD pattern. The features of the monoclinic and orthoI are easily observed in figure 4.22. Monoclinic peaks at 12.5° and 14° are labelled by the (11-1) and (111) reflections in figure 4.23. These reflections convert to the orthoI peak at 13.5° (the (211) reflection) and seen in the 8.3 GPa XRD pattern. In a similar way to the previous result (figure 4.13) the two peaks at 12.5° and 14° dominate up to about 8 GPa after which the single orthoI peak appears. Two lower intensity monoclinic peaks at 15.5° (the combination (002) and (020) reflections) become one orthoI feature at 16° (the (020) reflection). In the reference XRD patterns (figure 4.13 (iii)) there are two peaks at 22° and is labelled (n).

The (*hkl*) values have been assigned from the literature as (b) (11-1) and (c) (111). Peak (d) is the combination of the (020), (002) and (400) peaks. The Ar peaks are not yet prominent

because the Ar has possibly only randomly crystallised. The gasket line is at peak (f).

The next data point is 8.3 GPa and is a mixture of monoclinic and orthoI. The monoclinic peaks are observed at (i) and (j) (the (11-1) and (111) reflections, respectively, with the orthoI peak developing between them. The intensities are low due to the cell being skew in the holder and the gasket line the dominant feature at (m). The peaks (k) and (l) are thought to be the solidified Ar (solidifies at 1.2 GPa [26]) obscuring the signature orthoI reflections at (020), (002) and (400) labelled for ZrO_2 and HfO_2 in the literature [1, 4].

As no phase transformation took place as the pressure was increased to 20 GPa after which the final laser heating experiment was performed. The laser was raster scanned over the sample over the course of an hour. In contrast to the previous laser heating attempt, the raster scan lasted longer, the laser power was increased and was focused to a smaller spot size.

The laser heated 20 GPa XRD data (in figure 4.22) shows the orthoI peak at (o) with two less intense shoulder features at (p) and (u) shown in figure 4.22 (2θ) and figure 4.23 in d-spacing. The peaks in figure 4.22 at 16°, 14° and 19° represent reflections (102), (111) and (211) respectively. The (p) and (u) peaks are at a d-spacing of 2.80 Å and 2.65 Å. These peaks correspond to the (102) and (111) reflections, respectively, of the orthoII phase of the end members, as depicted in figure 4.23. Peak (s) is also a feature of the orthoII phase and is at a d-spacing of 2.02 Å corresponding to a reflection of (211). This (211) reflection is the most intense feature of the end member ZrO_2 orthoII phase. There are orthoI features still present in the 20 GPa XRD laser heated data. The feature (o) is the (211) signature reflection that is seen to be emerging between peaks (i) and (j) in the 8.3 GPa data. Peak (a) and (h) are features of the monoclinic and orthoI phases, respectively (reflection not labelled) and is absent from the 20 GPa laser heated data. The orthoII (011) reflection is overlapped by the orthoI (211) reflection (o). The transition to orthoII accelerates with the application of heat in the ZrO_2 case. The Ar peaks are represented as blue arrow heads in both the figures 4.22 and 4.23 and labelled (q) and (r) [55] and mask any orthoII peaks in that region. The peak at (t) (along with (f) and (m)) is the gasket line. The d-spacings are given in table 4.1.

The 20 GPa XRD laser heated data consists of a mixture of orthoI and orthoII. The d-spacings and angles of the orthoI and the orthoI/orthoII mixture are reflected in tables 4.2 and 4.3.

The experimental data is shifted to the left of the literature values. The internal XRD calibrant was difficult to track in initial tests and was not used in the XRD experiments. Systematic errors include the sample to detector distance, a conservative error is about 0.5 mm by adjusting

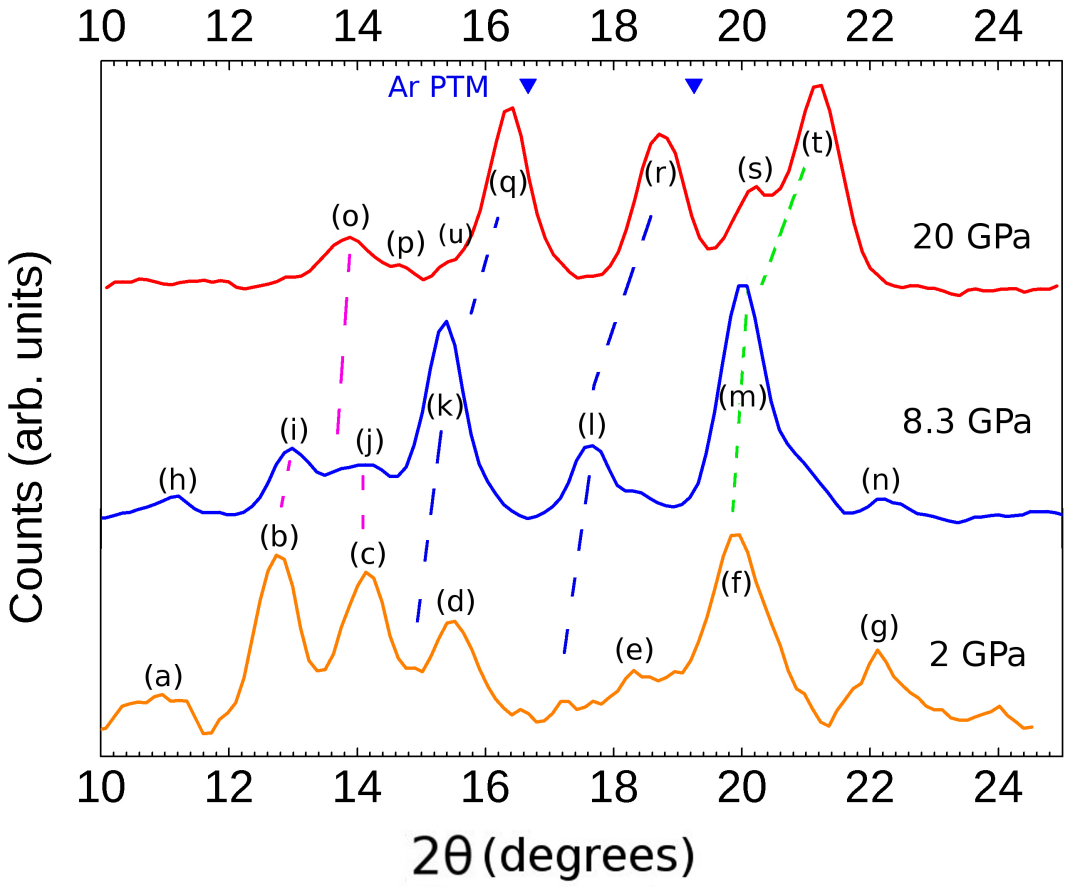

Figure 4.22: XRD data of $Zr_{0.5}Hf_{0.5}O_2$ with Ar PTM - 2 GPa, 8.3 GPa and 20 GPa XRD. Monoclinic to a mixture of orthoI and orthoII (see text for peak assignments). d-spacing of the Ar peaks are represented as blue arrow heads (from literature values) with the blue dotted lines showing the Ar as measured in the sample. The gasket line is indicated with the green dotted line.

Table 4.1: Ar d-spacings at 2 GPa, 8.3 GPa and 20 GPa - For the (111) and (200) reflections

Pressure (GPa)	(111)(Å)	(200)(Å)
2	2.83	2.45
8.3	2.62	2.27
20	2.46	2.13

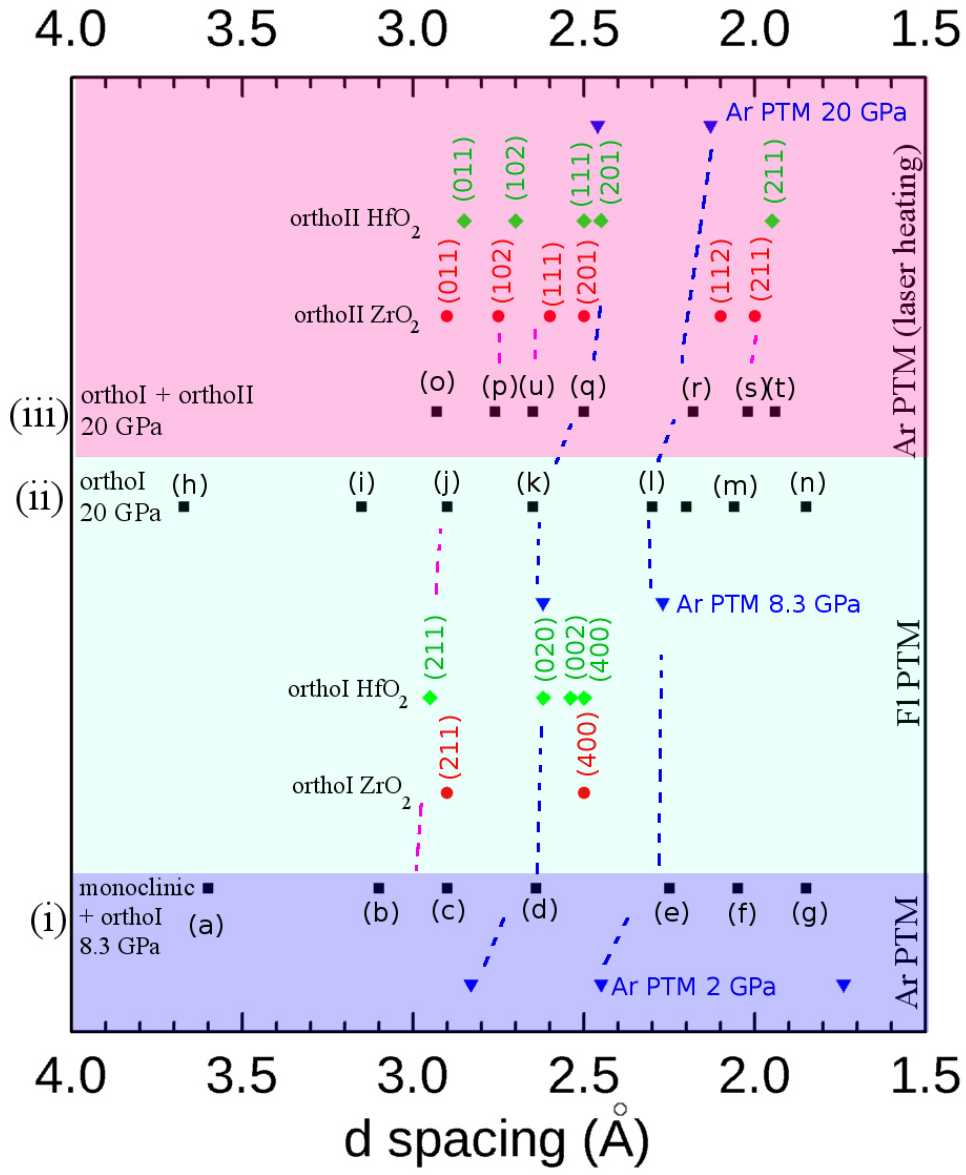

Figure 4.23: d-spacing obtained from XRD data of $Zr_{0.5}Hf_{0.5}O_2$ - 8.3 GPa (Ar PTM), 20 GPa (Fl PTM) and 20 GPa (Ar PTM) XRD d-spacing plotted alongside d-spacing of the end members from literature. (i) Monoclinic orthoI mixture at 8.3 GPa. (ii) OrthoI phase at 20 GPa. (iii) OrthoI orthoII mixture. Details follow in text.

Table 4.2: 20 GPa d-spacing of fully converted high P orthoI phase - Fully converted high P orthoI phase of $Zr_{0.5}Hf_{0.5}O_2$ at 20 GPa (Fluorinert PTM).

(hkl)	Angle (°)	d-spacing (Å)
	8.29	4.91
	11.5	3.54
11-1	13.07	3.12
111	14.65	2.78
	16.16	2.52
	20.31	2.01

Table 4.3: 20 GPa d-spacing of high P orthoI and orthoII phase mixture after laser heating - Mixture of the high P orthoI and orthoII phase of $Zr_{0.5}Hf_{0.5}O_2$ at 20 GPa (Ar PTM and laser heating).

(hkl)	Angle (°)	d-spacing (Å)
011	13.87	2.93
102	16.29	2.50
111	18.7	2.18
112	20.27	2.02
211	21.05	1.94

the telescope in and out of focus, the error is ∼0.05 Å in the reflections calculated using FIT2D which is a about 0.5° respective error in the angle. There is also an error associated with the beam centre position. The DAC needs to be removed from the XRD stage for pressure increases and heating. The monocapillary needs to be moved and therefore the beam centre is different for each measurement. The monocapillary optics also add a 10% error to peak widths [41]. Due to uniaxial pressure generation the pressed flake and Ar PTM has a high potential for non-random crystallite orientation. This affects the intensities of the diffraction peaks and in some cases may suppress peaks quite significantly. There is also an error associated with pressure measurement using the ruby fluorescence method. Pressures can be accurately measured to 0.02-0.05 GPa due to differential thermal expansion of the components of the DAC and to time dependent mechanical relaxation within the gasket [24].

It is important to note that the one of the goals of the experiment was to realize (or initiate) the orthoII (cotunnite) phase at a low as possible pressure, even though the MB-DAC was stable and could have been pressurized to higher pressures.

4.3.4 Comparison of the 20 GPa high pressure experiments as a function of temperature

The following subsection compares the 20 GPa results from both the MB-DAC loaded with Fluorinert to the MB-DAC loaded with liquid Ar and laser heated to ∼1000°C. The XRD data and Raman spectra are directly compared to Mojaki's [8] spectra and to the literature [50]. The results lead to a formulation of what future experiments should be performed including experiments using synchrotron radiation.

Experimental Raman spectra from this study (shown in figure 4.24 (i) laser heated, and (ii) pressure only, at 20 GPa) are shown alongside literature values for (iii) HfO_2 and (iv) ZrO_2 [56]. Figures (i) and (ii) have no major discrepancies, the Raman bands at 200 cm^{-1} and 550 cm^{-1} are more intense in (ii) than in (i). Figure 4.24 (v) shows previous Raman data obtained by Mojaki, with her spectra displaying similar bands at 400 cm^{-1} and 500 cm^{-1}. The three low intensity bands above 600 cm^{-1} are also present in all data, although slightly shifted. The band found at 200 cm^{-1} in figures 4.24 (i), (ii), (iii) and (iv) is missing from the laser heated spectra in 4.24 (v). Spectra in (v) have a high signal to noise ratio which could account for the peak not being easily distinguished at 100-200 cm^{-1}. Note that the signature orthoI Raman band is at 400 cm^{-1} and is absent from the orthoII Raman spectra of the end members in (iii) and (iv) and the laser heated Raman spectrum of Mojaki (red in (v)) which is indicated by the green

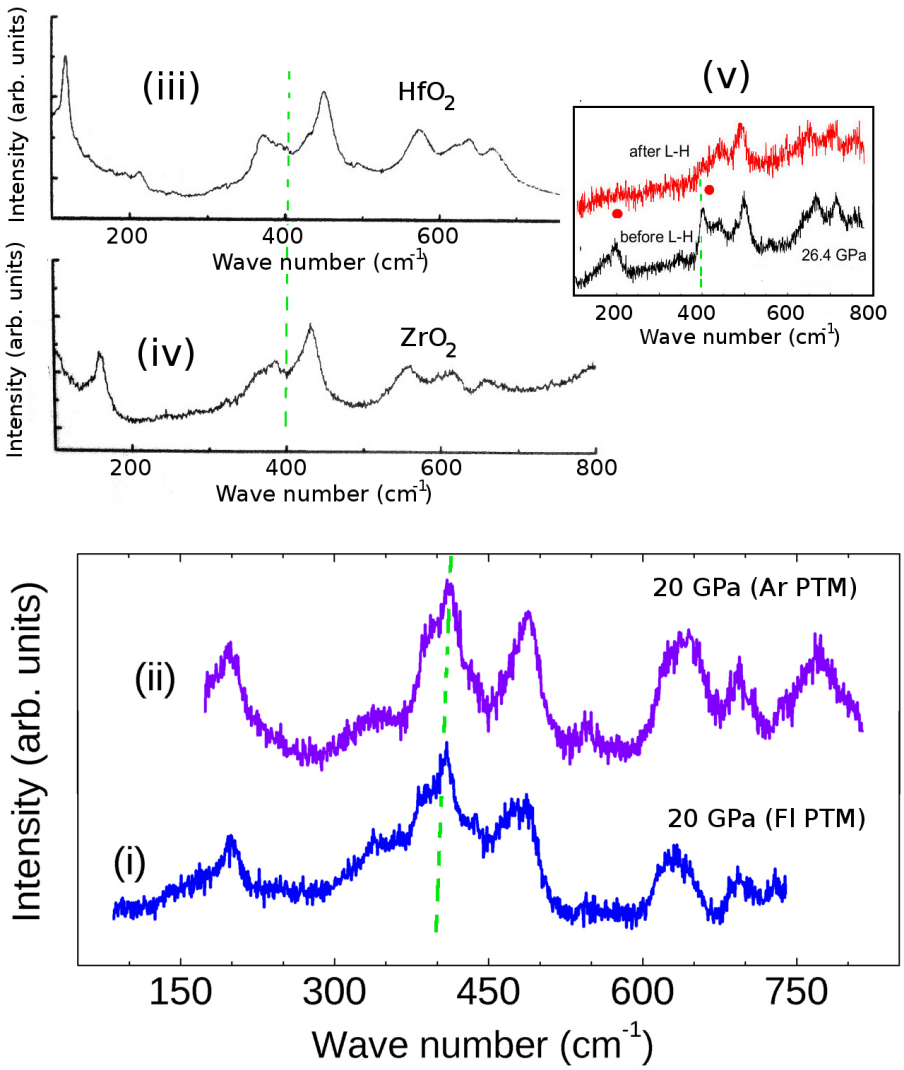

Figure 4.24: OrthoII Raman comparison at 20 GPa of $Zr_{0.5}Hf_{0.5}O_2$ - (i) 20 GPa spectra with Ar PTM, (ii) 20 GPa spectra with Fluorinert PTM. (iii) OrthoII HfO_2 Raman spectra. (iv) OrthoII ZrO_2 Raman spectra. (v) Mojaki's 26 GPa laser heated (L-H) Raman spectra [8]. Green dotted lines indicate the position of the signature orthoI peak at 400 cm^{-1}.

dotted lines in figure 4.24. Therefore, figure 4.24 compares Mojaki's Raman spectra involving laser-heating of the solid-solution at pressures bigger than 20 GPa with Raman spectra of orthoII phases of the end members, as well as our unambiguous identification of the Raman finger-print of the orthoI phase of the $Zr_{0.5}Hf_{0.5}O_2$ solid-solution. This inter-comparison, supported by our XRD results, suggests that Mojaki attained significant conversion to orthoII upon laser-heating at 26 GPa at temperatures not exceeding ~1500°C.

Figure 4.25 shows the comparison of the 20 GPa XRD data. The two Ar peaks are also clearly marked and are the (111) and (200) reflections in table 4.1. OrthoI is fully converted at 20 GPa and there is no indication of the orthoII phase. This is confirmed by the absence of (p) and (u) and the orthoII signature peak at about 20° (the (211) reflection). The Ar PTM laser heated data shows the orthoI peak (211) at about 14° (marked (o) in figures 4.22 and 4.25). To the right, are two shoulder features (p) and (u). These are the signature orthoII peak positions as seen in the end members labelled (102) and (111) reflections, respectively. Peak (s) at about 20° (211) is also a signature peak of the orthoII phase. The presence of the two shoulder features and the (211) reflection indicate the onset of the orthoII phase.

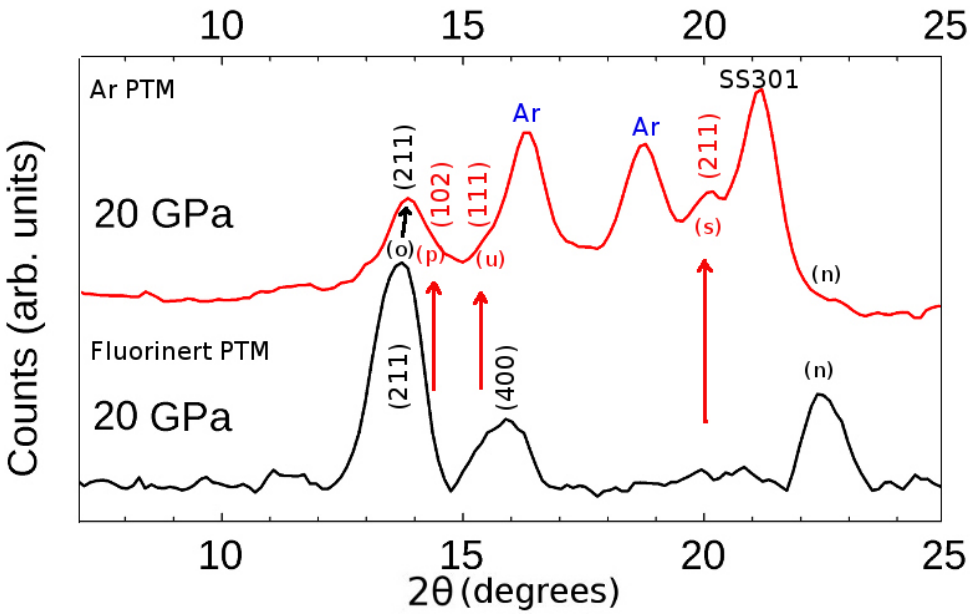

Figure 4.25: XRD comparison at 20 GPa of $Zr_{0.5}Hf_{0.5}O_2$ - 20 GPa Ar PTM laser heated $Zr_{0.5}Hf_{0.5}O_2$ and 20 GPa $Zr_{0.5}Hf_{0.5}O_2$ with Fluorinert PTM.

The high-pressure stabilized cotunnite phase can be recovered to ambient conditions (irreversibility) in the case of the end members ZrO_2 and HfO_2, whereas orthoI phase of $Zr_{0.5}Hf_{0.5}O_2$

cannot.

This study incorporated modest cost-effective tooling of the monocapillary compared with a synchrotron experiment. This work demonstrates that it is possible to give invaluable preliminary indicators of the pressure response of materials using the SMART diffractometer coupled with the 0.1 mm mono capillary (laboratory based XRD system) ahead of synchrotron experiments. It is anticipated that a quantitative analysis of this system can now be performed using a synchrotron experiment (proposal submitted to the beam line 27 at the ESRF). These laboratory-based XRD experiments have confirmed that the monoclinic to orthoI phase transition is sluggish at room temperature. The orthoI phase is fully stabilised at 20 GPa. Laser heating at 20 GPa initiates the conversion to orthoII. It is anticipated that protracted heating (hours) of the $Zr_{0.5}Hf_{0.5}O_2$ solid-solution will fully convert the orthoI phase to the orthoII phase. Alternatively, the pressure can be increased in the range 20-30 GPa with concurrent laser heating to accelerate the phase conversion to orthoII. This seems to have been the case in previous work of Mojaki (see figure 4.24).

5

Discussion and Conclusions

Low wave number lattice Raman modes at pressure may be tracked using the CZ-GAC. This is despite $Zr_{0.5}Hf_{0.5}O_2$ being found to be a weak scatterer in the region where the background from the CZ anvil tip is at its most intense. The data confirms the quality of the manual polished CZ anvils. This is the first time that Raman bands $Zr_{0.5}Hf_{0.5}O_2$ at pressure in the lattice mode region have been represented in MB-GAC experiments involving CZ. It is anticipated that the CZ-GAC may now be used quite routinely for Raman pressure measurements. It will suffice entirely for the case of strong to moderate scatterers or with Raman spectra very different to that of the spectra from the anvils. It may be possible to report valuable preliminary indicators of the pressure response of weak scatterers ahead of more suitable DAC experiments. The CZ-GAC is already known to be very suitable for IR spectroscopy work because of the low background in the high wave number regime, perhaps even superior to that of DAC work [18], taking into account that there may be a strong background contribution from Raman signals of the CZ anvil. This work demonstrates that complementary Raman data in the low wave number regime (lattice mode information) can also be derived from the same pressure cell, to appreciable pressures of 10-15 GPa. Pressures of 10-15 GPa easily covers and even exceeds the pressure range in which the pressure response of bio- and macro- molecular systems are investigated [20]. These ideas may find similar applicability in moissanite gem anvils [20], which have a higher strength and stability compared to CZ, so that pressures up to $\sim$20 GPa for relatively convenient culet sizes (of $\sim$400 μm) would be feasible. Emphasis must be placed on the modest cost-effective tooling and polishing techniques used for the CZ anvil preparation. This methodology could in the least case be used as an educational tool to school novices in analogous DAC preparation and pressurization techniques, without having to resort to expensive acquisition of diamond-anvils at

the outset. Furthermore, previous materials characterisation by optical spectroscopy at extreme high P-T conditions in excess of 10 GPa, (the almost exclusive domain of DACs) is now much more accessible with modest effort, expertise and cost.

The phase relations and compression behaviour of $Zr_{0.5}Hf_{0.5}O_2$ (nano-sized powders of unstabilized zirconia-hafnia solid-solution) under high pressure and high temperature have been investigated in-situ by observations using MB-DAC XRD and Raman spectroscopy. Two high pressure phases have been observed. OrthoI is present from about 5 GPa at room temperature and has been found to adopt the same structures as the end members ZrO_2 and HfO_2 (i.e. monoclinic to orthorhombic-I to cotunnite) at similar pressure ranges. The XRD data in conjunction with Raman spectra is a previously unreported result. The orthoI to orthoII (or cotunnite) phase is seemingly also sluggish as is the transition from monoclinic to orthoI seen in both MB-DAC high pressure experiments. This sluggishness may be overcome by heating at temperatures above 600°C [1]. The transition of the sample from monoclinic to orthoI is confirmed via Raman spectroscopy and XRD. The XRD data has been conclusively used to determine the set of Raman fingerprints for the orthoI phase of $Zr_{0.5}Hf_{0.5}O_2$ solid-solution. A further result shows that for the $Zr_{0.5}Hf_{0.5}O_2$ solid solution, the orthoI phase is not quenchable to ambient conditions as in ZrO_2.

The laser heating setup was modified to produce routine laser heating of samples. The addition of an extra CCD camera and the replacement of the main camera resulted in better alignment of the cavity and sample. $Zr_{0.5}Hf_{0.5}O_2$ begins the transformation from orthoI to the orthoII phase at 20 GPa and temperatures of between 500 and 1000°C. The transition from the orthoI phase to orthoII phase is evident by comparison to the end members. By comparing the Raman spectra and XRD data from the two separate 20 GPa pressure studies, it is clear that the laser heating is necessary at these pressures to assist the phase change to orthoII. It appears that the monoclinic to orthoI phase transition has to be complete (pressures of $\sim$20 GPa) before the orthoII transition can be initiated.

Our unambiguous identification of the Raman signatures of the orthoI phase, from complementary Raman and XRD pressure experiments, clarifies the previous higher P-T results of Mojaki [8]. The orthoI and orthoII Raman signatures of the $Zr_{0.5}Hf_{0.5}O_2$ solid-solution have now been firmly established experimentally.

XRD data has been analysed qualitatively ahead of envisioned future synchrotron experiments. This study incorporated modest cost-effective tooling of the monocapillary compared with a synchrotron experiment. This work demonstrates that it may be possible to obtain

valuable preliminary indicators of the pressure response of materials using laboratory XRD equipment (i.e. the SMART diffractometer and 0.1 mm monocapillary) ahead of more sophisticated synchrotron experiments so that beam-time can be used optimally. It is anticipated that a quantitative analysis of this system can now be performed efficiently by a synchrotron experiment. There have been a number of recent studies on quenched cotunnite phases of ZrO_2 and HfO_2 that have indicated very high bulk moduli of over 300 GPa [7, 56]. Our observations show that there are similar phase changes that are induced in the $Zr_{0.5}Hf_{0.5}O_2$ solid-solution, following similar pressure and temperature excursions in P-T phase space as for ZrO_2 and HfO_2 end-members. Therefore, it may be supposed that the high P-T phases of this solid-solution could well be new ultra-hard ultra-tough "superceramic" candidates.

Bibliography

[1] O. Ohtaka, H. Fukui, T. Kunisada, T. Fujisawa, K. Funakoshi, W. Utsumi, T. Irifune, K. Kuroda, and T. Kikegawa, "Phase relations and volume changes of hafnia under high pressure and high temperature," *Journal of the American Ceramic Society*, vol. 84, no. 6, pp. 1369–73, 2001. 1, 2, 3, 8, 10, 70, 73, 74, 77, 78, 87

[2] J. M. Leger and J. Haines, "The search for superhard materials," *Endeavor*, vol. 21, no. 3, pp. 121–124, 1997. 1, 2, 7, 14

[3] Y. Kamata, "High-k/Ge MOSFETs for future nanoelectronics," *Materials today*, vol. 11, no. 1-2, pp. 30–33, 2008. 1

[4] O. Ohtaka, H. Fukui, T. Kunisada, T. Fujisawa, K. Funakoshi, W. Utsumi, T. Irifune, K. Kuroda, and T. Kikegawa, "Phase relations and equations of state of ZrO_2 under high temperature and high pressure," *Physical Review B*, vol. 63, pp. 727–733, 2001. 1, 2, 3, 9, 10, 70, 73, 74, 77, 78

[5] O. Ohtaka, D. Andrault, P. Bouvier, E. Schultz, and M. Mezouar, "Phase relations and equation of state of ZrO_2 to 100 GPa," *Journal of Applied Crystallography*, vol. 38, p. 174108, 2005. 2, 10

[6] J. K. Dewhurst and J. E. Lowther, "Highly coordinated metal dioxides in the cotunnite structure," *Physical Review B*, vol. 64, p. 014104, 2001. 2, 10

[7] J. Haines, J. M. Leger, S. Hull, J. P. Petitet, J. P. Pereira, C. A. Perottoni, and J. A. H. da Jordana, "Characterization of the cotunnite-type phases of zirconia and hafnia by neutron diffraction and Raman spectroscopy," *Journal of the American Ceramic Society*, vol. 80, no. 1910, pp. 1910–1914, 1997. 2, 11, 88

[8] E. Mojaki, *Study of the zirconia-hafnia system and particularly its behaviour at high temperatures and pressures.* PhD thesis, University of the Witwatersrand, 2004. 3, 6, 7, 8, 9, 13, 28, 31, 39, 57, 58, 69, 75, 82, 83, 87

[9] A. F. Goncharov and J. C. Crowhurst, "Raman spectroscopy under extreme conditions," *Journal of Low Temperature Physics*, vol. 139, pp. 727–737, June 2005. 7, 31

[10] A. F. Holleman and N. Wilberg, *Inorganic Chemistry.* Walter de Gruyter, 2001. 8

[11] L. G. Liu, "New high pressure phases of ZrO_2 and HfO_2," *Journal of Physics and Chemistry of Solids*, vol. 41, no. 331, pp. 331–334, 1980. 10, 11

[12] W. Yang, R. G. Parr, and L. Uytterhoeven, "New relation between hardness and compressibility of minerals," *Physics and Chemistry of Minerals*, vol. 15, no. 2, pp. 191–195, 1987. 10

[13] "International crystalographic structure database version: 1.4.6," 2007. 11, 12

[14] L. Davison, Y. Horie, and T. Sekine, *High-Pressure Shock Compression of Solids V.* Springer, 2002. 11, 13

[15] A. Jayaraman, "Diamond anvil cell and high-pressure physical investigations," *Reviews of Modern Physics*, vol. 55, pp. 65–108, January 1983. 14, 26, 27, 31

[16] W. F. Wilkinson and G. Serman, *Advances in Infrared and Raman Spectroscopy*, vol. 6. Heyden and Son: London, 1980. 14

[17] D. E. Patterson and J. L. Margrave, "Use of gem-cut cubic zirconia in the diamond anvil cell," *Journal of Physical Chemistry*, vol. 94, pp. 1094–1096, 1990. 14, 15, 16, 17, 18, 20, 24

[18] T. P. Russell and G. J. Piermarini, "A high pressure optical cell utilizing single crystal cubic zirconia anvil windows," *Review of Scientific Instruments*, vol. 68, no. 4, pp. 1835–1840, 1997. 14, 16, 17, 19, 20, 22, 23, 86

[19] J. Xu, J. Yen, Y. Wang, and E. Huang, "Ultrahigh pressures in gem anvil cells," *Gem anvil pressure cells*, pp. 127–134, 1996. 15, 16, 59, 60

[20] N. R. Jackson, R. Erasmus, and G. Hearne, "Simplified manual fabrication of cubic-zirconia gem anvils for extended energy-range spectroscopic studies to routine high pressures of 100-150 kbar (10-15 GPa)," *Unpublished*, 2009. 16, 58, 65, 67, 86

[21] J. Xu and E. Huang, "Graphite-diamond transition in gem anvil cells," *Review of Scientific Instruments*, vol. 65, no. 1, pp. 204–207, 1994. 17, 24

[22] S. A. Moggach, D. R. Allan, S. Parsons, and J. E. Warren, "Incorporation of a new design of backing seat and anvil in a Merrill-Bassett diamond anvil cell," *Journal of Applied Crystallography*, vol. 41, pp. 249–251, 2008. 18, 19, 20, 37

[23] E. Sterer and M. P. Pasternak, "A multipurpose miniature diamond anvil cell," *Review of Scientific Instruments*, vol. 61, no. 3, pp. 1117–1119, 1990. 19, 41, 46

[24] R. Miletich, D. R. Allan, and W. F. Kuhs, "High-pressure single-crystal techniques," *Reviews in Mineralogy & Geochemistry*, vol. 41, pp. 445–519, 2000. 19, 21, 22, 24, 36, 46, 82

[25] I. F. Silvera, A. D. Chijioke, W. J. Nellis, A. Soldatov, and J. Tempere, "Calibration of the ruby pressure scale to 150 GPa," *Phisica Status Solidi*, vol. b, no. 1, pp. 460–467, 2007. 20, 21, 22

[26] J. Witlinger, R. Fischer, S. Werner, J. Schneider, and H. Schultz, "High-pressure study of *h.c.p.*-argon," *Acta Crystallographica Section B*, vol. B53, pp. 745–749, 1997. 23, 48, 78

[27] G. Hearne, A. Bibik, and J. Zhao, "CO_2 laser-heated diamond-anvil cell methodology revisited," *Journal of Physics: Condensed Matter*, vol. 14, pp. 11531–5, 2002. 23, 24, 25, 26

[28] R. Boehler, "New diamond cell for single-crystal x-ray diffraction," *Review of Scientific Instruments*, vol. 77, p. 115103, 2006. 24

[29] Y. Akahama, H. Kawamura, and A. K. Singh, "Equation of state of bismuth to 222 GPa and comparison of gold and platinum pressure scales to 145 GPa," *Journal of Applied Physics*, vol. 92, no. 10, pp. 5892–7, 2002. 24

[30] S. Ndiaye, "Introduction to the fundamentals of Raman scattering." Presented as a short lecture course in the School of Physics , WITS University Johannesburg, SA Nov-Dec 2004. 27

[31] P. Dhamelincourt, J. Barbillat, and M. Delhaye, "Laser confocal Raman microspectrometry," *Spectrometry Europe*, pp. 16–27, 1993. 27, 30, 31

[32] J. C. de Paula, "Raman spectroscopy of metalloporphyrins," *Access: http://www.haverford.edu/chem/302/Raman.pdf*, 10 December 2010. 27

[33] D. A. Long, *Raman Spectroscopy*. McGraw-Hill, Inc., 1977. 27

[34] I. Gregora, "Raman scattering," *International Tables for Crystallography*, vol. D, pp. 315–328, 2006. 27, 32

[35] I. E. Wachs, "Raman and IR studies of surface metal oxide species on oxide supports: Supported metal oxide catalysts," *Catalysis Today*, vol. 27, pp. 437–455, 1996. 29

[36] G. B. B. M. Sutherland, *Infra-red and Raman Spectra*. Methuen & Co. LTD., 1935. 30

[37] M. Baraton and M. El-Shall, "Synthesis and characterization of nanoscale metal oxides and carbides: Ii. micro-Raman and FT-IR surface studies of a silicon carbide powder.," *NanoStractured Materials*, vol. 6, 1995. 32

[38] B. E. Warren, *X-ray diffraction*. Dover publications, INC. New York, 1990. 33

[39] M. M. Woolfson, *An introduction to x-ray crystallography*. Cambridge University Press, 1997. 33

[40] H. P. Klug and L. E. Alexander, *X-ray Diffraction Procedures For Polycrystalline And Amorphous Materials*. Wiley New York, 1974. 35

[41] S. Cornaby, T. Szebenyi, R. Huang, and D. H. Bilderback, "Design of single-bounce monocapillary x-ray optics," *JCPDS-International Centre for Diffraction Data*, pp. 194–200, 2007. 34, 36, 82

[42] "Mono-capillary optics," *Access: http://www.horiba.com/us/en/scientific/products/x-ray-fluorescence-analysis/tutorial/mono-capillary-optics/*, 10 December 2010. 36

[43] K. Brister, "X-ray diffraction and absorption at extreme pressures," *Review of Scientific Instruments*, vol. 68, no. 4, pp. 1629–1647, 1997. 37

[44] "Boehler almax anvils," *access: http://www.almax-industries.com/Boehler-Almax.html*, 10 December 2009. 38, 44

[45] A. Hammersly, S. Stevenson, M. Hanfland, A. Fitch, and D. Hausermann, "FIT2D," *Access: http://www.esrf.eu/computing/scientific/FIT2D/*, 2 June 2008. 38, 54

[46] "Apollo scientific cc," *Access: http://www.apollosci.co.za/*, 8 November 2009. 41

[47] Leica-Microsystems-Ltd, *Leica L2.* Business Unit SM CH-9435 Heerbrugg (Switzerland), english m1-288-0en ed., 2001. 53

[48] G. R. Hearne, J. Zhao, A. M. Dawe, V. Pischedda, M. Maaza, M. K. Niewoudt, P. Kibasomba, O. Nemraoui, J. D. Comins, and M. J. Witcomb, "Effect of grain size on structural transitions in anatase TiO_2: A Raman spectroscopy study at high pressure," *Physical Review B*, vol. 70, p. 134102, 2004. 53, 65

[49] Brucker-AXS-Inc., *computer program SMART-NT.* Bruker AXS Inc., Madison, Wisconsin, USA., 1998. 54

[50] C. Carlone, "Raman spectrum of zirconia-hafnia mixed crystals," *Physical Review B*, vol. 45, no. 5, pp. 2079–2084, 1991. 58, 82

[51] T. Ohsaka, F. Izumi, and Y. Fujiki, "Raman spectrum of anatase, TiO_2," *Journal of Raman Spectroscopy*, vol. 7, no. 6, p. 321, 1978. 60, 65

[52] K. Lagarec and S. Desgreniers, "Raman study of single crystal anatase TiO_2, up to 70 GPa," *Solid state communications*, vol. 94, no. 7, pp. 519–524, 1995. 65

[53] S. Takele and G. R. Hearne, "Electrical transport, magnetism, and spin-state configurations of high-pressure phases of FeS," *Physical Review B*, vol. 60, pp. 4401–4403, 1999. 67

[54] S. Block, G. J. Piermarini, B. J. Hockey, B. R. Lawn, and R. G. Munro, "High-pressure transformation toughening: A case study on zirconia," *Journal of the American Ceramic Society*, vol. 69, no. 6, pp. 125–126, 1986. 74

[55] S. Merkel, "Simulation of high pressure diffraction pattern," *Access: http://merkel.zoneo.net/HPDiff/applet.html*, 12 December 2007. 78

[56] S. Desgreniers and K. Lagarec, "High-density ZrO_2 and HfO_2: Crystalline structures and equations of state," *Physical Review B*, vol. 59, no. 13, pp. 8467–8472, 1999. 82, 88

[1]

[1]Numbers after the date refer to the page numbers where the references appear in the text.